VIBRATIONAL SPECTROSCOPY AND MICROSCOPIC IMAGING OF SKIN

I. COLLAGEN HYDRATION IN TYPE I COLLAGEN AND DERMAL TISSUE

II. LATERAL DIFFUSION OF EXOGENOUS AGENTS IN HUMAN SC

III. CERAMIDE PERMEATION INTO HUMAN SKIN

by

QIHONG ZHANG

A Dissertation submitted to the

Graduate School-Newark

Rutgers, The State University of New Jersey

in partial fulfillment of the requirements

for the degree of

Doctor of Philosophy

Graduate Program in Chemistry

written under the direction of

Professor Richard Mendelsohn

and approved by

_____

_____

_____

_____

Newark, New Jersey

October, 2014

ABSTRACT OF THE DISSERTATION

VIBRATIONAL SPECTROSCOPY AND MICROSCOPIC IMAGING OF SKIN

I.   COLLAGEN HYDRATION IN TYPE I COLLAGEN AND DERMAL TISSUE

II.   LATERAL DIFFUSION OF EXOGENOUS AGENTS IN HUMAN SC

III.   CERAMIDE PERMEATION INTO HUMAN SKIN

By QIHONG ZHANG

Thesis director: Professor Richard Mendelsohn

Confocal Raman spectroscopy and dynamic vapor sorption (DVS) measurements of human Type I collagen and pigskin dermis were performed to probe relative humidity (RH) dependent differences in the nature and level of collagen hydration. Raman spectra were also acquired as a function of time for both Type I collagen and pigskin dermis samples upon exchange of a 100% RH H_2O to deuterium oxide (D_2O) environment. Alterations in Amide I and III modes were consistent with anticipated changes in hydrogen bonding strength as RH increased and upon $H \rightarrow D$ exchange. Of note is the identification of a Raman spectral marker (band at 938 cm^{-1}) which appears to be sensitive to alterations in collagen-bound water. Analysis of DVS isotherms provided a quantitative measure of adsorbed and absorbed water vapor consistent with the Raman results.

Infrared (IR) spectroscopic imaging was utilized to evaluate lateral diffusion in stratum corneum (SC) and elucidate intermolecular interactions between exogenous agents and SC constituents. In separate experiments, acyl chain perdeuterated oleic acid (OA-d) and deuterated dimethyl sulfoxide (DMSO-d)

were applied to the surface of isolated human SC. The lateral distribution of permeant concentrations was monitored using the time-dependence of IR images. Diffusion coefficients (D) were estimated from Fick's second law. Networked glyphs served as the major pathway for lateral distribution of OA-d. In glyph-poor regions, D values 0.3-1 x 10^{-8} cm^2/s bracketed the OA-d data and apparently decreased with time and diffusion of DMSO-d suggests D values of ~10^{-7} cm^2/s. Interactions between the exogenous agents and the SC were tracked from changes in CD_2 and Amide I stretching frequencies. OA-d spectral changes suggest penetration into the ordered lipids of the SC; DMSO-d penetration results in perturbation of SC keratin structure.

IR imaging was also used to investigate permeation properties of two types of ceramides in human skin. IR images were acquired after incubating for 24 or 48 H with deuterated ceramide suspended in oleic acid. IR images of ceramide concentration were obtained after applying Beer's Law. Analysis of IR spectra and concentration images suggest the detection limit of both ceramide around 3.5 mM, and most of the ceramide reside in concentrated localized pockets on skin surface, and in deep glyphs. Further analysis indicates the permeation of both ceramide into top layers of SC.

Acknowledgements

I wish to express my sincere appreciation to my supervisor and mentor, Prof. Richard Mendelsohn, for his patience, encouragement, invaluable help and guidance throughout my Ph.D. study. He has been supportive and has given me the freedom to work in my own way. This dissertation would not have been possible without his continuous support.

Many thanks to Dr. Carol Flach for her help, patience and beneficial suggestions throughout my dissertation work.

I would like to thank my thesis committee: Prof. Huskey, Prof. Lalancette and Dr. Russel M. Walters, for their suggestions, insightful comments and corrections to my thesis.

I am also thankful to our collaborators Laurence Senak, David J. Moore, Mary Catherine Mack Correa, Russel M. Walters for their generous and professional support. Thanks to Prof. Joan I. Morrell, for her help with microtoming that is important to my research.

I also thank former group members and friends in the Chemistry Department for their advice and encouragement.

I would also like to thank my parents and other members of my family. They were always supporting me and encouraging me with their best wishes and continuous love.

Last but not least, I would like to dedicate this thesis to my husband, Jiawei Chen, and our daughter, Scarlett Chen, for their endless support, patience and understanding. Without them I could not have made it here.

Table of Contents

List of Figures

List of Tables

List of Abbreviations

Acyl chain perdeuterated oleic acid	OA-d
Asymmetric CD2 stretching mode	ν_{asym}CD2
Center of mass	COM
Ceramides	CER
Cholesterol	CHOL
Concentration/initial concentration	C/Co
Deuterium oxide	D2O
Diffusion coefficient	D
Dimethylsulphoxide	DMSO
Dimethyl-d6 sulfoxide	DMSO-d
Dynamic vapor sorption	DVS
Factor analysis	FA
Free fatty acids	FFAs
4-hydroxyproline	Hyp
Lamellar bodies	LBs
Long periodicity phase	LPP
Microemulsions	MEs
Migrating epithelial tongue	MET
Natural moisturizing factor	NMF
Oleic acid	OA
N-palmitoyl (d31)-D-erythro-sphingosine	CER [NS]-d31
N-palmitoyl (d9)-D-phytosphingosine	CER [NP]-d9

N-palmitoyl (d31)-D-phytosphingosine	CER [NP]-d31
Principal components	PCs
Principal component analysis	PCA
Propylene Glycol	PG
Relative humidity	RH
Short periodicity phase	SPP
Sodium dodecyl sulfate	SDS
Sodium lauryl sulphate	SLS
Stratum basale	SB
Stratum corneum	SC
Stratum granulosum	SG
Stratum spinosum	SS
Symmetric CD2 stretching mode	$\nu_{sym}CD2$
Transepidermal water loss	TEWL

Chapter 1 Introduction

1.1 Skin structure

1.1.1 Basic skin structure

Skin, the largest organ of the human body, accounts for approximately 16% of total body weight. One of the most important roles of skin is to form an effective barrier between the "inside" and the "outside" of the organism, which prevents loss of water and other components of the body to the environment and protects the body against exogenous substances from the environment (Figure 1-1)[1-3].
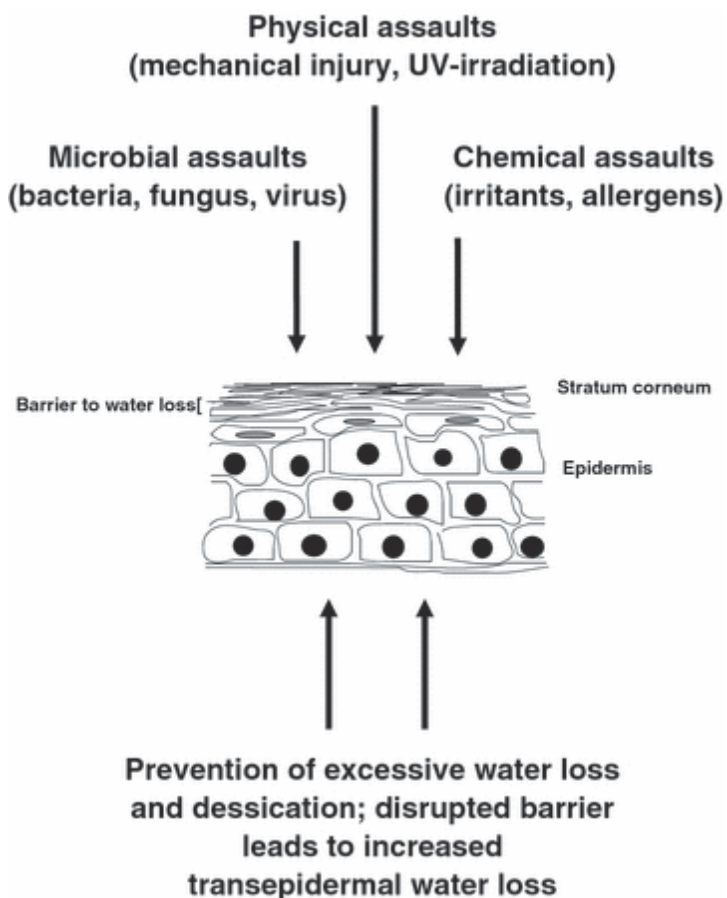
Fig. 1-1 Functions of the epidermal "inside-outside" and "outside-inside" barrier. This image was initially published in the Exp. Dermatol[1].

The skin (Figure 1-2) is divided into three main structural layers: epidermis, dermis and hypodermis (subcutaneous tissue). In the epidermis (Figure 1-3)[1] layers of keratinocytes appear in the following order (bottom to top): stratum basale (SB)-the undifferentiated layer, where cell proliferation occurs, stratum spinosum (SS)-where differentiation begins, stratum granulosum (SG)-where further differentiation continues, and stratum corneum (SC)-acellular layers.
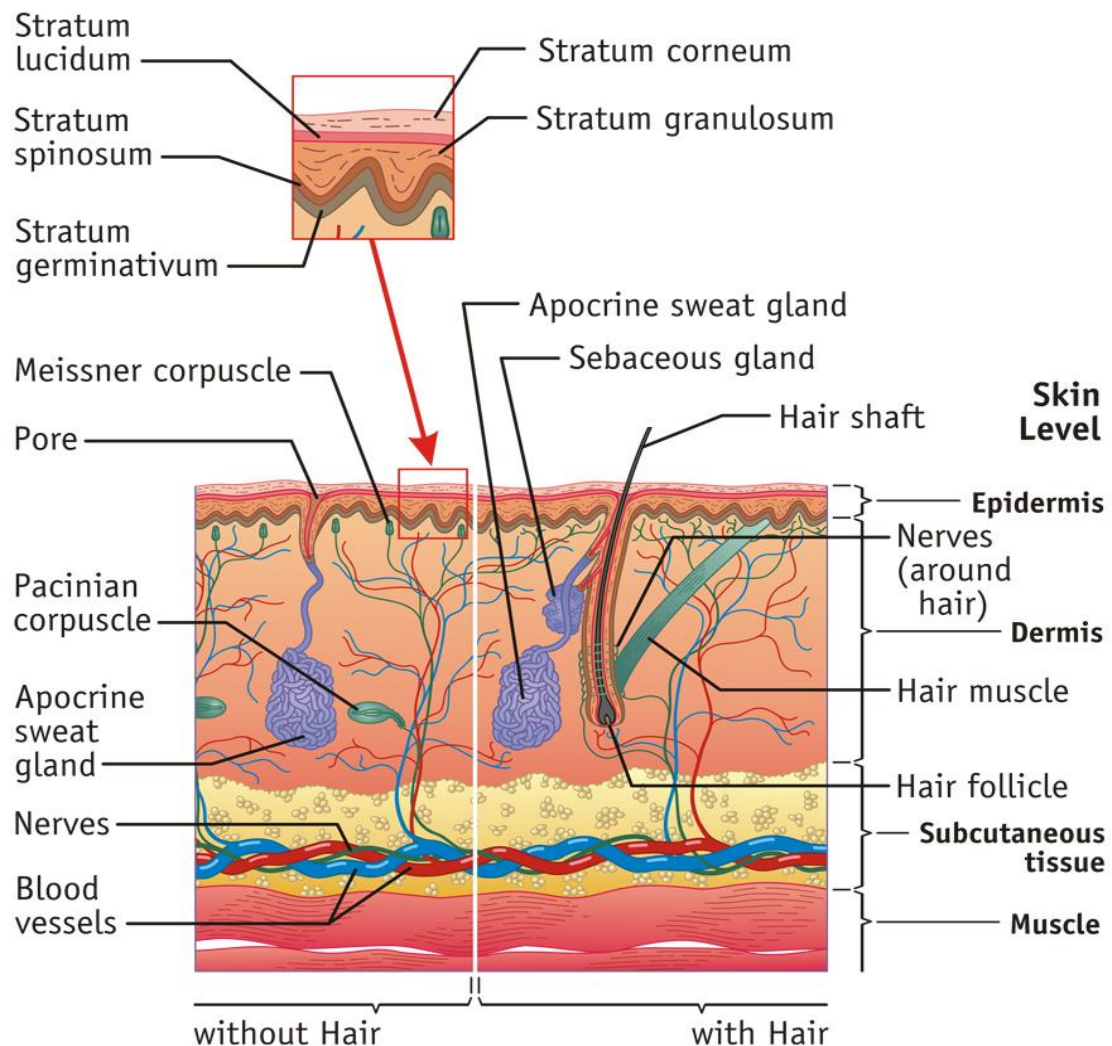
Fig. 1-2. A diagram of skin cross-section with anatomical features and sub-layers. This image was generated by Hilmers Studio[4].

The predominant cell type of the epidermis is the keratinocyte. They appear in the basal layer, and transiently migrate to the granular layer where they

transform into the corneocytes of the SC. These have undergone terminal differentiation with degradation of the nucleus, loss of DNA[5], flattening and finally have adopted the dimensions characteristic of the dead cells of the SC[6]. In the SG, two types of granules are formed: keratohyalin granules, which contain protein, and lamellar bodies (LBs), which are full of lipids. During the process, the nucleus is digested, the cytoplasm disappears, the keratin intermediate filaments aggregate to form microfibrils, the lipids are released into the intercellular space, and the cell membrane is replaced by a cell envelope made of cross-linked protein with lipids covalently attached to its surface. The resulting corneocytes that forms the SC tend to be in the shape of either a hexagon or pentagon approximately 25 μm on a side with a surface area of approximately 1000 μm^2 and a thickness of approximately 0.5 to 1.0 μm. Keratinocytes make keratin and many other proteins. They form a unique cornified envelope that serves as a platform for a neutral lipid enriched extracellular matrix.

1.1.2 Stratum corneum

The SC, the outermost layer of the epidermis, serves as the primary barrier against water loss and environmental insults. It contains about 12~16 cell layers that are oriented anucleated corneocytes as hydrophilic "bricks" embedded in a continuous highly ordered extracellular matrix as hydrophobic "mortar".
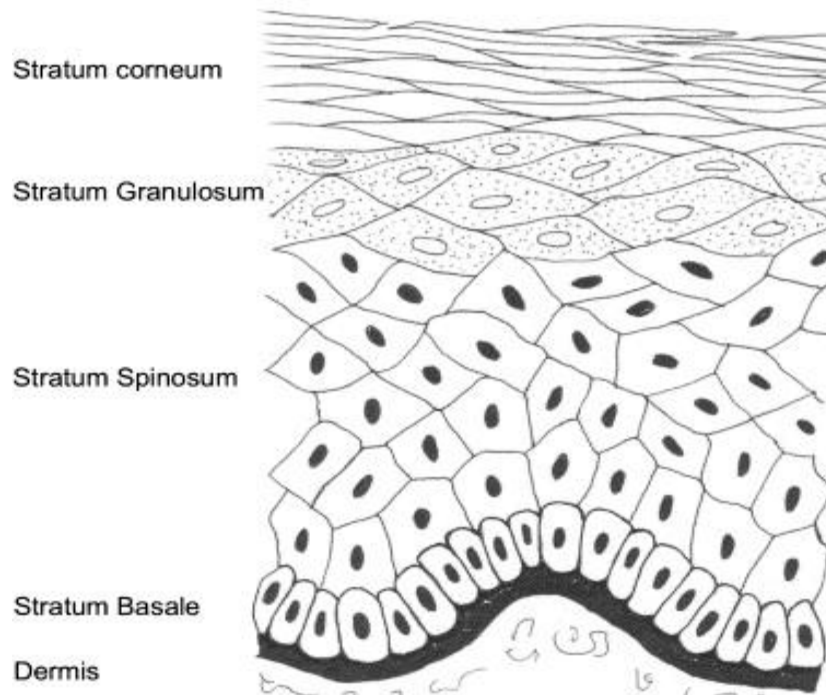
Fig. 1-3. Diagram of the four main layers of the epidermis. This image was initially published in Am. J. Infect. Control[7].
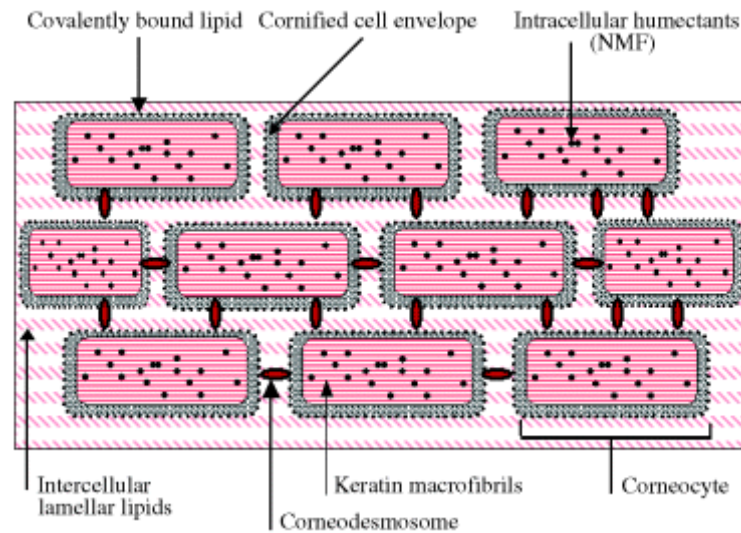
Fig. 1-4. Schematic "Bricks and Mortar" model of the SC representing the structural and functional components. This image was initially published in Dermatol. Ther.[8].

The corneocytes are keratin-rich dead cells. During the final stages of normal differentiation, keratins are aligned into highly ordered and condensed arrays upon interaction with filaggrin, a matrix protein synthesized as profilaggrin in the keratohyalin granules of the granular layer. Filaggrin aggregates the keratin filaments into tight bundles. Together, keratin and filaggrin constitute 80-90% of the protein mass of mammalian epidermis[1, 2]. There are mainly two types of keratin formed in keratinocytes, an acidic type I keratin and a neutral to basic type II keratin. Acidic keratins have more negatively charged amino acid side chains, and basic keratins have more positively charged side chains. This allows the formation of a structure called the *coiled-coil* form after interaction between two α helical proteins[9-11]. Coiled-coils are important to the structure of the keratinocytes and help maintain its integrity. Improper assembly of coiled-coil can lead to fragile keratinocytes.

In the intercellular space of the corneocytes lies the lipid lamellar matrix. Precursor lipids are secreted from LBs, containing stacks of lipid disks, enriched in polar lipids, glycosphingolipids, free sterols, phospholipids and catabolic enzymes, *etc.*, derived from the Golgi apparatus in the SS and SG. Upon reaching the SC, these LBs fuse with cell membranes and release lipids that are subsequently modified and arranged into intercellular lamellar bilayers positioned parallel to the cell surface. The secretion of LBs are regulated by the level of calcium in the SG. The polar lipids are enzymatically converted into non-polar products. The major lipid classes in the SC are ceramides, free fatty acid and cholesterol in an approximately equimolar ratio[1, 12].

The intercellular lipid matrix in human SC shows a unique lamellar arrangement, in which the lipids are organized in lamellar sheets regularly stacked on top of each other. Furthermore, the lipids appear to be organized in a so-called broad-narrow-broad arrangement. Two lamellar phases have been identified with periodicities of 6.4 nm (short periodicity phase = SPP) and 13.4 nm (long periodicity phase = LPP) of which the 13.4 nm phase is suggested to be important for the skin barrier function[3]. Lipid organization within the lamellae is referred to as "lateral organization" as depicted in Figure 1-5[3, 6].
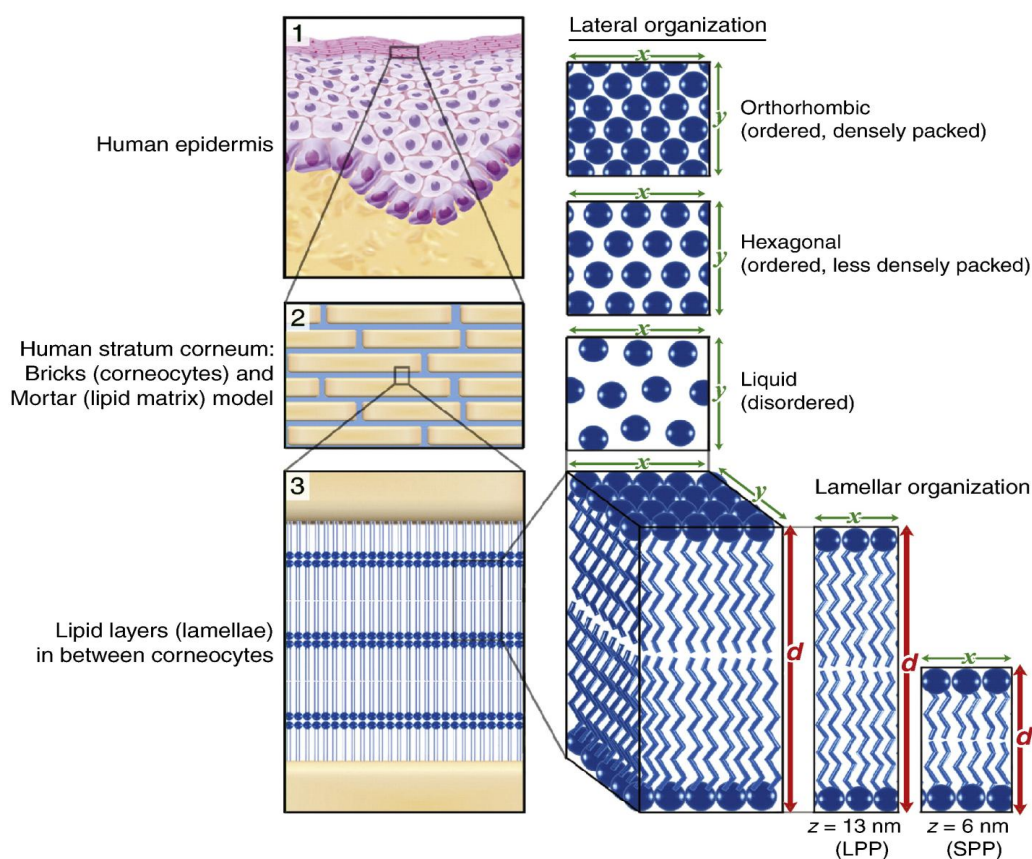
Fig. 1-5. Lipid packing in human SC. (1) the outmost layer of the epidermis, the SC. (2) "Bricks and Mortar" model. (3) With either a long or short repeat distance (d). The lateral organization refers to the plane perpendicular to the direction of the lamellar organization. This image was originally published in the Journal of Lipid Research[13].

In healthy human skin, the SC lipids are mainly packed in a very dense orthorhombic phase, along with a subpopulation packed in a less dense hexagonal phase or even in the low density, disordered, liquid phase. The dermis layer is ~ 1-2 mm thick, and is composed of connective tissue that includes collagen (contributing ~80% of the tissue's total dry weight) and elastic fibers in a gel of glycosaminogycans[14, 15]. Dermal collagen provides tissue integrity and tensile strength to skin.

1.2 Confocal Raman microscopy

1.2.1 Instrumentation   Raman spectra of skin were acquired with a Kaiser Optical System Raman Microprobe shown in Figure 1-6. The instrumentation has been described in detail elsewhere[16, 17]. Generally, an external-cavity-stabilized solid-state diode laser emitting at 785 nm, with ~6-8 mW of single mode laser power at the sample (nominal spot size ~2 μm), was utilized for excitation. The wavelength was selected to minimize fluorescence background from skin samples. The laser light is transmitted to the confocal microscope system via a single-mode excitation optical fiber. The back-scattered Raman light from the

sample is collimated by the same (100X) objective lens and passed through the microscope system, and delivered to the detector by a collection optical fiber.
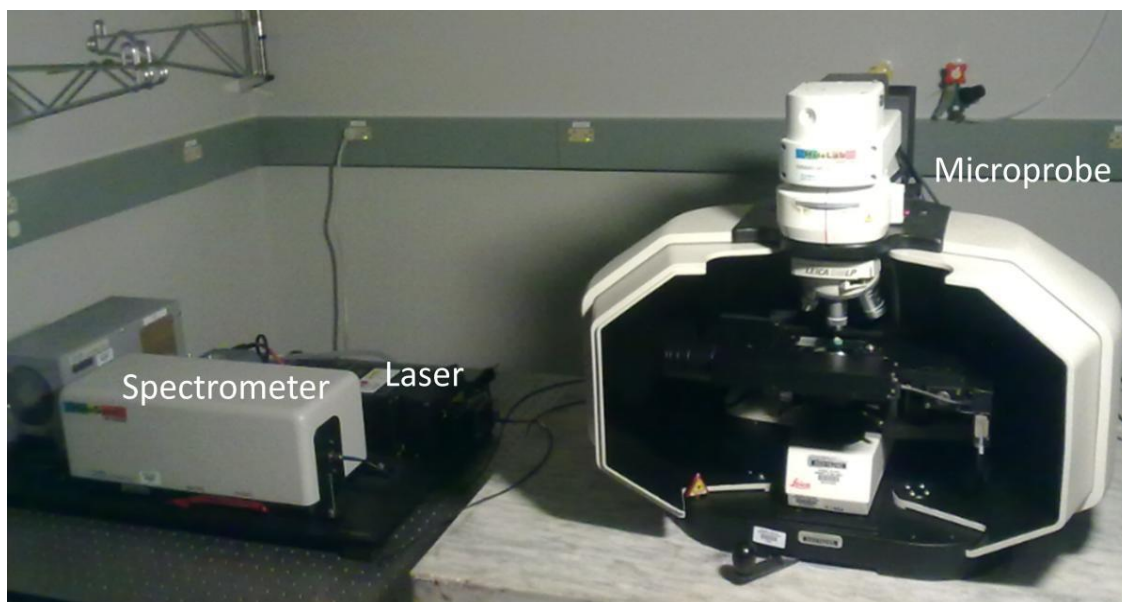
Fig. 1-6. Kaiser Optical Systems Raman microprobe.

The laser light sent to the detector passes a pair of notch filters which are used to attenuate several orders of magnitude of the input laser signal from Rayleigh scattering. The Kaiser HoloPlex transmission grating disperses and divides the collected Raman light into a low wavenumber shift stripe and a high wavenumber shift stripe on the charge-coupled device (CCD) used for detection and then stacks the two stripes on top of each other. As a result, the HoloPlex grating essentially doubled the spectral coverage without significant diffraction efficiency loss (the two stripes have some spectral overlap, which reduces the spectral coverage below double). The spectral range is 100 cm^{-1} to 3450 cm^{-1} while data are encoded at ~ 0.3 cm^{-1} intervals. The near-IR CCD (ANDOR Technology, Model DU 401-BR-DD) is a linear array detector possessing 128

pixels on the spatial axis and 1024 pixels on the spectral axis. The optical microscope is a Leica DLMO microscope with reflected/transmitted light illumination, operating in the epi-illumination mode. A computer-controlled stage which can be moved with high precision in the X, Y and Z directions is integrated in a base unit enclosure which is used to block interference from environmental light. Spectra can be taken in defined three dimensions by precise control of the stage together with an incorporated video camera for evaluation of the sample site.

In our experiments on full-thickness skin samples, 1-2 μm lateral and 2-3 μm confocal resolution was achieved. Laser light traveling through layers of skin components with different refractive indices was attenuated due to the heterogeneity of the skin. In the intact skin Raman mapping experiments, a Leica oil immersion objective (100X) was used to minimize the Raman scattering losses and to achieve better resolution.

1.2.2 Applications of confocal Raman microscopy

Confocal Raman microscopy, as a noninvasive optical method, can provide detailed information about molecular composition, structure, and interaction. It has been applied to measure molecular concentration profiles in the skin *in vivo* by Caspers*, et. al*. They were able to quantitatively determine the water concentration in the SC and semi-quantitatively measure major constituents for natural moisturizing factor (NMF) and sweat as a function of depth from the skin surface with a resolution of 5μm[18].

Xiao, *et al.* reported the utilization of the confocal Raman microscopy on laminated polymer and pigskin. They evaluated the thickness distortions in confocal measurements for laminated polymer, which are quite significant, and compared the univariate analyses and multivariate analyses of both samples, which shows consistency and also provides distinct diagnostic markers for both the SC and the viable epidermis of skin[16].

Zhang, *et al.* applied confocal Raman microscopy on pigskin biopsies treated with a prodrug of 5-fluorouracil, which is known to enhance transdermal delivery of an important systemic antitumor drug. They were able to image the outermost layers of intact skin in a non-invasive manner and to differentiate closely related chemical species in the skin without the necessity for external labels. Confocal Raman microscopy was shown to provide a convenient, non-perturbing technique to monitor the spatial distribution of exogenous materials and their biochemical transformation in intact skin[19].

1.3 IR microsopy

1.3.1 Instrumentation

The Perkin Elmer Spotlight system 300 (shown in Figure 1-7) used in these studies consists of an FT-IR spectrometer coupled to an IR microscope. A home-built case was also installed to provide constant relative humidity and temperature with constant purge of dry house air. The microscope includes a high-performance cassegrain mirror system with a wide collection angle (high numerical aperture) and high efficiency collection system for infrared radiation for

microspectroscopy applications. There are two cassegrains in the imager. The lower cassegrain condenses the beam from the spectrometer to an appropriate size for a microscopic sample and focuses it at the sample position. The upper cassegrain collects light from the sample and sends it upward through the aperture and the upper dichroic mirror. When collecting an IR image in transmittance, the beam is reflected on the upper dichroic mirror to the detector cassegrain and then focuses the radiation onto a linear array (16 X 1 detector elements) of mercury-cadmium-telluride (MCT) detector. The sample sits on a motorized stage, controlled by a joystick and the Spotlight software, which enables one to find points on the sample with high precision in the X, Y and Z directions. The imager includes a camera and viewing system that magnifies the visible-light image of the sample to facilitate positioning and isolation of point of interest.

Fig. 1-7. Perkin Elmer Spotlight Imaging system 300

When imaging the sample in transmittance, it is important to prepare the sample properly to collect good quality spectra. The sample should ideally be thin enough (approximately 5 to 20 μm) to give good detail and undistorted absorption bands.

1.3.2 Applications of IR microscopy

Although IR microscopic imaging does not permit confocal data collection, the approach offers advantages such as permitting the sampling of larger areas (up to a few millimeters) at higher signal-to noise ratios (for the same scan time) than Raman, although at worse spatial resolution (~10-12 μm in the IR versus ~1-2 μm in the Raman). Another useful advantage is that Beer's Law is obeyed in the IR, thereby permitting determination of concentration of exogenous molecules in skin; whereas, Raman microscopy can only provide relative concentration information.

IR microspectroscopic imaging has been used to map the spatial distribution of two penetration enhancers, propylene glycol (PG) and dimethylsulphoxide (DMSO) in porcine skin to a permeation depth of >1 mm in microtomed sections by Mendelsohn, *et al.* With the utilization of deuterated isotopomers, the approach can monitor the penetration of exogenous agents while simultaneously permitting evaluation of endogenous lipid behavior and protein secondary structures in skin[20].

Yu, *et al.* reported the investigation of lipid conformation in the migrating epithelial tongue (MET) in an *ex vivo* human organ culture skin wound healing

model by IR imaging for the first time. IR spectra of different regions of the skin have characteristic spectral features. Through factor analyses of different spectral regions, they were able to delineate different skin regions, and even small conformational change of the lipids within and in the vicinity of the MET. They also used univariate measure to support their factor analysis results, which proves the reliability of IR microspectroscopic imaging as a powerful imaging tool[21].

A good example of using IR imaging to quantitatively investigate the distribution of sodium dodecyl sulfate (SDS) in skin was reported by Mao, *et al.* [22] Upon deuteration of SDS, both confocal Raman microscopy and IR imaging were able to map SDS-d penetration into the porcine skin, mostly within the SC under various treatment conditions. In addition, IR imaging can provide concentration profiles of the SDS-d in both porcine and human skins. The availability of a complete vibrational spectrum at each sampling pixel of a confocal Raman and IR image provides unique molecular level information regarding the changes in physical properties of SDS and evaluation of its tendency to damage the skin barrier.

1.3.3 Principal component analysis and factor analysis

An IR image of a skin sample contains thousands of spectra. To evaluate the useful information in these spectra that cannot be manifest by univariate analysis, two multivariate statistical methods, principal component analysis (PCA) and factor analysis[22], were applied.

PCA is one of the most frequently used tools in the analysis of spectral images. It describes the important information in an image in terms of relatively small number of channels, the so-called Principal Components (PCs). It can be used either as a data reduction method, or as a classification method. The PCs are ranked in terms of the percentage of the total spectral variance that they explain. A loading vector is generated for each PC, giving the spectral dependence of that component. The projections of a data set in its original form onto loading vectors calculated for each component yield a set of scores, which provide a representation of those spectra in terms of the PCs.

The principal component decomposition of an image is equivalent to finding a decomposition of the data matrix: $X = \sum_j S_j L_j$

where X is the two-dimensional matrix formed by laying each pixel spectrum below the previous one, shown successive columns of the image. Each S_j is a px1 score vector.   The dimension p corresponds to the original spatial dimensions m and n of the image cube (p=mxn). Each L_j is a 1xk loading vector, where k is the spectral dimension of the data matrix.   The product $S_j L_j$ is the fractional variance of X accounted for by the j'th principal component.

The resulting loading vectors are not generally pure component spectra. FA is a method to detect structure in the relationships between variables in order to classify them, or to reduce the number of variables (dimensionality) of the data set. If the spectral image is proportional to an absorbance image, then to the

extent that Beer's Law is obeyed, the intensity at the ij'th pixel and the k'th wavelength can be expanded as:

$$I_{ijk} \sim \sum_m C_m e_{mk}$$

where c_m is the concentration of species m and the e_{mk} is the molar extinction coefficient of species m at the k'th wavelength of the spectrum. If we 'unfold' the image cube into a two dimensional array, **X**, with pixel spectra along each row, we can then express that matrix as a sum of outer products of concentration vectors and pure component spectra:

$$X = \sum_m C_m e_m$$

where each c_m is a px1 vector (p = number of pixels in the image), each component of which represents the concentration of species m at a particular pixel. e_m is a 1xk (k = number of channels in each pixel spectrum) spectrum of species m. An analogous factorization will hold if X represents Raman data[23].

FA seeks transformation from the abstract PAC loading vectors which corresponds to the directions of maximum uncorrelated variance, to the underlying factors. The starting point is the generation of a set of scores and loadings corresponding to the currently specified source data set. The scores will be generated by the matrix multiplication **S=X*L'**, where **L'** is the transpose of the matrix of normalized loadings.

Factor analysis of the IR image data was carried out using the score segregation routine available in ISys. The analysis seeks to detect simple patterns in the relationships between observed variables in order to reduce the dimensionality of the data set. Score segregation begins by normalization of PCA scores by channel to the range 0-1, which may be 'sharpened' by raising them to

a power specified by an acceleration parameter. Factor loadings are calculated according to: $(S'S)^{-1} * S' * X$. Typically 2-6 significant factors are observed.

ISys 5.0 was used in the current IR images of skin for FA. Generally, there are four steps for the operation: determination of the appropriate spectral region of interest, determination of the number of factors, diagonalization of the original covariance matrix, and score segregation. Determination of the number of factors is an interactive process because of the characteristically stratified structure of skin samples: statistically meaningful factors may or may not be biologically informative. Generally, two or more than the expected number of factors can be set before diagonalization of the original covariance matrix. After score segregation, the set number of factors can be obtained or not. If yes, it is necessary to check whether each factor loading correlates to the original data set. Otherwise, it is optional to either increase the number of factors for more possible new findings, or decrease the number to eliminate similar factors (difference is not distinguishable enough), or if the iterative process for the factor loading calculation does not converge, or if the signal-noise level is too low for any factor loading spectrum.

An example of utilizing factor analysis in the CH stretching spectral region (2830-3000 cm^{-1}) to delineate different skin layers in IR images is shown in Figure 1-8. Factor analysis was applied for skin samples under different preparation conditions, and three factors were captured for SC, VE, and dermis, respectively, in Figure 1-8A. Three factor loadings shown in Figure 1-8B clearly differentiate the spectral characteristics of the three layers and are nearly

identical to the original spectra from each skin region (not shown). Factor score

loading images are shown for each loading spectrum in column 2-4 of Figure 1-

8A. The color coding measures the correlation between the original spectrum at

each pixel and the factor loading spectrum, with red showing the highest

similarity and blue, the lowest[24].
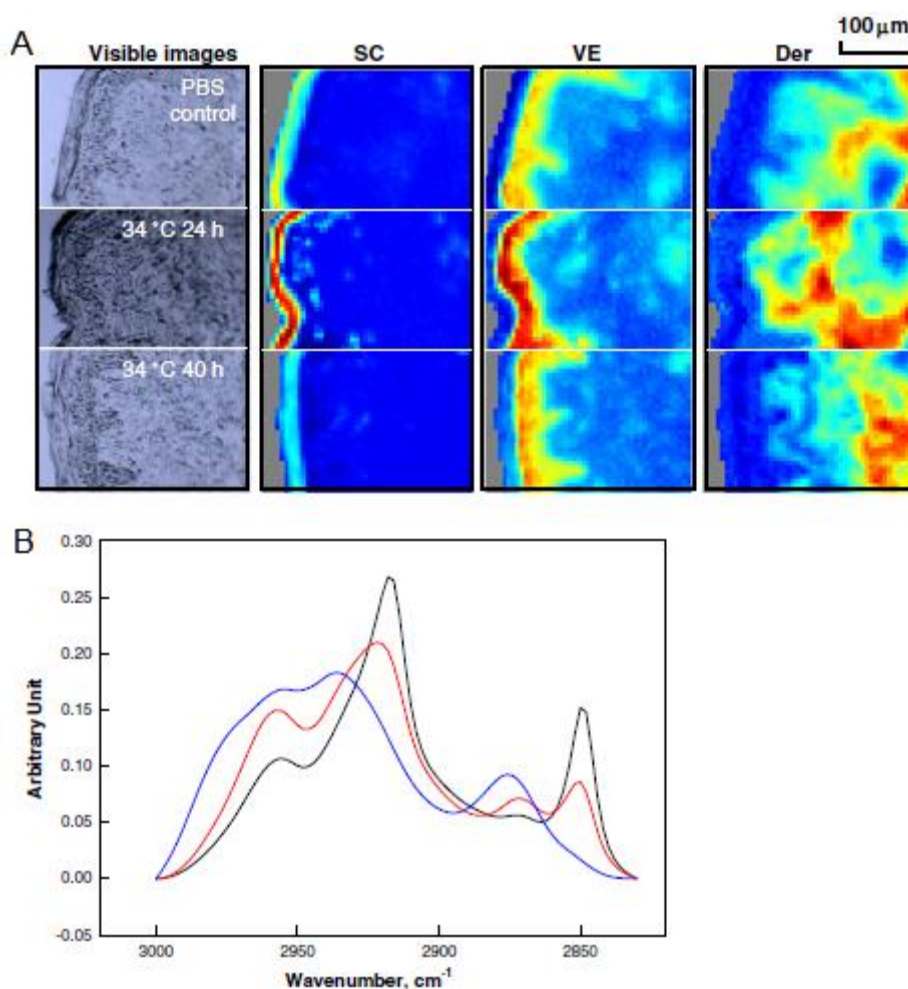
Fig. 1-8. The utilization of factor analysis in IR images of skin sections. 8A. Visible images and factor loading score images of the skin (scores color coding: red>yellow>blue) depicting different regions of human skin under different treatment conditions. 8B. Factor loadings of each skin region: SC (black), VE (red) and Der (blue). This image was initially published in Pharm. Res.[24].

In this thesis, collagen hydration properties were investigated by Confocal

Raman microscopy, and lateral diffusion of exogenous agents on SC and

permeation of two types of ceramides into the SC were studied by IR spectroscopy. The results will be discussed in Chapters 2-4, respectively.

1.4 References:

1. Proksch, E.; Brandner, J. M.; Jensen, J. M., The skin: an indispensable barrier. *Experimental Dermatology* **2008,** 17, 1063-1072.
2. Baroni, A.; Buommino, E.; De Gregorio, V.; Ruocco, E.; Ruocco, V.; Wolf, R., Structure and function of the epidermis related to barrier properties. *Clinics in Dermatology* **2012,** 30, 257-262.
3. Bouwstra, J.; Gooris, G.; Ponec, M., The lipid organisation of the skin barrier: Liquid and crystalline domains coexist in lamellar phases. *Journal of Biological Physics* **2002,** 28, 211-223.
4. Helmers, W., Integumentary System, American Pharmacists Association, Pharmacists College Student Book. *http://www.hilmersstudios.com/sample/medical/integumentary-system*.
5. Feingold, K. R.; Elias, P. M., Role of lipids in the formation and maintenance of the cutaneous permeability barrier. *Biochim Biophys Acta* **2013**.
6. Van Smeden, J.; Janssens, M.; Gooris, G. S.; Bouwstra, J. A., The important role of stratum corneum lipids for the cutaneous barrier function. *Biochim Biophys Acta* **2013**.
7. Wickett, R. R.; Visscher, M. O., Structure and function of the epidermal barrier. *American Journal of Infection Control* **2006,** 34, S98-S110.
8. Harding, C. R., The stratum corneum: structure and function in health and disease. *Dermatol Ther* **2004,** 17 Suppl 1, 6-15.
9. Steinert, P. M., Structure, Function, and Dynamics of Keratin Intermediate Filaments. *Journal of Investigative Dermatology* **1993,** 100, 729-734.
10. Fuchs, E., Keratins and the skin. *Annual Review of Cell and Developmental Biology* **1995,** 11, 123-153.
11. Steinert, P. M., Organization of Coiled-Coil Molecules in Native Mouse Keratin 1/Keratin-10 Intermediate Filaments - Evidence for Alternating Rows of Antiparallel in-Register and Antiparallel Staggered Molecules. *Journal of Structural Biology* **1991,** 107, 157-174.
12. Hwa, C.; Bauer, E. A.; Cohen, D. E., Skin biology. *Dermatologic Therapy* **2011,** 24, 464-470.
13. Janssens, M.; van Smeden, J.; Gooris, G. S.; Bras, W.; Portale, G.; Caspers, P. J.; Vreeken, R. J.; Hankemeier, T.; Kezic, S.; Wolterbeek, R.;

Lavrijsen, A. P.; Bouwstra, J. A., Increase in short-chain ceramides correlates with an altered lipid organization and decreased barrier function in atopic eczema patients. *Journal of Lipid Research* **2012,** 53, 2755-2766.

14. Odland, G. F., In physiology, biochemistry, and molecular biology of the skin *Oxford University Press: New York* **1991**, 1-62.

15. Tobin, D. J., Biochemistry of human skin - our brain on the outside. *Chemical Society Reviews* **2006,** 35, 52-67.

16. Xiao, C. H.; Flach, C. R.; Marcott, C.; Mendelsohn, R., Uncertainties in depth determination and comparison of multivariate with univariate analysis in confocal Raman studies of a laminated polymer and skin. *Applied Spectroscopy* **2004,** 58, 382-389.

17. Zhang, G. J.; Moore, D. J.; Mendelsohn, R.; Flach, C. R., Vibrational microspectroscopy and imaging of molecular composition and structure during human corneocyte maturation. *Journal of Investigative Dermatology* **2006,** 126, 1088-1094.

18. Caspers, P. J.; Lucassen, G. W.; Carter, E. A.; Bruining, H. A.; Puppels, G. J., In vivo confocal Raman microspectroscopy of the skin: Noninvasive determination of molecular concentration profiles. *Journal of Investigative Dermatology* **2001,** 116, 434-442.

19. Zhang, G.; Moore, D. J.; Sloan, K. B.; Flach, C. R.; Mendelsohn, R., Imaging the prodrug-to-drug transformation of a 5-fluorouracil derivative in skin by confocal Raman microscopy. *J Invest Dermatol* **2007,** 127, 1205-9.

20. Mendelsohn, R.; Chen, H. C.; Rerek, M. E.; Moore, D. J., Infrared microspectroscopic imaging maps the spatial distribution of exogenous molecules in skin. *Journal of Biomedical Optics* **2003,** 8, 185-190.

21. Yu, G.; Flach, C.; Tomic-Canic, M.; Stojadinovic, O.; Mendelsohn, R., Vibrational Spectroscopy, Microscopy and Imaging Probes Cutaneous Wound Healing and Artificial Skin Structure. *Biophysical Journal* **2013,** 104, 339a-340a.

22. Tfayli, A.; Piot, O.; Manfait, M., Confocal Raman microspectroscopy on excised human skin: uncertainties in depth profiling and mathematical correction applied to dermatological drug permeation. *Journal of Biophotonics* **2008,** 1, 140-153.

23. Hardle, W.; Simar, L., Applied multivariate statistical analysis (Third Edition). *Springer* **2003**, (ISBN 978-3-642-17228-1).

24. Mao, G.; Flach, C. R.; Mendelsohn, R.; Walters, R. M., Imaging the Distribution of Sodium Dodecyl Sulfate in Skin by Confocal Raman and Infrared Microspectroscopy. *Pharmaceutical Research* **2012,** 29, 2189-2201.

Chapter 2: Raman Microspectroscopic and Dynamic Vapor Sorption Characterization of Hydration in Collagen and Dermal Tissue

2.1 Introduction

The structure and organization of collagen, the major mammalian structural protein, has been actively studied for over half a century. Initial fiber diffraction studies[2] revealed three polyproline II-like chains wrapped around a common axis. Close packing near the central axis requires that glycine occupies the third residue position in each chain yielding the characteristic collagen X-Y-Gly repeating pattern. Only one direct interchain hydrogen bond is formed between amide groups (Gly-NH $\cdots$ O=C-X) for each set of three residues[2]. The most common triplet motif is Pro-Hyp-Gly, where the presence of Hyp (4-hydroxyproline) results from the enzymatic post-translational modification of Pro residues. Key features stabilizing the structure are the high proportion of Hyp residues and water. Although steric restriction precludes direct H-bonding between the Hyp–OH groups and peptide C=O groups, X-ray crystallographic studies of model collagen peptides reveal repetitive intrachain, interchain, and intermolecular water bridges involving Hyp-OH and backbone carbonyls[1, 3]. In addition to this ordered arrangement of water bridging, an extended cylinder of hydration involving networks of hydrogen-bonded water molecules suggests that hydration plays a major role in collagen fiber assembly[1-4]. Overall, water is clearly an intrinsic feature of collagen structure.

Understanding collagen structure and hydration in intact tissue is of primary importance to the medical and cosmetic communities. In skin, the most abundant component in the dermis is collagen, comprising ~80% of the tissue's total dry weight and ~90% of all dermal protein[5, 6]. Type I collagen is dominant (85-90%) in healthy dermal tissue and Type III is present at ~10%. Dermal collagen provides tissue integrity and tensile strength to skin among other functions. Although age, UV exposure, and disease-related changes in the mechanical, physical, and biochemical properties of collagen have been documented[7-9], the molecular basis for the alterations are not yet fully understood. It is likely that these modifications partially involve changes in collagen hydration. Raman spectroscopy[10, 11] and MRI[12, 13] have been used to study changes in collagen hydration levels due to aging and UV exposure, yielding somewhat conflicting results. Briefly, the content of free (non-collagen bound) water was reported in human dermis using in vivo and ex vivo methods. An increase in water content was reported for photoaged compared to non-exposed dermis[10, 12], whereas water content for non-exposed elderly versus young dermis ranged from no change[10] to significantly higher[11] in the elderly samples. The basis for these differences is uncertain. However, a general consensus exists that the bulk water content in the dermis increases with age, while the collagen-bound water content decreases. The ability to differentiate collagen-bound from bulk water is of interest in studies ranging from the evaluation of therapeutics for wound healing to the hydration efficacy of skin care products.

Towards this end, the current work utilizes confocal Raman microscopy to probe the response of Type I collagen and intact dermal tissue to a range of relative humidity (RH) values and to H_2O to deuterium oxide (D_2O) exchange with the aim of defining spectral parameters for the collagen-bound water content. It is well known that Raman spectra are sensitive to protein secondary and higher order structures, including hydrogen bonding, mostly through the analysis of frequency positions and widths of the Amide I and III bands. In addition, spectral features from particular vibrational modes including amino acid side chains provide information about local conformation, environment, and hydrogen bonding. Raman spectroscopy is a nondestructive method which permits both macroscopic and microscopic observations and can be applied *in vivo* to skin or *ex vivo* to skin biopsies. Applications of confocal Raman microscopy to study skin processes have been demonstrated recently, including the permeation and metabolism of drugs in intact tissue[14-16], the characterization of pathological states[17, 18], and *in vivo* measurements of bulk water content[11, 19]. The technique is limited when applied to skin *in vivo* to a total depth of 100-150μm, sampling papillary dermis only.

As an adjunct to the confocal Raman experiments, dynamic vapor sorption (DVS) measurements were conducted on intact dermis to provide a wider-ranging measure of dermal hydration. Modeling of sorption isotherms highlights differences in classes of water interacting with the dermal tissue, i.e., monolayer, multilayer, and internally absorbed[20]. The DVS results for internally absorbed water are compared with the Raman measurements of collagen-bound water and

previously reported quantitative measures of collagen hydration using a variety of physical techniques.

2.2 Materials and methods

2.2.1 Materials:

Type I collagen from human skin (purity 95%) was purchased from Calbiochem. Skin biopsies (approximately 2 mm thick) from white, hairless Yucatan miniature pigs were purchased from Sinclair Research (Auxvasse, MO). The fresh tissue was frozen in liquid nitrogen and stored at -20°C. The epidermis was removed from the frozen biopsies using a razor blade prior to further sample treatment. Deuterium oxide (D_2O), 99.9%, was purchased from Cambridge Isotope Laboratories, Inc.

2.2.2 Methods:

Hydration of Type I collagen and pigskin dermis at various RHs for Raman measurements

About 0.5 mg of Type I human skin collagen was tightly packed in a circular well (~6 mm in diameter) milled into a home-built brass humidity cell and sealed under a glass coverslip. The sample sits upon a piece of mesh which is positioned over a small circular reservoir (~2 mm in diameter and 10 mm in depth). The cell was designed for *in situ* confocal Raman microscopic examination of tissue samples under conditions of controlled humidity. A side

port connected to the small reservoir allows solutions to be exchanged in the cell so the sample is exposed to the vapor phase without direct contact to the solution. The samples were dried to approximately 0% RH by placing the cell in a desiccator under house vacuum at 22°C for 48 H. Following the acquisition of Raman spectra, various saturated salt solutions were used to generate a series of increasing RH values at 22°C to which the same Type I collagen sample was exposed. The salts used in the current studies and their respective RH values are: LiCl, RH 15%; $CaCl_2 \bullet 2H_2O$, RH 32%; $Ca(NO_3)_2 \bullet 4H_2O$, RH 55%; NH_4Cl + KNO_3, RH 73%; $BaCl_2$, RH 88%. Collagen samples were allowed to equilibrate in controlled environments for at least 20 H prior to acquisition of Raman spectra at each RH. Maximal hydration was achieved by exposing the sample to pure distilled water (100% RH) at 22°C for 20 H.

A section of frozen pigskin dermis (~5 mm^2, 2 mm thick) was allowed to defrost at room temperature before being placed in the humidity cell. The same salts and conditions described above were used to achieve the following RH environments: 0%, 32%, 55%, 73%, and 100%.

Hydrogen-Deuterium exchange experiments

In separate experiments, either Type I human skin collagen or pigskin dermis was placed in the humidity cell as described above and exposed to 100% RH (distilled water) for 20 or 40 hrs, respectively. Following acquisition of Raman spectra at 100% RH, water was replaced with D_2O in the humidity cell reservoir and spectra were acquired approximately every 10 min over a 48 H period.

Raman measurements and data processing

Confocal Raman spectra were acquired from Type I collagen and pigskin dermis samples beginning at a position ~10μm under the surface using a Kaiser Optical Systems Raman Microprobe equipped with a 785 nm solid state diode laser. A 100x oil immersion objective was used to focus approximately 6-10 mW of single mode power within a sample volume of ~2μm^3. The backscattered light was dispersed on an ANDOR Technology, Model DU 401-BR-DD, near-IR CCD detector. Spectral coverage ranges from 100 to 3450 cm^{-1} at a spectral resolution of 4 cm^{-1}. Spectra were acquired using a 60 second exposure time, 4 accumulations, and automatic cosmic ray correction. Data analysis was carried out with ISys software, version 3.1 (Malvern Instruments Ltd) and Grams/32 AI software version 6.0 (Thermo Scientific).

Dynamic Vapor Sorption measurements

Dynamic Vapor Sorption (DVS) is a gravimetric technique that may used to monitor the interaction of a probe molecule (e.g. water) with the substrate of interest (e.g. skin). During testing, the water vapor content is changed stepwise with time and changes in mass are monitored by a sensitive microbalance. The sorption and desorption steps are carefully controlled such that at each isohume the sample reaches or closely approaches an equilibrium mass. Although the experiments are time consuming, proper equilibration between the substrate and vapor facilitates fitting of the data to isotherm models to discern the allocation of *adsorbed* and *absorbed* vapor in probe-substrate interactions.

The water vapor sorption-desorption experiments were performed with a DVS Advantage-1 gravimetric vapor sorption analyzer (Surface Measurement Systems Ltd., London, UK). The pre-dried dermis had dimensions of approximately 5 mm x 5 mm x 2 mm thick and a weight of 40-50 mg. The experimental temperature was 25.0 ±0.1 °C and the total gas flow was 200 sccm (standard cubic cm per minute). The drying, sorption, and desorption sequence consisted of the following steps:

1. Drying step: The thawed dermis sample was loaded into the DVS on a 13mm quartz pan and dried for 24 H at 25°C and 0% RH.

2. Sorption-Desorption curves: Three separate sorption-desorption experiments were performed to study the moisture regain of the dermis as a function of time:

    a. The initial sorption experiment consisted of an isothermal humidity ramp from 0-90% RH in 10% RH steps. Desorption from 90-0% RH followed the sorption process. Each sorption-desorption step was 6 H in duration.

    b. The second sorption experiment was comprised of an isothermal humidity ramp from 0-90% RH in 15% RH steps. Desorption from 90-0% RH followed the sorption process. Each sorption-desorption step was 24 H in duration to approximate gravimetric equilibration.

    c. The third experiment consisted of an initial isothermal humidity ramp from 0-30% RH in 5% RH steps, followed by a humidity ramp from 30-90% RH in 15% steps. Desorption from 90-30% RH in

15% steps followed by a 30% RH to 0% RH in 5% RH steps followed the sorption process. Each sorption-desorption step in the 0-30% RH range was 48 H in duration to better approximate equilibration; whereas, the 30-90% RH range steps were all 24 H in duration.

The resultant sorption isotherms were subsequently analyzed using the Young and Nelson model[20]. The theory of Young and Nelson, which is derived from kinetic molecular theory of gases, may be used to describe the allocation of water vapor adsorbed or absorbed by the substrate as monolayer adsorbed, multilayer adsorbed, or bulk absorbed by fitting the data from sorption-desorption processes to equations 1 through 7[20, 21],

(1) $\quad \theta = \frac{p}{p_0} / \left(\frac{p}{p_0} + \left(1 - \frac{p}{p_0}\right) \cdot E \right)$

(2) $\quad E = \exp\left[-\frac{(q_1 - q_L)}{kT}\right]$

(3) $\quad \varphi = \frac{p}{p_0} \theta$

(4) $\quad \alpha = -\frac{E \cdot \frac{p}{p_0}}{E - (E-1) \cdot \frac{p}{p_0}} + \frac{E^2}{E-1} \ln \left[\frac{\left(E - (E-1) \cdot \frac{p}{p_0}\right)}{E} \right] - (E+1) \cdot \ln \left(1 - \frac{p}{p_0}\right)$

where θ is the fraction of the skin surface covered by a layer of bound water, E is a parameter related to the heat of adsorption of water molecules bound to the surface, φ is the fraction of the monolayer of water covered by at least one layer of condensed water molecules, q_1 is the heat of adsorption of water to the surface, q_L is the normal heat of condensation, and p and p_0 are the vapor pressure of water and the saturation pressure of water at the prescribed

isotherm, respectively and α is the amount of normally condensed water, which is measured in adsorption layers.

$$(5) \quad M_{sorp} = A(\theta + \alpha) + B\varphi$$

$$(6) \quad M_{desorp} = A(\theta + \alpha) + B\theta \left(\frac{p}{p_0}\right)_{max}$$

$$(7) \quad A = \rho v_{\frac{m}{W}}, B = \frac{\rho V}{W}$$

Equations 5, 6, and 7 relate the equilibrium content of adsorbed (M_{sorp}) and desorbed (M_{desorp}) water to the E, A, and B parameters. A and B describe the distribution of surface adsorbed and bulk absorbed water vapor, respectively; $\left(\frac{p}{p_0}\right)_{max}$ is the maximum empirical humidity; and v_m, V, and W are the volume of monolayer water, volume of absorbed moisture at saturation, and the mass of dried skin, respectively.

Because q_1, v_m, and V are all simultaneously unknown, the analysis software (Isotherm Analysis Suite, v2.1, Young and Nelson module) uses a combination of iteration and multiple regression techniques to choose the value of E and associated A and B to best correlate Young and Nelson theory to the experimental raw isotherm plot of equilibrium moisture sorbed at each partial pressure value. A correlation coefficient (r^2) value of 0.995 was obtained for the data shown in the inset in Figure 2-8.

2.3 Results and discussion

2.3.1 Raman measurements of collagen hydration

Raman spectra of human skin type I collagen equilibrated at increasing relative humidity values are shown in Figure 2-1. Humidity-dependent changes are evident in a few spectral regions and are highlighted in the difference spectrum shown at the bottom of Figure 2-1. As expected, spectral changes consistent with alterations in hydrogen bonding are observed in both the Amide I (1600-1700 cm^{-1}, predominantly C=O stretching) and Amide III (1200-1300 cm^{-1}, mostly N-H in-plane bending and C-N stretching) modes. In particular, as RH increases, the more intense component in the Amide I band displays a small downshift in frequency from ~1672 to 1665 cm^{-1} along with an increase in the position of the low frequency component of Amide III at ~1245 cm^{-1}. These observations are consistent with an increase in hydrogen bonding strength as RH increases. It is well established that when hydrogen bonding involves one of the atoms in a stretching vibration, a frequency decrease is observed whereas the opposite occurs for a bending mode. An unanticipated and more easily quantifiable humidity-dependent alteration is observed in the characteristic collagen doublet-of-doublets pattern between 820 and 980 cm^{-1}. The vibrational origin of the bands was discussed many years ago by Frushour and Koenig[22]. They assign the 938 cm^{-1} feature to ν(C-C) of the protein backbone, while the bands at 922 and 856 cm^{-1} arise from ν(C-C) of the proline ring and the 876 cm^{-1} feature arises from ν(C-C) of the Hyp ring. Assignment of the 938 cm^{-1} band to

ν(C-C) of the protein backbone is somewhat tentative as other reports assign the band to the ν(C-C) of the proline ring[23, 24]. In the current set of experiments, we observe a marked intensity increase in the 938 cm^{-1} band with increasing RH along with other smaller variations.
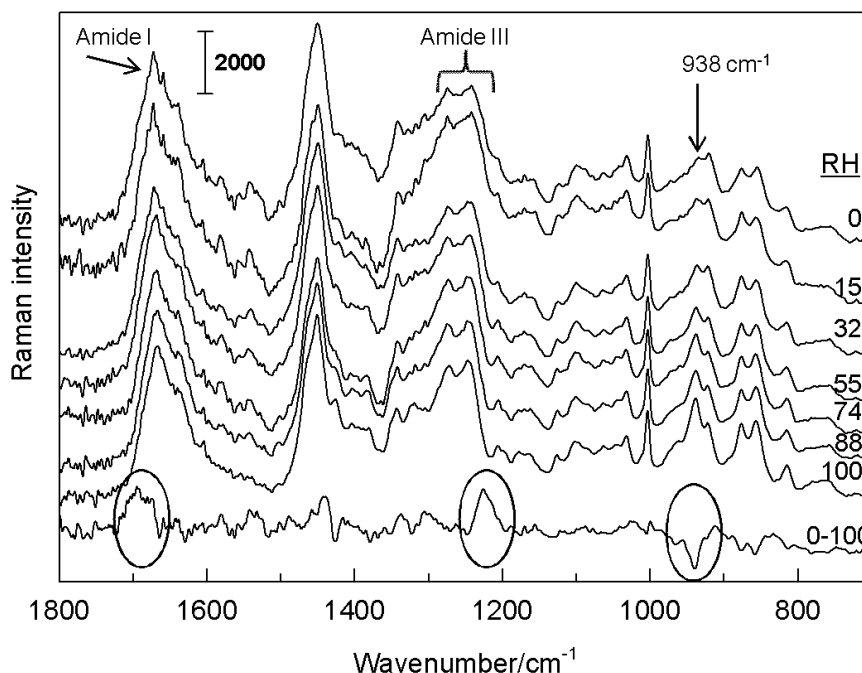
Fig. 2-1. Raman spectra of Type I collagen from human skin (1800-600 cm^{-1} region) after exposure for ~20 H to various relative humidity (RH) values, increasing from top to bottom, as noted. Averaged spectra are shown (3-5 spectra) after subtraction of glass (coverslip), baseline correction, and normalization to the phe ring stretching mode at ~1003 cm^{-1}. A difference spectrum (100% RH - 0% RH) is shown on the bottom with particular spectral features highlighted (see text for details).

Similar RH experiments were conducted with pigskin dermis and Raman spectra of particular spectral regions are highlighted in Figure 2-2. The bottom spectrum in both parts of the Figure was acquired from a section of pigskin that was not subjected to the relatively extreme low humidity experimental conditions. The sample was simply quick frozen as described in Materials and Methods and thawed at room temperature, followed by exposure to a 100% RH environment.

Comparing the bottom spectrum in Figure 2-2A and 2B to that directly above (exposed to 0 through 100% RH conditions), respectively, it is apparent that the low RH-induced alterations are essentially fully reversible in both spectral regions consistent with DSC studies on rat tail tendon[25]. In addition, a similar downward shift in Amide I (Figure 2-2A) and upward shift in Amide III (not shown) with increasing RH was observed when comparing pigskin dermis to human Type I collagen. Furthermore, the humidity-induced intensity increase in the C-C backbone stretch at 938 cm^{-1} is evident in Figure 2-2B. In a recent porcine corneal laser ablation study[24], temperature sensitivity of the 938 cm^{-1} band intensity was demonstrated. Although the results from the corneal studies do not strictly compare to the results presented herein (response of 938 cm^{-1} band intensity to temperature vs. RH, respectively), they are broadly consistent with each other, i.e. exposure to higher temperatures results in a decrease in intensity. On the other hand, their interpretation of the 938 cm^{-1} band intensity response differs. Further discussion is deferred to the section on H-D exchange. In the current work, the integrated area ratio of the entire 988-898 cm^{-1} region to the low frequency half of the 922 cm^{-1} band was used to quantitate the intensity increase in the C-C backbone stretch (938 cm^{-1} band) with RH. This spectrally-based hydration parameter is plotted as a function of RH in Figure 2-3 for both Type I skin collagen and pigskin dermis.

As is evident in Figure 2-3, the range of the measured hydration parameter is quite similar (~4-7) for Type I skin collagen and pigskin dermis. This observation provides a level of confidence in the general utility of this parameter

as a hydration probe. Although collagen comprises ~80% of the fat free dry weight of skin[5], the additional constituents found in the dermis such as, elastin, fibrillin, etc. do not appear to interfere with the intensity measurement of the
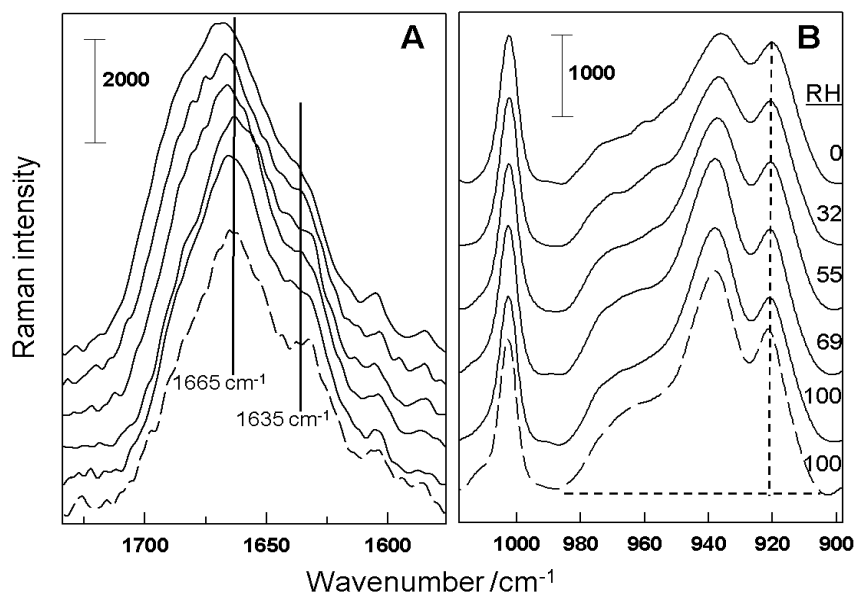
Fig. 2-2. Averaged Raman spectra of intact pigskin dermis at various RH values as noted, increasing from top to bottom. The bottom spectrum (dashed) is acquired from pigskin dermis that was not previously dried. 2A. The 1730-1575 cm^{-1} region with predominant components of the Amide I band marked to highlight the downshift in the 1665 cm^{-1} component as RH is increased. 2B. The 1018-898 cm^{-1} region delineating the band areas used to calculate the hydration parameter shown in Figure 3 (see text for details). Spectra are baseline corrected and normalized to the phe mode at ~1003 cm^{-1}.

Raman bands used in the hydration parameter calculation. In addition, the presence of other collagen types in the dermis, particularly Type III (~10%), may respond similarly to RH. Interestingly, it appears as if each material has a different response to increasing RH. Whereas the response of Type I collagen is nearly linear from 0-80% RH with an increase in slope at RH>80%, pigskin dermis has a sigmoidal response (see Figure 2-3). Higher order structural differences between collagen fibers in dermis compared to the Type I sample may be responsible for the relative resistance of the dermis to dehydration at low

RH and saturation at RH≥70%. A similar observation, i.e. saturation for RH≥75%, was observed in the infrared spectra of bovine tendon collagen[26]. The current observation may lead one to question whether or not the samples were fully equilibrated after the incubation period at each RH value. The inset to Figure 2-3 compares the hydration parameter at several RH values for Type I collagen equilibrated for 2 compared to 20 H. At ~0% RH, the 2 H sample does not appear to be as dry as the Type I collagen equilibrated for 20 H and at RH>40%, the 2 H sample appears to be less hydrated than that equilibrated for 20 H. The sample appears to be closer to equilibrium when incubated for 20 H.
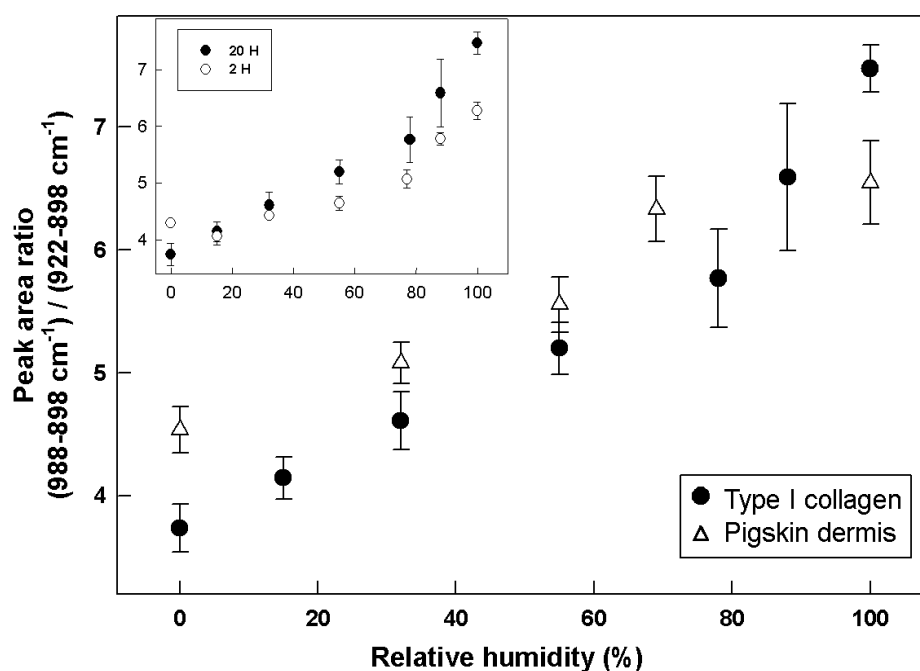
Fig. 2-3. Integrated peak area ratio (988-898 cm^{-1}/ 922-898 cm^{-1}) as a function of RH obtained from confocal Raman spectra of Type I collagen (filled circle) and pigskin dermis (open triangle) shown as mean values +/- standard deviation after ~20 H exposure to various RH's. Inset: The same peak area ratio for Type I collagen after exposure to various RH's for 2 H (open circle) and ~20 H (filled circle).

Confocal Raman images of the hydration parameter obtained for pigskin dermis at several RH levels are displayed in Figure 2-4 and provide clear

evidence for the near equilibration of dermal hydration following an initial 20 H incubation period. The same section of dermis is used for the set of images and the RH conditions are maintained while spectra are acquired. Following the initial equilibration period at each of the five RH levels, the acquisition of spectra is initiated from top to bottom (10 spectra, one every 5 microns) and left to right (9 z-lines of spectra, one every 5 microns) within the dermal section, requiring an additional ~12 H. If equilibration of dermal hydration was not complete after the initial 20 H, the hydration parameter at each RH would show an increasing value moving across each line of spectra from left to right as each z-line requires ~1.3 H for acquisition. This is not observed. The variation within each image, however, likely reflects differences in the spatial distribution of collagen hydration in the dermis. Overall, images of the Raman-based hydration parameter (Figure 2-4) are observed to respond to RH increases as anticipated.
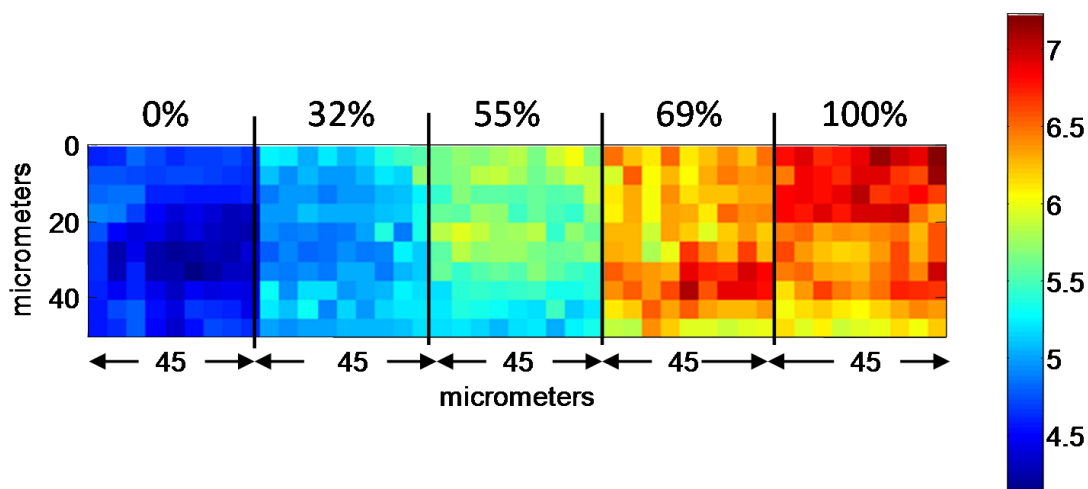
Fig. 2-4. Confocal Raman images of the integrated peak area ratio (988-898 cm^{-1}/ 922-898 cm^{-1}) at the labeled % RH values after exposure for >20H. At each RH, Raman spectra were acquired from an area of 45 x 45 μm^2 using a 5 μm step-size. The color bar for the area ratio values is shown to the right.

2.3.2 Raman measurements of H-D exchange in collagen

To better understand the spectral origin of the changes in the collagen doublet structure, a sample of Type I collagen initially hydrated at 100% RH in H_2O, was incubated with D_2O vapor for an increasing time period while Raman spectra were acquired. Duplicate experiments were conducted on sections of pigskin dermis and averaged spectra from the dermis at several time points are shown in Figure 2-5A and 5B. In each part of the figure, the bottom spectrum is of the H_2O equilibrated sample. The D_2O stretching region (2200-2800 cm^{-1}), displayed in Figure 2-5A, shows the time evolution of the contour as it becomes quite similar to that of pure liquid D_2O after several hours of exposure. Within the first 1.5 H of exposure to 100% RH D_2O, a broad band is observed at ~2510 cm^{-1} most likely due to the D-OH stretching mode[28, 29]. With increasing exposure time to D_2O, both the symmetric (~2410 cm^{-1}) and asymmetric (~2500 cm^{-1}) D-O-D stretching modes become dominant within this spectral region. The measured rate and extent of D_2O adsorption is presumably dependent on the size of the dermis section and the position from which the spectra are acquired. These parameters have been held constant in the current experiments and are described in the Experimental section. The intensity in the D-O-D stretching region is used as a measure of bulk H_2O to D_2O exchange in the sample (see Figure 2-6).

Significant changes are observed with increasing exposure time to D_2O in the lower wavenumber region (800-1680 cm^{-1}) of the dermal spectra shown in

Figure 5B. Upon long exposure time, the relative intensity of the 938 cm^{-1} band decreases in a manner similar to that observed when drying the sample (see Figure 2-2B). However, the intensity decrease is not accompanied by an upward shift in Amide I frequency as observed for dehydration (see Figure 2-2A). In contrast, a downward frequency shift in the position of the major Amide I mode from ~1665 to 1657 cm^{-1} is observed and is most likely due to H-D exchange in Amide I carbonyl hydrogen bonding. Furthermore, as exposure time increases, a decrease in intensity in the Amide III region (1230-1280 cm^{-1}) is observed concurrent with the development of a shoulder on the low frequency side of the phe ring stretching mode (1003 cm^{-1}). The shoulder in the 970-990 cm^{-1} region is assigned to the Amide III' mode (deuterated Amide III). The parallel evolution of these two spectral features is apparently a manifestation of N-H to N-D exchange. Although diffusion is likely the rate limiting step for the replacement of bulk phase H_2O with D_2O, the spectral changes based upon H-D exchange in hydrogen bonding and N-H to N-D exchange appear to take place more gradually over a relatively longer time period. To probe the temporal nature of these processes in more detail, relevant spectral parameters have been plotted as a function of D_2O exposure time in Figure 2-6.
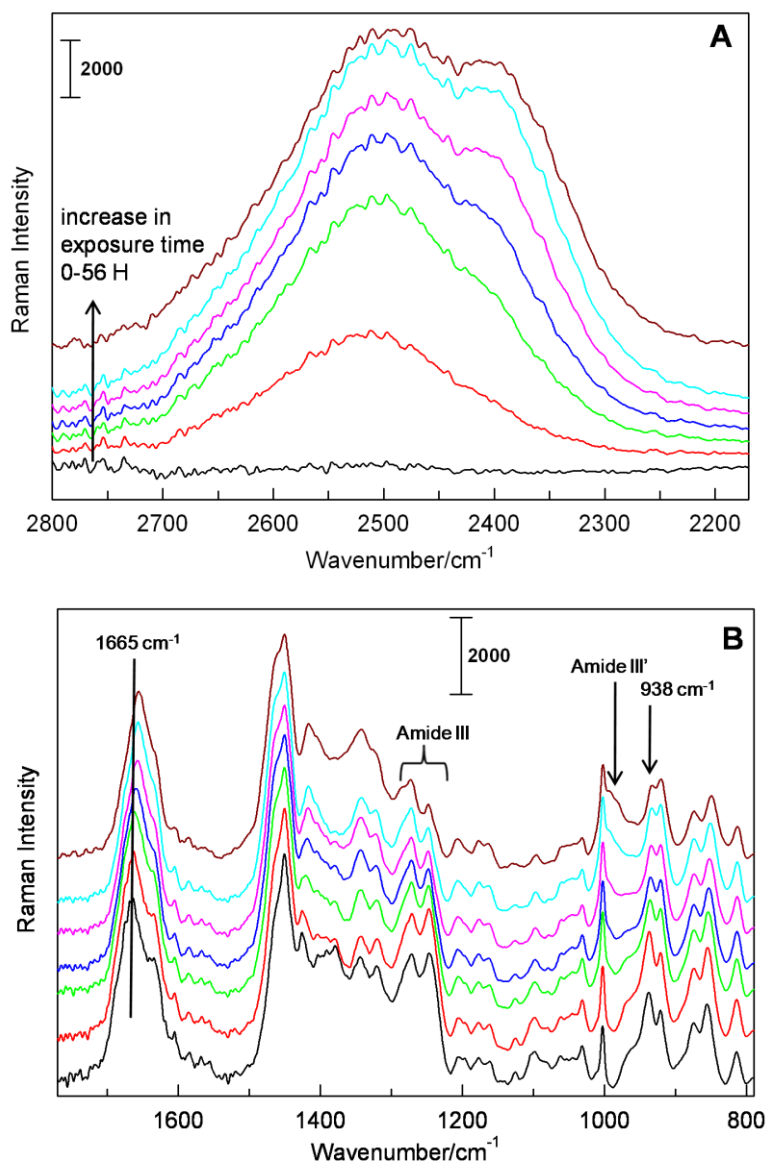
Fig. 2-5. Raman spectra of pigskin dermis upon exchange from exposure to 100% RH H_2O to D_2O. Spectra are averaged over increasing time periods (bottom to top): black, exposure to 100% RH H_2O for >20H; after exposure to 100% RH D_2O- red, 0-1.5H; green, 1.5-3.0H; blue, 3.0-4.0H; pink, 4.0-9.7H; cyan, 12.3-23H; brown, 43-56H. Spectra of: 5A. The D-O-D stretching region (2800-2160 cm^{-1}) and 5B. The fingerprint region (1780-790 cm^{-1}) with bands of interest marked. Spectra were baseline corrected and, for the fingerprint region, normalized to the 1450 cm^{-1} methyl bending mode.

The relative rate of the intensity increase in the D_2O stretching region is clearly faster than that observed for the Amide III diminution and Amide III' increase as displayed in Figure 2-6. It is also evident in the Figure that the collagen hydration parameter, based on the 938 cm^{-1} band, follows a time course similar to the N-H $\rightarrow$ N-D exchange. Thus, the hydration parameter appears to track the relative amount of bound as opposed to bulk water present in the dermis. The ability of the Raman measurement to differentiate bulk from bound water in dermal tissue is important in understanding the changes in hydration of aging skin and disease states.
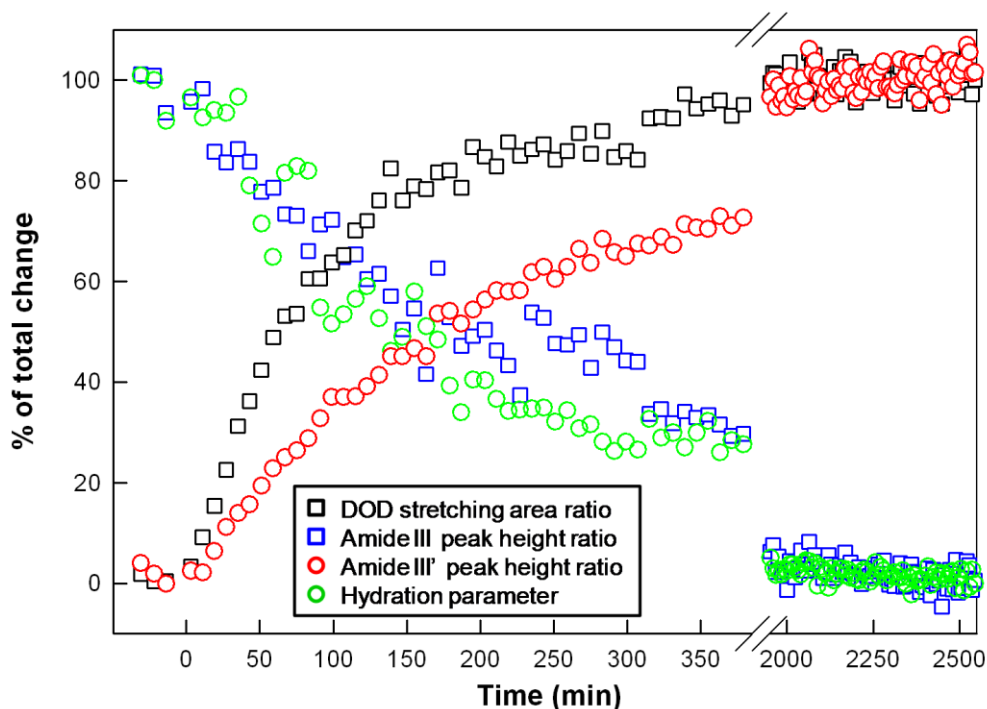
Fig. 2-6. The response of several Raman spectral features obtained from spectra of pigskin dermis as a function of time after exposure to a 100% RH D_2O environment depicted as % of total change. Black square: integrated area ratio of D_2O stretching region (2790-2175 cm^{-1}) / CH stretching region (3015-2825 cm^{-1}); blue square: peak height / integrated area ratio of Amide III component at 1248 cm^{-1} / CH stretching area; red circle: peak height / integrated area ratio of Amide III' component at 992 cm^{-1} / CH stretching area; and hydration parameter area ratio as defined in Figure 2-2.

It seems highly unlikely that a major structural change would occur in collagen upon exchange of H_2O to D_2O, especially given that large alterations in

Amide I and III band position and shape are not observed and those changes that are observed are consistent with H-D exchange. Xiao et al.[24] suggest that the intensity decrease in the 938 cm^{-1} band observed with increasing temperature is due to trans-cis isomerization in pro and hyp. ^{13}C-NMR experiments support their conclusion. It is possible that intensity in the 938 cm^{-1} band may be dependent on both hydration and isomerization.

Since liquid H_2O or D_2O lack Raman spectral features in the 850-980 cm^{-1} region, the origin of the sensitivity of the 938 cm^{-1} band intensity to RH and D_2O exposure must arise from collagen motions that are affected by interaction with water. The following tentative explanation relies on the Frushour and Koenig[22] assignment of the band to the ν(C-C) of the protein backbone. The actual normal modes are likely to contain contributions from other internal coordinates in addition to C-C stretches. A reasonable candidate for coupling to the C-C stretching internal coordinate in the normal mode is the N-C=O in-plane bending vibration depicted in Figure 2-7. It should be noted that although the ν(C-C) in Figure 2-7 is depicted for a hyp residue, it could just as well be shown for pro or gly. Hydration of the C=O bond with H_2O may alter both the in-plane bending frequency as well as vibrational coupling to the backbone C-C stretching internal coordinate resulting in an intensity increase. In contrast, hydration of the C=O with D_2O will cause a different alteration in the N-C=O bending force constant (due to both mass differences and altered hydrogen vs deuterium bond strength) and hence alter (reduce in the current case) the coupling between internal coordinates in the normal mode. The above model is evidently speculative.
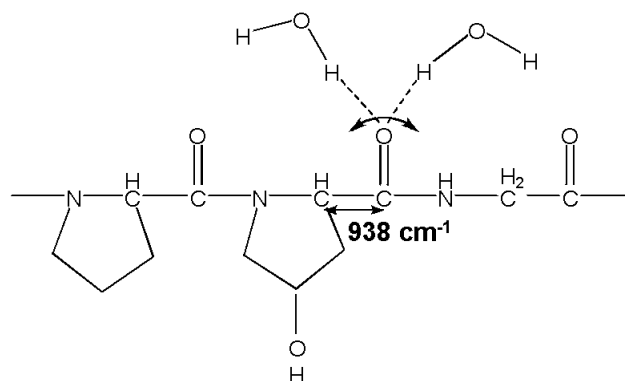
Fig. 2-7. Schematic of vibrational modes possibly involved in the RH-induced (and the H-D exchange-induced) intensity variation of the C-C stretching band at 938 cm^{-1}. The involvement of hydrogen-bonding is suggested to influence the coupling between the C-C stretching mode and the N-C=O in-plane bending mode.

2.3.3 DVS measurements of dermis

For the purposes of this study, the DVS experiments are best expressed using the Young and Nelson analysis[20] as described in the Methods section. Representative raw sorption and desorption data from a dermis section are displayed in the inset to Figure 2-8 and the component Young and Nelson plot fit to this dataset comprise the main part of Figure 2-8. From repetitive studies conducted as described in the Methods section, a range of quantitative results are obtained from the DVS experiments for absorbed water which falls between 0.5 – 0.9 mol H_2O/mol amino acid of collagen. The calculation assumes the typical ~1000 residue per individual polypeptide chain in a triple helix and a dermal collagen content of 80%. This range of absorbed water is slightly lower, but generally consistent with Gevorkian et.al.[29], where water content in rat tail tendon at 93% RH was reported at ~2 mol H_2O/mol amino acid and the hydration

networks of 1-3 mol H_2O/mol amino acid revealed in x-ray diffraction studies of collagen-like peptides[1, 30, 31].
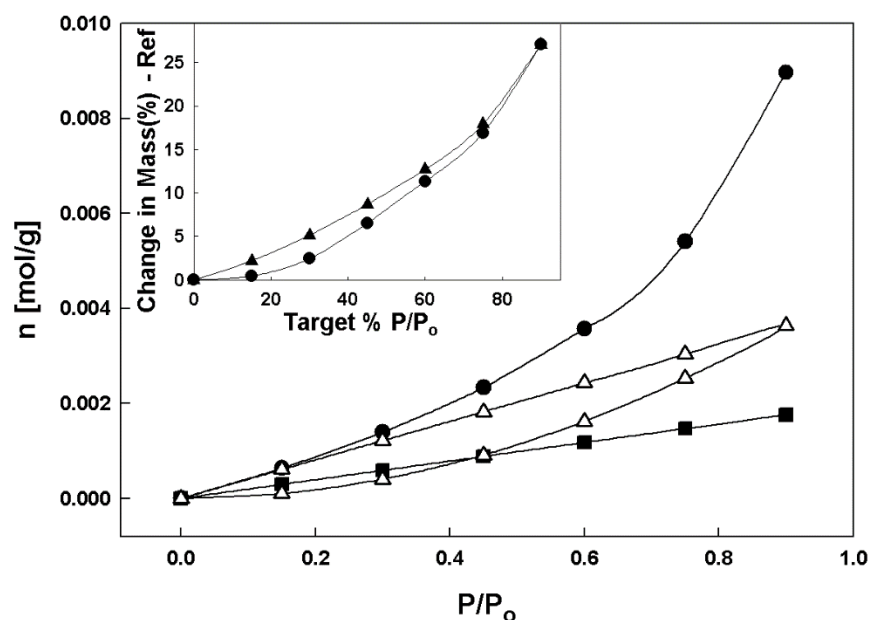
Fig. 2-8. DVS experimental results including the Young and Nelson component plot (see Materials and Methods) of a pigskin dermis sample dried for 24 H at 25°C and 0% RH, followed by an isothermal humidity ramp from 0-90% RH in 15% RH steps and desorption from 90-0% RH using the same decrements. Each sorption-desorption step was 24 H in duration to approximate gravimetric equilibration. Filled circles represent the adsorbed multilayer water, filled squares for adsorbed monolayer, and open triangles for absorbed and internal water. The inset shows the raw isotherm sorption (filled circle) and desorption (filled triangle) plot for the same sample.

It is interesting to compare the general form of the absorbed water plot in Figure 2-8 to that of the Raman hydration parameter plot in Figure 2-3 (open triangles). Whereas the Raman hydration parameter is thought to measure only dermal collagen-bound water molecules (see above), the absorbed water content obtained from DVS measurements likely includes bound and excess internal water. At lower RH, both datasets display concave curvature, fairly consistent with each other. Discrepancies could conceivably be anticipated under the experimental conditions applied, since complete removal of all integral water is unlikely and the Raman experiment is sampling only the outer ~50 μm of the

dermis. It is at roughly 70% RH where these two data sets appear to diverge. At greater than 70% RH the DVS plot continues to retain a concave form while the Raman area ratio plateaus to give the plot an overall sigmoidal shape. This divergence in response to RH may be reconciled when considering the difference in the area of the dermis sampled with each measurement and that the DVS measurement includes internal "free" water. In addition, the DVS experiment takes into account the many constituents of the dermis. Components such as elastin and fibrillin may bind water as well, reflected only in the DVS plot. Therefore given the potential multi-component make up of the absorbed water in the DVS experiment and the single component nature of the Raman band area ratio in Figure 2-3, the respective behaviors are quite reasonable.

2.4 Conclusions

Raman spectra were acquired of Type I collagen from human skin and intact pigskin dermis exposed to relative humidity conditions ranging from 0 to 100%. The relative intensity of the band centered at 938 cm^{-1} appears to directly track exposure to a range of RH values and the response is essentially reversible. Examination of the Amide I and Amide III bands in the Raman spectra at various RH values show no indication of major structural alterations under the applied experimental conditions. Raman spectra obtained at various time points during hydrogen-deuterium exchange experiments support the suggestion that the 938 cm^{-1} band intensity provides a measure of the collagen-bound water content. In contrast, DVS experiments of pigskin dermis provide a quantitative

measure of overall water content. Analysis of the DVS data by Young and Nelson's equations are used to distinguish three forms of moisture, i.e., a surface adsorbed monolayer, external adsorbed multilayers, and absorbed or internal moisture[20, 32]. One can envision how the work included herein may provide a baseline for future studies designed to probe alterations in collagen-bound and unbound water in dermal tissue exposed to a variety of external or internal stresses.

2.5 Reference

1. Bella, J.; Brodsky, B.; Berman, H. M., Hydration structure of a collagen peptide. *Structure* **1995,** 15, 893-906.
2. Rich, A.; Crick, F. H., *J. Mol. Biol.* **1961,** 3, 483-506.
3. Berisio, R.; Vitagliano, L.; Mazzarella, L.; Zagari, A., Crystal structure of a collagen-like polypeptide with repeating sequence pro-hyp-gly at 1.4 A resolution: Implications for collagen hydration. *Biopolymers* **2001,** 56, 8-13.
4. Kuznetsova, N.; Chi, S. L.; Leiken, S., Sugars and polyols inhibit fibrillogenesis of Type I collagen by disrupting hydrogen-bonded water bridges between the helices. *Biochemistry* **1998,** 37, 11888-11895.
5. Odland, G. F., Structure of the skin. In *Physiology, Biochemistry, and Molecular Biology of the Skin*, Goldsmith, L. A., Ed. Oxford University Press: New York, **1991,** I, 1-62.
6. Tobin, D. J., Biochemistry of human skin - our brain on the outside. *Chem. Soc. Rev.* **2006,** 35, 52-67.
7. Lavker, R. M., Cutaneous aging: chronologic versus photoaging. In *Photodamage*, Glichrest, B. A., Ed. Blackwell: New York, **1995,** 123-135.
8. Bernstein, E. F.; Chen, Y. Q.; Kopp, J. B.; Fisher, L.; Brown, D. B.; Hahn, P. J.; Robey, F. A.; Lakkakorpi, J.; Uitto, J., Long-term sun exposure alters the collagen of the papillary dermis. *J. Am. Acad. Dermatol.* **1996,** 34, 209-218.
9. Cowper, S. E.; Robin, H. S.; Steinberg, S. M.; Su, L. D.; Gupta, S.; LeBoit, P. E., Scleromyxoedema-like cutaneous diseases in renal-dialysis patients. *The Lancet* **2000,** 356, 1000-1001.
10. Gniadecka, M.; Nielsen, O. F.; Wessel, S.; Heidenheim, M.; Christensen, D. H.; Wulf, H. C., Water and protein structure in photoaged and chronically aged skin. *J. Invest. Dermatol.* **1998,** 111, 1129-1133.

11. Nakagawa, N.; Matsumoto, M.; Sakai, S., In vivo measurement of the water content in the dermis by confocal Raman spectroscopy. *Skin Res. Tech.* **2010,** 16, 137-141.

12. Wright, A. C.; Bohning, D. E.; Pecheny, A. P.; Spicer, K. M., Magnetic resonance chemical shift microimaging of aging human skin in vivo: initial findings. *Skin Res. Tech.* **1998,** 4, 55-62.

13. Richard, S.; Querleuz, B.; Bittoun, J.; Jolivet, O.; Idy-Peretti, I.; Delacharriere, O.; Leveque, J. L., Characterization of the skin in vivo by high-resolution magnetic-resonance imaging - water behavior and age-related effects. *J. Invest. Dermatol.* **1993,** 100, 705-709.

14. Zhang, G.; Moore, D. J.; Sloan, K. B.; Flach, C. R.; Mendelsohn, R., Imaging the prodrug-to-drug transformation of a 5-Fluorouracil derivative in skin by confocal Raman microscopy. *J. Invest. Dermatol.* **2007,** 127, 1205-1209.

15. Zhang, G.; Flach, C. R.; Mendelsohn, R., Tracking the dephosphorylation of resveratrol triphosphate in skin by confocal Raman microscopy. *J. Control. Release* **2007,** 123, 141-147.

16. Tfayli, A.; Piot, O.; Pitre, F.; Manfait, M., Follow-up of drug permeation through excised human skin with confocal Raman microspectroscopy. In *Eur Biophys J*, **2007**; 36, 1049-1058.

17. Eikje, N. S.; Aizawa, K.; Ozaki, Y., Vibrational spectroscopy for molecular characterization and diagnosis of benign, premalignant and malignant skin tumours. In *Biotechnology Annual Review*, El-Gewely, M. R., Ed. Elsevier B. V.: Amsterdam, **2005,** 11, 191-225.

18. Krafft, C.; Steiner, G.; Beleites, C.; Salzer, R., Disease recognition and Raman spectroscopy. *J. Biophotonics* **2009,** 2, 13-28.

19. Caspers, P. J.; Lucassen, G. W.; Carter, E. A.; Bruining, H. A.; Puppels, G. J., In vivo confocal Raman microspectroscopy of the skin: Noninvasive determination of molecular concentration profiles. *J Invest Dermatol* **2001,** 116, 434-441.

20. Young, J. H.; Nelson, G. L., Theory of hysteresis between sorption and desorption isotherms in biological materials. *Trans. Am. Soc. Agric. Eng.* **1967,** 10, 260-263.

21. Young, J. H.; Nelson, G. L., *Trans. Am. Soc. Agric. Eng.* **1967,** 10, 756-761.

22. Frushour, B. G.; Koenig, J. L., Raman scattering of collagen, gelatin, and elastin. *Biopolymers* **1975,** 14, 379-391.

23. Diem, M.; Bhatnagar, R. S.; Druyan, M. E.; Renugopalakrishnan, V., Solution-phase Raman-spectroscopic studies on synthetic collagen analogs: prolyl-prolyl-glycine and (prolyl-prolyl-glycine)10. *Biopolymers* **1984,** 23, 2955-2961.

24. Xiao, Y.; Guo, M.; Zhang, P.; Shanmugam, G.; Polavarapu, P. L.; Hutson, M. S., Wavelength-dependent conformational changes in collagen after mid-infrared laser ablation of cornea. *Biophys. J.* **2008,** 94, 1359-1366.

25. Miles, C. A.; Ghelashvili, M., Polymer-in-a-box mechanism of the thermal stabilization of collagen molecules in fibers. *Biophys. J.* **1999,** 76, 3243-3252.

26. Susi, H.; Ard, J. S.; Carroll, R. J., The infrared spectrum and water binding of collagen as a function of relative humidity. *Biopolymers* **1971,** 10, 1597-1604.

27. Mendelsohn, R.; Mantsch, H. H., Fourier transform infrared studies of lipid-protein interaction. In *Progress in Protein-Lipid Interaction. Vol. 2*, Watts, A.; de Pont, J. J. H. M., Eds. Elsevier: Amsterdam, **1986,** 103-146.

28. Murphy, W. F.; Bernstein, H. J., Raman spectra and an assignment of the vibrational stretching region of water. *J. Phys. Chem.* **1972,** 76, 1147-1157.

29. Gevorkian, S. G.; Allahverdyan, A. E.; Gevorgyan, D. S.; Simonian, A. L., Thermal (in)stability of Type I collagen fibers. *Phys. Rev. Lett.* **2009,** 102, 048101-1-048101-4.

30. Bella, J.; Eaton, M.; Brodsky, B.; Berman, H. M., Crystal and molecular structure of a collagen-like peptide at 1.9 angstrom resolution. *Science* **1994,** 266, 75-81.

31. Kramer, R. Z.; Bello, J.; Mayville, P.; Brodsky, B.; Berman, H. M., Sequence dependent conformational variations of collagen triple-helical structure. *Nat. Struct. Biol.* **1999,** 6, 454-457.

32. Agrawal, A. M.; Manek, R. V.; Kolling, W. M.; Neau, S. H., Water distribution studies within microcrystalline cellulose and chitosan using differential scanning calorimetry and dynamic vapor sorption analysis. *J. Pharm. Sci.* **2004,** 93, 1766-1779.

Chapter 3: Infrared Spectroscopic Imaging Tracks Lateral Diffusion in Human Stratum Corneum

3.1 Introduction:

The majority of percutaneous penetration/permeation studies have focused on the ability of a substance to cross the stratum corneum (SC) barrier giving little consideration to competitive spreading and lateral diffusion that may take place simultaneously on the surface and within the SC, respectively. Along with these processes, the potential exists for the formation of a drug depot or reservoir in the SC which may have important consequences regarding dosing and controlled or timed-release[1, 2]. Lateral diffusion within the top layers of the SC and radial spreading mechanisms along surface furrows or glyphs are poorly defined although this information is of substantial pharmacological, toxicological, and cosmetic importance.

The basic structure of the SC, often depicted as bricks and mortar, mainly consists of anucleated keratin-rich corneocytes embedded in a continuous multi-lamellar lipid network. If permeant transport through skin appendages (hair follicles and glands) is ignored, diffusion in the SC is thought to take place via intercellular and/or transcellular routes. Exogenous agent solubility in the SC lipid matrix and/or binding to keratin in corneocytes may limit the bioavailability of substances. Transport routes across and within the SC mostly depend on the size and lipophilicity of the exogenous agent[3]. It is generally accepted that lipophilic compounds follow an intercellular route through the lipid matrix whereas hydrophilic compounds may diffuse through corneocytes and the lipid matrix, possibly including an aqueous pore pathway[1, 4, 5].

Fluorescence-based techniques have been used to track lateral diffusion of substances in both SC lipid models and in isolated SC. Fluorescence recovery after photobleaching (FRAP), employed for three decades to measure diffusion coefficients in membrane-related systems, was used by Langer and co-workers[6] to measure the lateral diffusion of a series of nine fluorescence probes in extracted SC lipids. They derived diffusion coefficients ranging from 0.306×10^{-8} to 2.34×10^{-8} cm^2/sec depending on probe molecular weight. More recently, fluorescence multiphoton tomography was employed in FRAP experiments performed on human SC in vitro[7]. With this approach, micron-sized scales are realized for the photobleached volume. In another study, Raster image correlation spectroscopy (RICS) based on multiphoton excitation fluorescence was used to evaluate local diffusion coefficients in excised human skin[8]. Spatially resolved images of lateral diffusion coefficients were generated at different depths in the SC using amphiphilic and hydrophilic fluorescently-labeled molecules. Diffusion in the SC was found to be very heterogeneous on a microscopic scale. Despite the substantial sensitivity of these techniques, there are some limitations for their usefulness in understanding lateral diffusion mechanisms in skin. First, the experiments evidently require the presence of a fluorescent moiety which could have significant effects on molecular diffusion, especially in the heterogeneous environments of skin. Second, the use of fluorescence microscopy does not provide molecular structure information about the skin microenvironment, e.g., fluorophore-induced structural changes in the molecular constituents of skin.

Tape stripping protocols with appropriate analytical methods have also been employed for monitoring lateral diffusion in SC. Early reports reveal differences in lateral diffusion versus depth of active agent penetration dependent on the delivery vehicle[9, 10]. More recently, Jacobi et al.[11] investigated the *in vivo* lateral spreading of UV filter substances and reported significant amounts in adjoining areas that takes place via spreading on the surface. Along similar lines, Schicksnus and Muller-Goymann[12] extracted concentric skin segments surrounding the site of application of ibuprofen to skin. Using HPLC detection, two phases of lateral diffusion were observed; accumulation in the central segment, followed by redistribution. In a recent extension of this experiment, Gee et al.[13] used a similar concentric tape stripping method to track both lateral spreading and SC penetration of caffeine, hydrocortisone and ibuprofen *in vivo.* They reported that lateral spreading behavior depends on the physicochemical properties of the applied drugs. The permeant with smallest log P value (caffeine), rapidly diffused laterally within the top SC lipid bilayers whereas, the most lipophilic permeant, ibuprofen, quickly exhibited both a wide and deep drug depot.

It is noted that the presence of furrows in the skin (glyphs) may invalidate the conclusions drawn from tape stripping experiments. Van der Molen et al.[14] reported the presence of non-stripped skin in the furrows after tape stripping 20 times. Indeed, glyphs have been shown to function as pathways for lateral spreading of topically applied substances[15, 16] while their density and distribution vary with body site, age and environmental exposure[15, 17, 18]. Hence, the influence

of glyph distribution on lateral diffusion/spreading is not only an important experimental issue, but also has implications for pharmacology, toxicology, and cosmetics.

Vibrational spectroscopy-based methods (i.e. Fourier transform infrared (FT-IR) and Raman spectroscopies) offer some generic advantages compared to the fluorescence-based methods discussed above. As is well known, vibrational spectra provide molecular structure information from endogenous skin components in addition to the exogenous material whose diffusion is being monitored. Over the past twenty years, the development of both IR microspectroscopic imaging and confocal Raman microscopy have proven the feasibility of acquiring spatially resolved spectra from microtomed skin sections and intact skin, respectively. Several studies from our lab and others[19-24] have demonstrated the utility of the approach. Penetration of exogenous agents is conveniently tracked from the spatial distribution of their vibrational band intensities. Although IR microscopic imaging has not been previously used to measure lateral diffusion kinetics in skin, studies demonstrating the feasibility of the experiment have indeed appeared. Gotter et al.[25] investigated the heterogeneous lateral distribution of the anti-psoriasis drug dithranol in an artificial membrane. From our laboratories, Mao et al.[26] imaged the distribution of sodium dodecyl sulphate (SDS) across different skin regions. A useful advantage of IR imaging was realized from the fact that Beer's Law is obeyed in the IR, thereby permitting (in the example cited above) the determination of the SDS concentrations in the skin.

In the current study, we demonstrate the feasibility of mapping lateral spreading/diffusion in human SC with IR imaging. We image the spatial distribution and concentration of deuterated variants of the common permeation enhancers, oleic acid (OA) and dimethyl sulfoxide (DMSO). The use of acyl chain perdeuterated OA (OA-d) and methyl group deuterated DMSO (DMSO-d) permits us to spectroscopically distinguish the exogenous agents from the endogenous SC lipids without affecting penetration parameters. In addition to providing a temporal and spatial quantitative measure of OA concentration along networked furrows on the SC surface, images are generated for both permeants in relatively glyph-free regions. A range of diffusion coefficients for lateral transport based on Fick's second law are compared to the imaging data. Although the results do not directly distinguish between permeant spreading on the surface and that diffusing within the SC, the unique capabilities of IR spectroscopy permit us to detect perturbation to endogenous SC keratin structure for the DMSO experiments and changes in the OA spectra consistent with penetration and lateral diffusion.

3.2 Materials and methods:

3.2.1 Materials:

Trypsin (Type II-S from porcine pancreas), phosphate buffered saline, and perdeuterated oleic acid-d_{34} (OA-d), 98 atom % D were purchased from Sigma-Aldrich (St. Louis, MO). Dimethyl-d_6 sulfoxide (DMSO-d) was purchased from CDN Isotopes, Inc. (Quebec, Canada). Human abdominal skin (otherwise to be discarded) from plastic surgery procedures, was obtained from dermatological offices following informed consent and approval of the institutional ethics

committee. Samples were fast frozen with liquid nitrogen after removal of subcutaneous fat, cut into about 15 X 15 cm^2 pieces, and stored at -20°C for six months or less.

3.2.2 Methods:

Isolation of SC.

Skin samples of ~1 x 2 cm^2 surface area and thickness of ~2.5 mm were cut from a larger piece and defrosted on filter paper with the SC side up. The SC was cleaned with cotton swabs to remove surface fat, tape-stripped twice to remove most of the sebum, and then treated with 0.5% (w/v) trypsin buffer solution for 24 hours at room temperature. The SC was isolated by peeling from the viable epidermis, rinsed with distilled water and then hair was removed. The SC was cut to the desired size, transferred onto a ZnSe IR window, and dried overnight under house vacuum.

IR Microscopic Imaging.

IR images of skin were collected with a Perkin-Elmer Spotlight 300 system (PerkinElmer Life and Analytical Science, Inc., Waltham, MA) with an essentially linear array (16 X 1) of mercury-cadmium-telluride (MCT) detector elements. The imaging protocol was to first acquire a control IR image of the SC prior to the application of either OA-d or DMSO-d. Most of the IR images were collected utilizing the transmission mode with a 25 X 25 μm^2 pixel size and 32 scans at a spectral resolution of 2 cm^{-1}. Occasionally an image was acquired using a 6.25 X 6.25 μm^2 pixel size (32 scans and spectral resolution of 8 cm^{-1}). Next, a finite application of 0.3 μL of OA-d or DMSO-d (the size of the drop was ~1.8-2.0 mm

in diameter) was applied with the edge of the drop close to the imaging area used for the control image. The geometry of the set-up is shown in Figure 1 where the visible micrograph of the SC appears yellow due to the ZnSe IR window. Finally, IR images were acquired as a function of time for 20-50 H after application. Each image required 1-2 H for acquisition and is labeled at the time image acquisition began. Experiments were repeated 3-4 times; typical data are presented. Image sizes were ~1600 X 800 μm^2, corresponding to 64 pixels in the x direction and 32 pixels in the y direction. Visible micrographs were obtained with the microscope integrated into the Spotlight 300 system.

Determination of IR Extinction Coefficients of OA-d and DMSO-d.

OA-d was dissolved at known concentrations in methanol, octane and octanol. A fixed pathlength (15 μm) IR cell with CaF_2 windows was used to measure the absorbance of each standard. IR spectra were acquired with a Nicolet 6700 spectrometer (Thermo Electron Corporation, Madison, Wisconsin), 128 scans and using a spectral resolution of 2 cm^{-1}. A graph of the area of the symmetric CD_2 stretching ($\nu_{sym}CD_2$) band (obtained using ISys 3.1 software, Malvern Instruments, UK) as a function of molar concentration was plotted. Linear regression was used to find the best fit lines to the Beer's Law plots. The extinction coefficients (mol^{-1} dm^3 cm^{-1}) and correlation coefficients are as follows: methanol, 5653, 0.987; octane, 5222; 0.999 and octanol 6010, 0.996. The average of the three measured extinction coefficient values was used for quantitative analysis. When calculating OA-d concentration, we assume that the thickness (pathlength) of isolated human SC samples is 15 μm. A similar

procedure was used to determine the extinction coefficient and concentration for DMSO-d based on the area of the asymmetric CD_3 stretching band. The extinction coefficients (mol^{-1} dm^3 cm^{-1}) and correlation coefficients are as follows: octanol, 201.8, 0.996 and propanol, 198.6, 0.999, respectively. The correlation coefficients demonstrate the high precision of using the symmetric CD_2 and asymmetric CD_3 stretching band areas to calculate OA-d and DMSO-d concentration in skin, respectively.

IR Imaging Data Analysis.

Vibrational microspectroscopic images were generated from IR spectral data using ISys 3.1 software (Malvern Instruments, UK). Image planes of spectral parameters (integrated peak areas, area ratios, and center of mass (COM) peak frequencies) were produced after linear baselines were applied in spectral regions of interest. Image planes of OA-d and DMSO-d concentrations were generated after applying the averaged extinction coefficient. Figures were generated with SigmaPlot 2000 (SPSS Inc., Chicago, IL).

Estimation of Diffusion Coefficients.

The two dimensional diffusion equation is given as follows, assuming the diffusion coefficient, D, is constant and [C] is the concentration of the diffusing molecule:

$$\frac{\partial^2 [C]}{\partial x^2} + \frac{\partial^2 [C]}{\partial y^2} = \frac{1}{D} \frac{\partial [C]}{\partial t}$$

The concentration at a distance "r" where r = $(x^2 + y^2)^{1/2}$ from a point source on an infinite plane is given by:

$$[C] = \frac{M}{4\pi Dt} e^{\left(-r^2/(4Dt)\right)}$$

where M is the total amount of the diffusing substance and t is time. When an instantaneous cylindrical source with a radius (r) of 1000 μm (as observed in our experiments) is left to diffuse throughout an infinite plane surface, Crank [27] has shown the corresponding result to be:

$$\frac{C}{C_o} = \frac{1}{2Dt} e^{\left(-r^2/(4Dt)\right)} \int_0^{1000} \{e^{\left(-w^2/(4Dt)\right)} I_o \,(rw/2Dt)\} w dw$$

where I_o is the modified Bessel function of the first kind of order zero, with an argument of (rw/(2Dt)) and C_o is the initial concentration. The equation was evaluated with Mathcad 2001 (PTC, Needham, MA).

Determination of initial concentration.

A solution of molar ratio of 1:19 deuterated oleic acid:protonated oleic acid was prepared to measure initial OA-d concentration. 0.3 μL of the solution was placed on a piece of isolated SC and a visible image of the drop was taken using the Spotlight instrument. Infrared spectra (point mode, aperture size: 100 μm^2) were acquired at a series of points inside the OA drop. The integrated area of the $\nu_{sym}CD_2$ band was calculated at each point and then averaged (A). The radius of the OA drop was measured from the visible image. Assuming the drop is a perfect cylinder, the height of the cylinder which is the pathlength (l), can be calculated based on the volume and area. According to Beer's law, the initial concentration was calculated from: C_o = (A/(E_xl))F, where E_x is the molar extinction coefficient and F is an adjustment factor based on the molar ratio (total moles/OA-d moles) of 20. This molar ratio was chosen to keep the $\nu_{sym}CD_2$ band

on scale based on the IR imaging detector sensitivity. A similar procedure was used to determine the initial concentration of DMSO-d.

3.3 Results:

A schematic depiction of the IR imaging lateral diffusion experiment, overlaid on a visible micrograph of the SC, is shown in Figure 3-1. The typical area over which IR spectra are acquired is ~0.5 mm x 1.0 mm. OA-d was applied as a 0.3 μL drop (pure liquid). Usually, the front edge of the source drop is ~300 μm away from the area of the rectangular IR image plane; however occasionally the source drop area overlapped this image plane. As is evident in the figure, separate regions of the SC appear to be nearly furrow-free or contain several networked furrows. Data is presented herein from both regions, although we cannot rule out that smaller, non-visible glyphs may be present in the glyph-poor areas. Representative radial distances from the center of the source over which diffusion coefficients in a glyph-poor area were evaluated are marked in the figure.

3.3.1 OA-d diffusion experiments.

IR and visible images were collected from the same area as a function of time following application of the OA-d drop to the SC surface. Representative spectra depicting the appearance of OA-d at a particular site at a few time points following application to the surface are shown in Figure 3-2A. Important spectral features are labeled in the Figure. The spectra are of high quality depicting a S/N ratio of ~200 for the Amide II vibration near 1550 cm^{-1}. Of particular interest in the evaluation of the diffusion process is the time evolution of the spectral

intensity in the CD_2/CD_3 stretching region (2000-2300 cm^{-1}). This spectral region is shown enlarged in Figure 3-2B for spectra acquired at 0, 4.5, 24.5, and 50.5 H (top to bottom) following application. The integrated band intensity of $\nu_{sym}CD_2$ (~2100 cm^{-1}) was used to determine the concentration of OA-d (as described in the Experimental section).
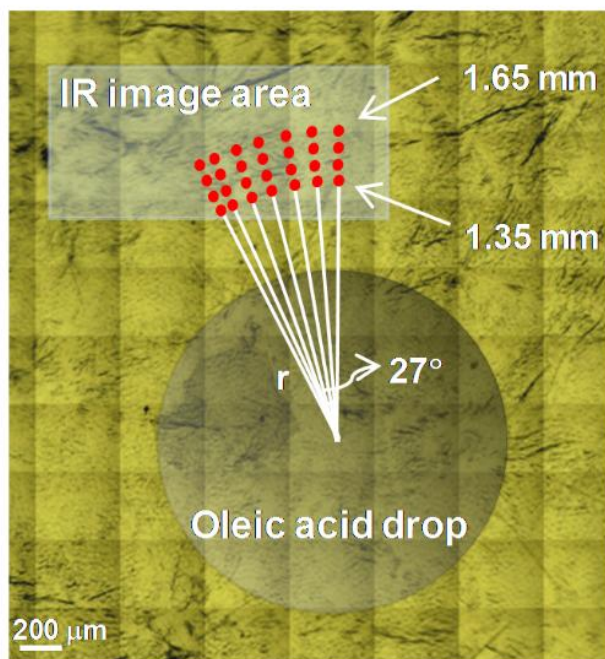
Fig. 3-1. Geometry of the experimental design and schematic of averaging the oleic acid-d concentration at various distances (1.35-1.65 mm) from the center of the source in a glyph-poor area. The schematic is shown on a visible image of isolated human SC on top of an IR ZnSe window.

Several IR images displaying the spatial distribution of the OA-d concentration on and/or within the isolated SC as a function of time after application are shown in Figure 3-3. A visible image of this glyph-rich region of the SC acquired before the OA-d was applied is included in the figure. The source droplet was applied with its edge ~0.2 mm from the bottom left-side of the image area as depicted in Figure 3-3. It appears, from the very high OA-d concentrations in the lower portion of the images, that the droplet of OA-d has

spread into the imaged area (most likely between 5-11H) during IR data acquisition. Since spectra were collected in the transmission mode, the peak intensities obey Beer's law. Color codings are converted to oleic acid concentrations as depicted on the scale bar in the figure. The scale bar upper range has been manually set to highlight concentration variations in the IR images that track the glyphs shown in the visible micrographs. An overlay of the visible image in the top row (transparent) with a concentration image taken at 55 H is displayed in the bottom row (right) with the intent of emphasizing the manner in which the concentration profile follows the glyph network in the SC. The time evolution of the concentration images suggests that the OA-d is wicking or spreading predominantly within the grooved glyphs of the SC. At early times (< 8 H), OA-d is first observed to spread into the vertical furrow in the bottom left-hand side of the visible image. At times ≥ 8.5 H, the presence of OA-d becomes apparent in a second glyph on the bottom right. As the concentration of OA-d increases to ≥ 0.4M in the lower portion of the image (≥ 8.5 H), the glyph network in the top portion begins to fill with OA-d, reaching concentrations of ~0.15M at ≥ 27.5 H. Concentration profiles in glyph-rich areas were explored further.
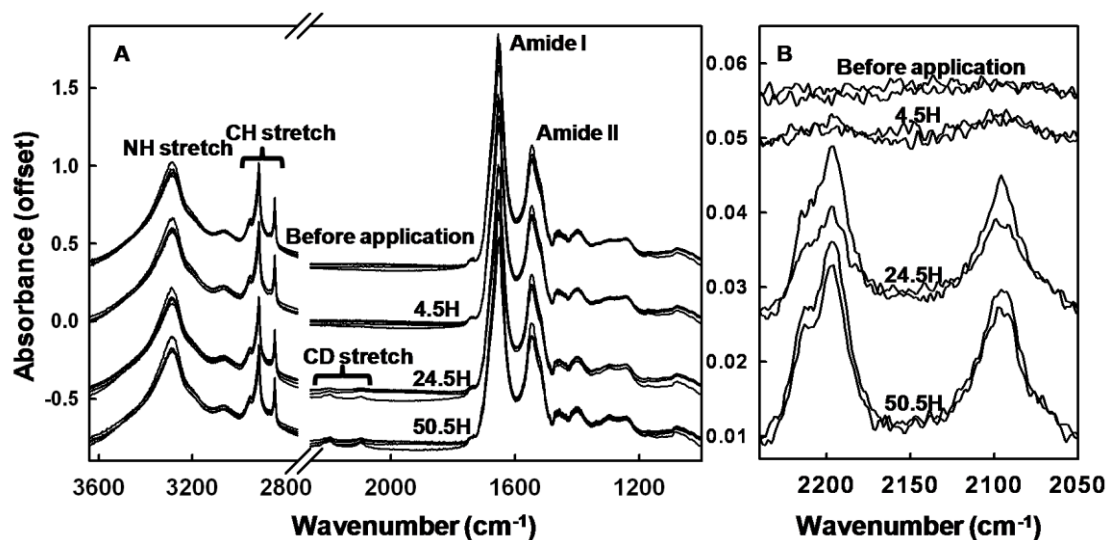
Fig. 3-2. Overlaid, unprocessed, single pixel (25 μm^2) IR spectra of OA-d treated SC at 1.35 mm from the center of the source in a glyph-poor area. 2A: representative spectra offset at 0, 4.5, 24.5 and 50.5 H following OA-d application. Spectral features of interest are labeled. 2B: Similar spectra as shown in (2A) highlighting the CD_2 stretching region (2050-2240 cm^{-1}). The spectra are baseline corrected at 2250 and 2059 cm^{-1}.

OA-d concentration along a nearly continuous set of furrows, as shown in the visible image in Figure 3-4A (visible image from Figure 3-3 is cropped and rotated with source droplet located at left side), is displayed in Figure 3-4B as a function of distance from the source and time after application. There are a few regions within the glyphs at specific distances from the source center (black arrows at ~1.45, 1.85, and 1.95 mm) that appear to go through a concentration maximum with time, at 30.5 H. The visible image is the darkest at these locations which may reflect a maximum depth in the glyphs at these particular points. An additional upsurge in concentration is evident at earlier time points for the 1.45 mm distance at 8.5-11 H. The stabilizing of OA-d concentration to ~0.15M (as noted above) is evident for the two longest time points over a range of distance from the source (1.55-1.95mm).
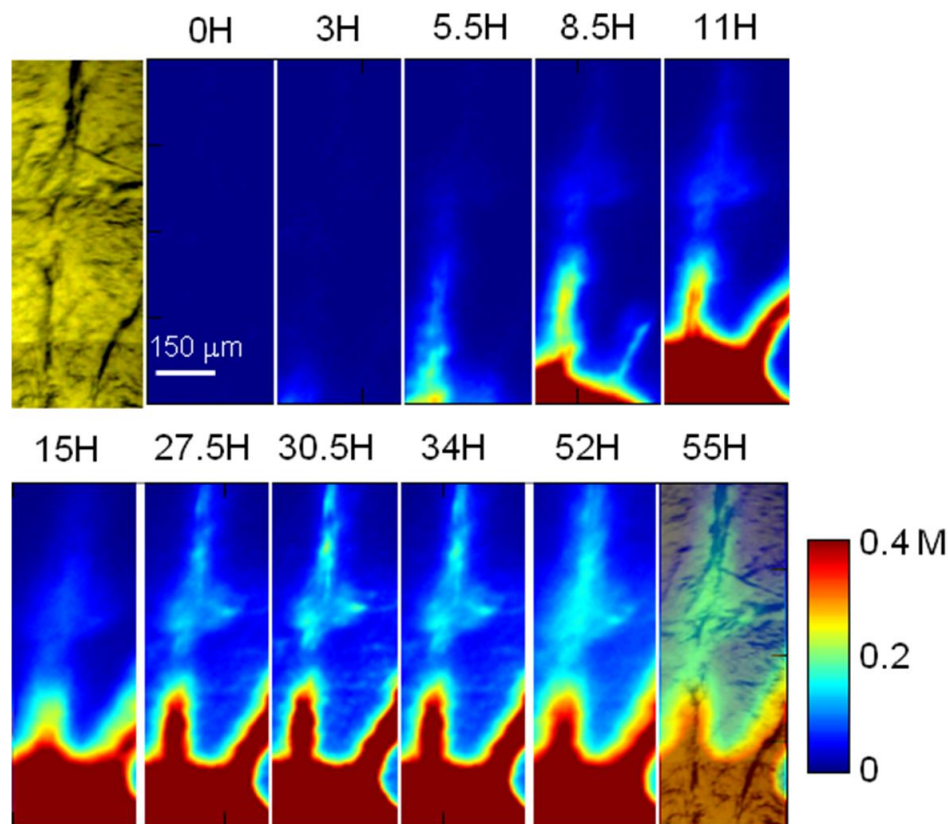
Fig. 3-3. IR images of OA-d concentration as function of time in a glyph-rich area (6.25 μm^2 pixel size). The source droplet was applied with its edge ~0.2 mm from the bottom left-side of the image area. The concentration range of 0-0.4 M is shown for better viewing of OA-d diffusion within the glyphs. The concentration of OA-d is calculated based on the symmetric CD_2 stretching band area according to Beer's Law. The 2059-2132 cm^{-1} region is baseline corrected and integrated. The image size is 0.30 X 0.80 mm^2. The visible image of the SC (top left) is taken before OA-d application. An overlay of the visible image (transparent) with a concentration image taken at 55 H is displayed in the bottom row (right).

Concentration profiles are plotted across a glyph at the same distance from the source center (~1.4 mm) in an attempt to evaluate whether transport along a glyph can be discerned from diffusion within the SC lipid layers. The red line in the visible image (Figure 3-4A) marks the approximate location of those spectral pixels chosen for the concentration profiles shown in Figure 3-4C. At this location, the approximate width of the furrow appears to be ~20 μm in the visible image. As observed in Figure 3-4C, OA-d concentrations are strongly influenced by the presence of the glyph within 20 μm of its center, reaching a maximum at

30.5 H, as mentioned above for concentration within the glyph area. The influence is not as strong at 31.3 μm away from the center and at greater distances the temporal concentration behavior appears to have two phases. There is a relatively rapid initial increase in concentration from 0-15 H, followed by a slower rate of increase for the remainder of the experiment. It is tempting to speculate that at distances greater than ~30 μm from the glyph center, the OA-d has penetrated into the SC to the point that the temporal concentration profiles are governed by its lateral diffusion within the SC lipid layers. This point will be expanded upon in the Discussion.
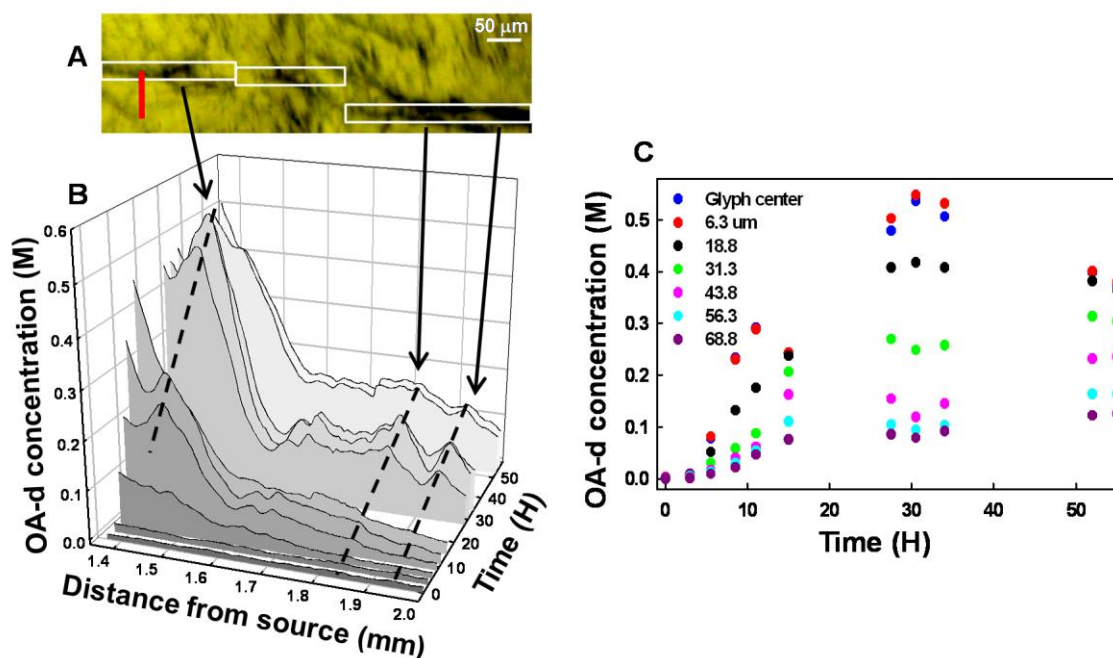
Fig. 3-4. OA-d concentration as function of time and distance from the source in glyph-rich regions. 4A: The visible image of the SC from Figure 3-3 has been cropped and rotated to facilitate comparison of glyph locations with the concentration plot shown in 4B. The center of the OA-d droplet was located at ~1.37mm from the left-hand edge of the cropped image. 4B: Three dimensional plot of OA-d concentration as function of time and distance from the source center along glyphs. The plotted concentrations are averaged across three pixels (shown within the white rectangles in 4A). The arrows and dashed lines are shown to guide the eye (see text). 4C: OA-d concentration as function of time at several distances from glyph center (position shown as red line in A), all ~1.4mm from the source center.

IR images presented in Figure 3-5A display the time evolution of OA-d concentration for a lateral diffusion experiment in a SC region that is relatively glyph-free. The edge of the source droplet in this experiment is located ~200 μm below the right hand side of the IR image area as shown in Figure 3-1 and its shape does not appear to change over the time period of the experiment. OA-d can be observed diffusing into the lower right hand portion of the IR image within the first 2 H after application (Figure 3-5A). As the spatial distribution of OA-d concentration increases with time, a finger-like feature of relatively high OA-d concentration is initially observed at ~ 22 H (white arrow), spatially aligned with a small glyph in the lower right hand corner of the visible image (not shown). The projection remains as a distinct area of higher concentration until the concentration in the surrounding area increases (at times $\geq$ 47 H) to approximately the same level ($\geq$ 0.05 M). Figure 3-5B displays averaged OA-d concentration as a function of time for particular distances from the source as delineated in Figure 3-1. Each concentration value is averaged from ~30 spectra for each time period. It is likely that the "error" bars (standard deviation) predominantly reflect concentration differences due to the native heterogeneity of the SC. In addition, it is readily apparent that the OA-d concentrations in the glyph-poor areas are at least an order of magnitude less than those in the glyph-rich areas for comparable distances from the source (compare to Figure 3-4B).
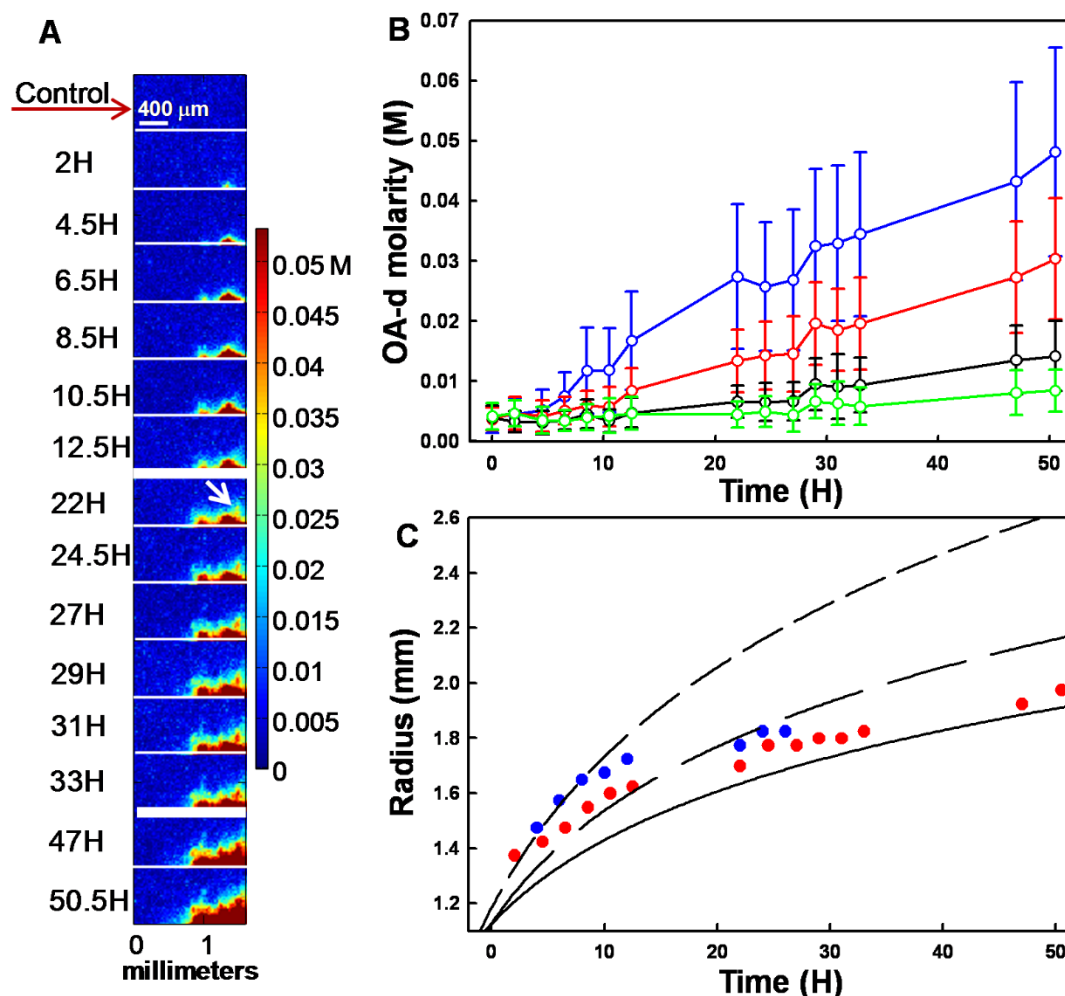
Fig. 3-5. OA-d concentration as function of time in a relatively glyph-free area. 5A: IR images (1.60 X 0.80 mm^2) displaying the time evolution of OA-d concentration. The edge of the source droplet is ~0.2mm below the bottom right-hand side of the image. The white arrow in the image at 22 H marks a finger-like feature possibly due to a small glyph. 5B: Averaged OA-d concentration (± standard deviation) as function of time at particular distances from the source center. Each concentration is the average of ~30 pixels as depicted in Figure 1 for each distance from the source center (in mm): blue: 1.35; red: 1.45; black: 1.55; green: 1.65. 5C: The expanding radius of oleic acid due to diffusion as a function of time for duplicate experiments (red and blue filled circles) compared to a range of diffusion coefficients obtained from Crank's solution of Fick's second law for lateral diffusion in two dimensions (see Methods section for details). The radii values are obtained based on OA-d detection limit of 5mM. Diffusion coefficients are as follow: solid line, 0.3e-8 cm^2/s; long dashed line, 0.5e-8 cm^2/s; short dashed line, 1.0e-8 cm^2/s.

IR images of OA-d concentration in glyph-poor areas were analyzed further and compared to results from Crank's solution of lateral diffusion in two dimensions[27] to obtain a range of diffusion coefficients which best describe the experimental data. The outcome is plotted in Figure 3-5C as radius vs. time. The

OA-d detection limit of 5mM based on the $\nu_{sym}CD_2$ band was used to obtain the radii values shown in the graph. The experimental results are essentially bracketed by the calculated values shown in the figure. The diffusion coefficient that best fits the experimental data appears to decrease with time; from ~1 x 10^{-8} cm^2/s for shorter times to ~3 x 10^{-9} cm^2/s for longer times.
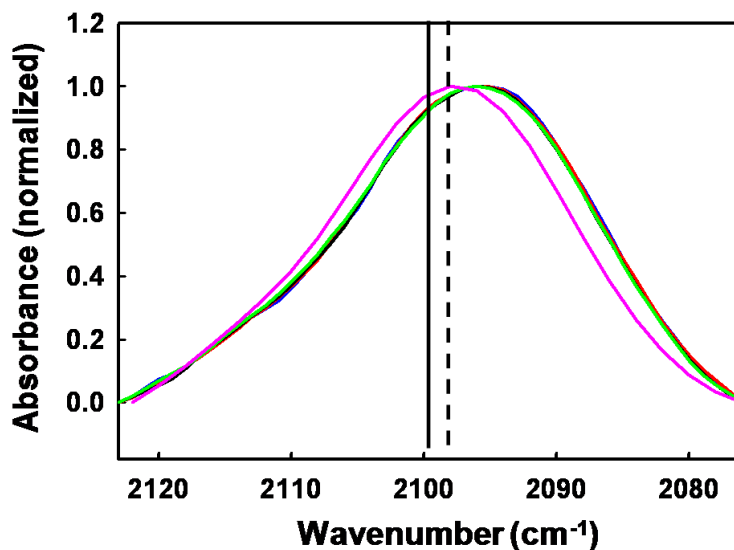
Fig. 3-6. Overlaid spectra of the symmetric CD_2 stretching band at particular time points after OA-d application (1.35mm away from the source center) compared to that of the OA-d droplet on the SC obtained within 5-10 min after application (pink). Time after application (in H): blue, 4.5; red, 12.5; black, 29.0; green, 50.5. The spectral region is baseline corrected at 2123-2076 cm^{-1} and normalized to highlight the frequency shift. The vertical solid line is the COM frequency for the droplet (2098.6 cm^{-1}); whereas the dashed line is the averaged COM frequency for the four different time points (2097.5 cm^{-1}).

The use of perdeuterated OA permits the detection of permeant-induced changes in endogenous SC lipid acyl chain conformation via frequency shifts in the methylene stretching bands. In a similar manner, frequency shifts in the CD_2 stretching bands can indicate interaction between the disordered OA-d chains and the highly ordered lipids of the SC. Overall, the lower the frequency, the greater the acyl chain conformational order. No sign of alteration to endogenous structure was detected in the OA-d treated SC samples; however, measurable

changes in the $\nu_{sym}CD_2$ suggest that at least a portion of the OA-d has penetrated into the SC. Since the transmission mode is utilized to acquire the IR images, the resultant spectra are a weighted average of OA-d residing on the surface and that which has penetrated into the SC. As shown by the overlaid spectra in Figure 3-6, the $\nu_{sym}CD_2$ for OA-d decreases by ~1.5 cm^{-1} comparing the frequencies immediately after a drop was placed on the SC surface and in octanol solutions (~2098.6 and 2099.0 cm^{-1}, respectively) with frequencies measured in glyph-poor regions of the SC at various time points after application (2097.4 and 2097.5 cm^{-1} after 4.5 and 29H, respectively). Similar changes are observed for the $\nu_{asym}CD_2$ (not shown). A 1.5 cm^{-1} shift covers approximately a quarter of the wavenumber range available for this vibrational mode and indicates that a moderate degree of acyl chain conformational ordering has taken place as the OA-d likely interacts with the more highly ordered SC lipids. In earlier reports from our laboratory, both the ν_{asym} and $\nu_{sym}CD_2$ have been used as indicators of acyl chain perdeuterated permeant penetration and interaction with SC lipids[26, 28].

3.3.2 DMSO-d diffusion experiments.

In contrast to the OA-d experiments discussed above, IR imaging experiments of DMSO-d lateral diffusion in the SC directly detected structural perturbation to endogenous SC protein. Figure 3-7 displays overlaid IR spectra from imaging experiments at various time points after the application of DMSO-d to SC. In addition to bands specific to DMSO-d (Figure 3-7A), i.e., CD$_3$ stretch (2050-2250 cm^{-1}) and S=O stretch (1000-1100 cm^{-1}), the presence of a shoulder

(~1626 cm^{-1}) on the low frequency side of the Amide I band was observed (Figure 3-7B), indicating a fair degree of DMSO-induced keratin denaturation. In the IR spectra of the SC, keratin is the major contributor to absorbance in the Amide I region with minor contributions arising from small amounts of various SC proteins and the ceramide Amide group. The overall symmetric shape of the Amide I band and frequency position (~1650 cm^{-1}) before DMSO-d application are indicative of keratin's helical structure. However, after DMSO-d is applied, the increase in intensity at ~1626 cm^{-1} denotes the formation of β-sheet structure. Similar DMSO-induced helix to sheet transitions have been previously observed by IR in human SC and isolated human corneocytes[29, 30] and the detection of keratin denaturation herein provides proof that DMSO has penetrated into the corneocytes within the SC. The apparent splitting at the Amide I peak maximum, evident in Figure 3-7B, is caused by saturation of the MCT IR detector due to the thickness of the SC (~15 μm).
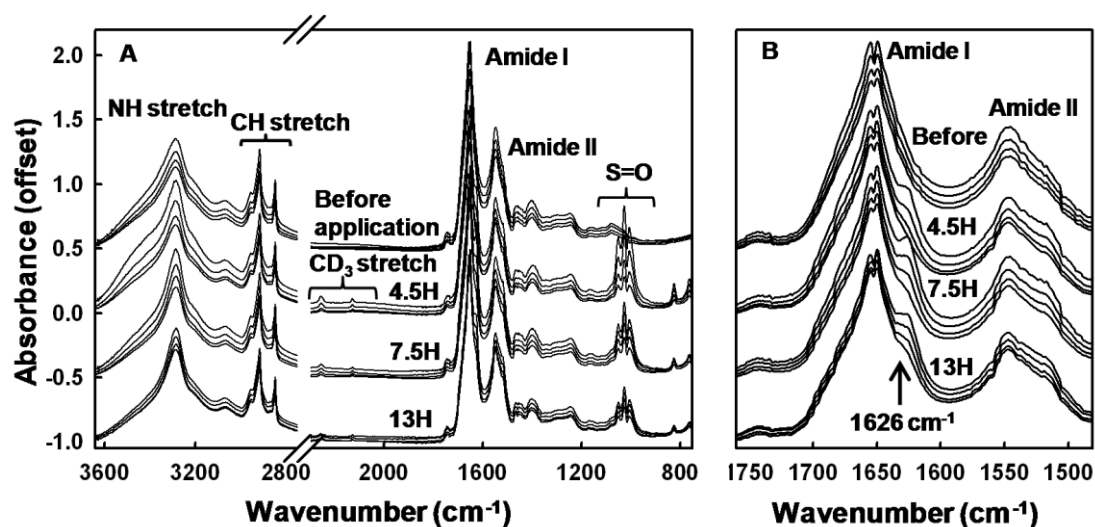
Fig. 3-7. IR spectra of DMSO-d at ~1.0 mm from the center of the source. 7A: Offset representative spectra at 0, 4.5, 7.5 and 13 H following DMSO-d application. Bands of interest are labeled. 7B: Enlarged Amide I/II region (baseline corrected at 1450-1750 cm^{-1}) highlighting the evolution of a shoulder at ~1626 cm^{-1} indicative of keratin denaturation (see text for details) after DMSO-d exposure.

IR images of the time evolution of DMSO-d lateral diffusion in a glyph-poor SC region (see visible image in Figure 3-8A) are displayed in Figure 3-8B where DMSO-d concentration is observed to go through a maximum 3.0-6.0 H after application. In addition, the source droplet of DMSO-d vanishes from the visible images within the first two hours after application. The circular region of high DMSO-d concentration (deep red) evident in the center of the lower half of the images taken at ≥7.5 H is suggested to arise from a hair follicle. Images depicting the relative amount of keratin denaturation are displayed in Figure 3-8C. A time delay between the maximum DMSO-d concentration in a particular spatial region and keratin denaturation is evident when the images are compared and is shown more clearly in Figure 3-9A. In this figure, the time evolution of DMSO concentration (C/C_o) is plotted along with the relative amount of β-sheet at a position 1.35mm away from the center of the source. Each data point shown is measured from the average of 14 spectra. A delay time of 3-4.5H is observed between increasing DMSO-d concentrations and observable β-sheet formation. Under the current experimental conditions, keratin denaturation does not appear to be reversible with time as DMSO-d concentration decreases. This observation will be explored in future experiments as keratin denaturation was shown to be largely reversible after corneocyte exposure to high relative humidity[30]. Thus, the observed structural perturbation to keratin in the SC is consistent with a transcellular penetration route for DMSO which includes a pathway through both the lipid matrix and corneocytes.
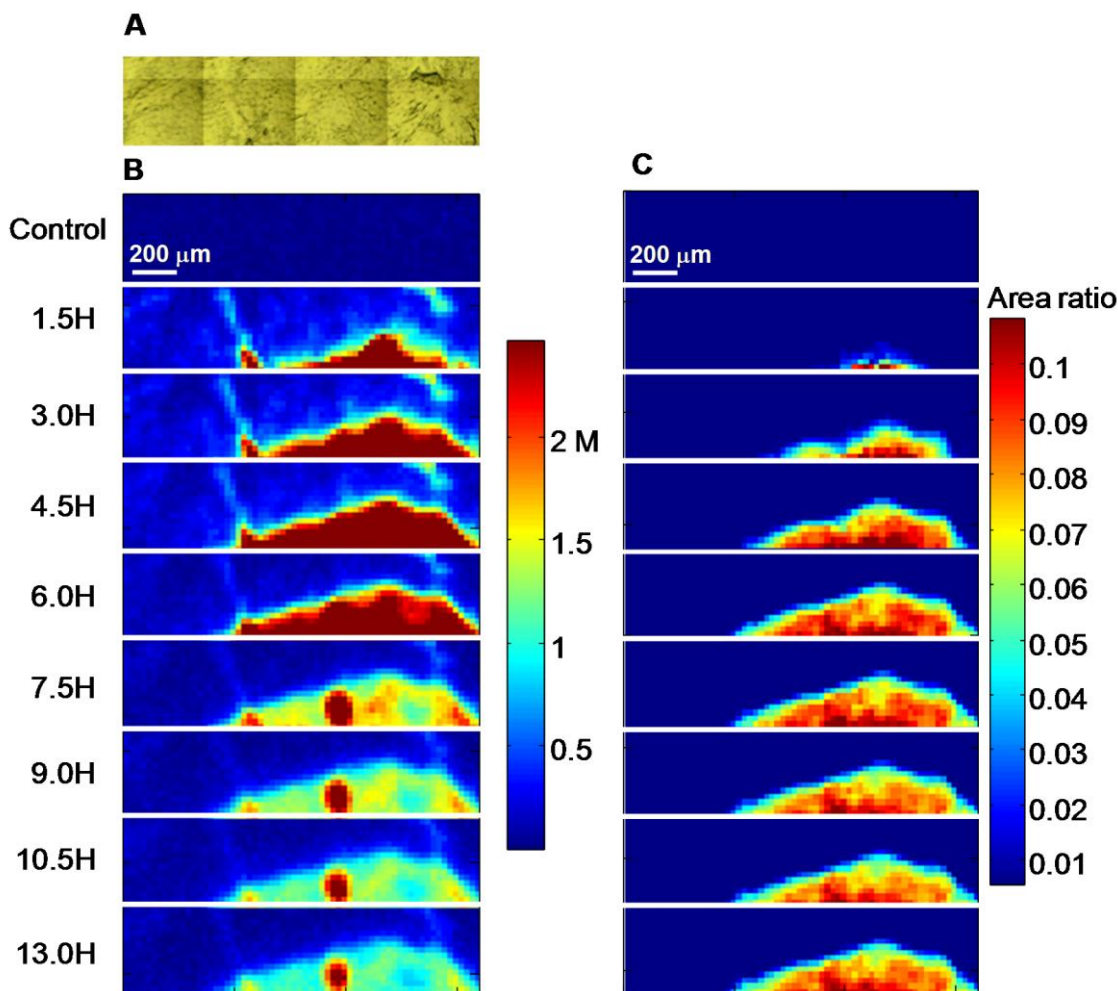
Fig. 3-8. IR images of DMSO-d diffusion in a relatively glyph-poor SC region as function of time. 8A: Visible image of the SC in the IR imaging area (1.60 X 0.40 mm^2). The source droplet was deposited at the lower right side and its edge impinged within the image area by ~50mm with an initial radius of 0.9mm. 8B: IR images of DMSO-d concentration before and after application as function of time. The concentration range of 0-2.47 M is shown for better viewing of DMSO-d diffusion. DMSO-d concentration is calculated based on the asymmetric CD$_3$ band area (baseline corrected over 2281-2232 cm^{-1}) according to Beer's Law. 8C: IR images of the relative amount of keratin denaturation measured by the integrated area ratio of the β-sheet shoulder (1644-1590 cm^{-1}) to the CH stretching region.

A comparison between experimental and calculated DMSO-d concentrations as a function of time at a position 1.35 mm away from the source is shown in Figure 3-9B along with comparable OA-d concentrations for the glyph-poor experiment. The calculated curves for a wide range of diffusion coefficients (5 x 10^{-10} to 2 x 10^{-7}) are shown. There is a marked difference

between the experimental results for the two permeants. Although the magnitudes of the calculated C/C_o values for the larger diffusion coefficients ($\geq$5 x 10^{-8}) at early times (<10H) are greater than that of the experimental values, the behavior of the calculated curves with a maximum C/C_o (peak flux) at relatively early times are similar to the DMSO-d experimental results.
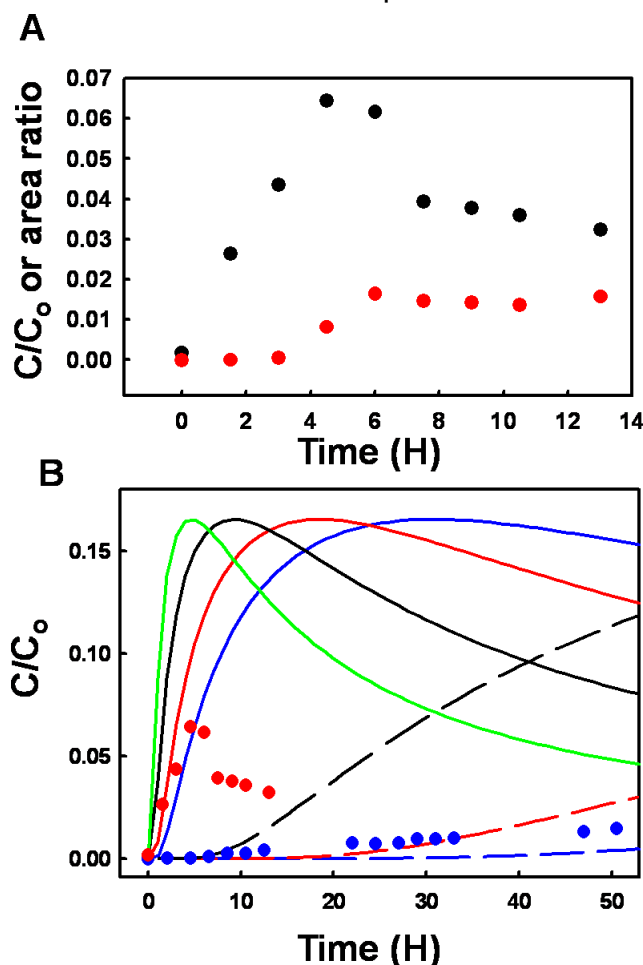
Fig. 3-9A. Overlay of DMSO-d concentration as C/C_o where C_o is the initial DMSO-d concentration and a relative measure of keratin denaturation (as described for Figure 3-8C) as a function of time at a position 1.35mm away from the source center highlighting the time-delay of protein denaturation. Each data point shown is the average of 14 spectra (black: DMSO-d C/C_o; red: keratin denaturation). 9B: Comparison between experimental (DMSO-d, red and OA-d, blue symbols; both relatively glyph-poor regions) and calculated concentrations (C/C_o) as a function of time at 1.35mm away from the source center. Calculated concentrations are obtained from Crank's equation (see text for details). Diffusion coefficients for the simulated plots are as follows: solid lines (source radii: 0.9mm): blue: 0.3e-7 cm^2/s; red: 0.5e-7; black: 1.0e-7; green: 2.0e-7; dashed lines (source radii: 1mm): blue: 0.5e-9 cm^2/s; red: 1.0e-9; Black: 3.0e-9.

3.4 Discussion:

Early studies of model lipid and human red blood cell membranes report that the rate of lateral diffusion is more rapid than transbilayer transport[31, 32]. In skin, relatively few studies have attempted to track both the penetration and lateral diffusion of drugs. Most of those studies employ tape stripping protocols that have the potential to provide information regarding both penetration and lateral diffusion of exogenous agents, albeit confined to the SC region of skin (see Introduction). One very recent in vitro study[2] included the tape stripped SC layers, deeper skin layers and lateral skin parts. In general, although the analytical techniques utilized in these studies provide precise quantitative measures of permeant concentrations, information regarding possible perturbation to endogenous SC structure is lacking. Endogenous molecular structure information is also lacking in fluorescence-based diffusion measurements.

The IR imaging method we demonstrate here for tracking lateral diffusion of exogenous materials in the SC offers some advantages. One major advantage of IR spectroscopy is that there is no need to attach a chromophore to the exogenous agent under study. Additionally, IR spectra provide molecular structure information from endogenous skin components and the exogenous material whose diffusion is being monitored. In the current study, we take advantage of deuterated analogues to isolate the C-D stretching modes of the molecule of interest. This also frees up the C-H stretching region of skin lipids yielding information regarding permeation mechanisms. Depending on the IR

spectrum of the exogenous agent, other spectral regions may also remain free from spectral overlap, as demonstrated herein by the DMSO-induced endogenous keratin denaturation detected in the Amide I region. Finally, when IR imaging is conducted in the transmission mode and the sample has a uniform thickness, Beer's Law provides quantitative concentration values for the exogenous agent.

The concentration profiles depicted in a glyph-rich region in Figure 3-3 clearly reveal that the predominant contribution to OA-d lateral spreading arises from these structures. The role of glyphs as pathways for lateral diffusion on the skin surface has been previously reported[15, 16], although we believe the IR images shown here (Figure 3-3) are the first to report the spatial distribution of the concentration of exogenously applied material. Lateral transport along the glyphs not only competes with penetration but also provides a reservoir of exogenous material in regions removed from the site of application. Thus as glyph density is known to be dependent on body site, skin exposure, and aging[15,17,18], the consequences of these observations should be of significant interest for those involved with transdermal and cutaneous drug delivery, toxicology, and personal care or cosmetic applications. The phenomenon of glyph storage may partially account for age-related chronic skin dryness as glyph structures becomes less dense with age, thereby reducing the reservoir in skin for topically applied hydration products.

Attempts were made to fit the glyph-rich OA-d experimental data with empirical engineering models for the kinetics of liquid spreading in V-shaped

grooves[33], however, these models are based on complete wetting which does not apply to the current OA-d experiment. In addition, we have observed that absorption into the SC occurs while the OA-d spreads along the glyphs, a complication not accounted for in the engineering models cited above. Based on these two differences between models and experiment, it seems reasonable that the models consistently predicted much larger radii of spreading compared to our experimental data (results not shown). OA-d penetration in glyph-rich regions can be monitored in a manner similar to the glyph-poor OA-d experiments discussed above (Figure 3-6). The frequencies of $\nu_{sym}CD_2$ suggest that a fair portion of the OA-d in the vicinity of the glyphs has penetrated into the SC.

Alterations to endogenous SC lipid chain conformational order determined from shifts in CH_2 stretching frequencies were not detected in the OA-d treated SC samples. This is consistent with a recent publication from our laboratories[34] where IR imaging was employed to monitor OA-d penetration. In that study which used microtomed sections, OA-d was shown to permeate to the dermal/epidermal junction with no significant differences observed in endogenous SC lipid ordering. Seemingly in contrast, endogenous chain disordering was detected in *in vivo* attenuated total reflectance (ATR) IR measurements of OA-d penetration in human skin [34,35]. However ATR-IR only probes the outer few microns of the SC and when this measurement was combined with tape stripping, the perturbation to endogenous lipid structure was indistinguishable from an untreated skin region after a few tape strips. In the current experiment, the absence of a frequency shift is likely due to the use of the

transmission mode for IR spectral acquisition which produces spectra that reflect the average of the endogenous acyl chain conformation over the entire SC thickness. We also cannot rule out that a portion of the OA-d may be penetrating through slightly less ordered endogenous SC lipid regions, i.e. the grain borders described by Forslind[36] or through an altogether different route, eg., aqueous pores, although it is likely that these pathways would not produce the observed CD_2 frequency shifts.

In glyph-poor regions of the SC where we assume the OA-d has mostly penetrated, its distribution is reasonably well approximated by Crank's solution[27] of Fick's Second Law. A range of diffusion coefficients (0.3-1 x 10^{-8} cm^2/s) bracket the experimental data. Although this range for D is quite similar to that previously reported for the lateral diffusion of a series of fluorescent probes in extracted SC lipids (0.3-2 x 10^{-8} cm^2/s^6) and for the average D of hydrophilic and amphiphilic fluorescent probes in human SC (0.3-0.8 x 10^{-8} cm^2/s^8), we may be underestimating the diffusion coefficient due to penetration or diffusion in the Z-dimension given that the isolated SC is ~15 microns thick. In addition, as noted above, the diffusion coefficient that best fits the experimental data (see Figure 3-5) appears to decrease with time. More rapid lateral diffusion at earlier time points may also be due to some initial wicking or spreading of OA-d across the SC surface prior to penetration into the SC. Other discrepancies may arise when utilizing Crank's model because the SC's native heterogeneity is not consistent with the model's assumption of isotropic media.

Estimation of lateral diffusion coefficients for DMSO-d in the SC via the current IR imaging experiment is hampered by the relatively quick diffusion of this well-known permeation enhancer compared to the timescale of our measurement. The data presented in Figure 9 appear to indicate that D values in the 10^{-7} cm^2/s range may be appropriate. The design of future imaging experiments is being modified to sample smaller areas of the SC on a faster timescale, along with the possible addition of confocal Raman microscopy measurements to probe "z" direction diffusion. The difference in the magnitude of calculated C/C_o (for D in the 10^{-7} cm^2/s range) compared to the experimental data is thought to be due to permeation of DMSO-d throughout the SC thickness as mentioned above.

One result of the DMSO-d experiments provides a clear demonstration of the major advantage of utilizing vibrational spectroscopic imaging for diffusion studies in skin. The ability to detect changes in the structure of endogenous SC components suggests the pathway/mechanism of the diffusing substance as is evident in Figure 3-7. Alterations to keratin's secondary structure in response to DMSO-d diffusion are strongly indicated by the low frequency shoulder that arises on the Amide I band (Figure 3-7B) revealing an intercellular diffusion pathway.

In summary, the inherent complexities of the SC constrain the ability to model the system accurately. However the approach demonstrated here offers the potential to identify permeant-induced perturbations to specific endogenous

SC species thereby providing useful and otherwise unavailable information for elucidating transport mechanisms.

3.5 Conclusions:

Utilizing IR imaging to track the spatial and temporal distribution of exogenous agents in isolated human stratum corneum provides insight into competitive lateral diffusion processes. Transport along networked furrows is shown to be the dominant mode of lateral diffusion for the lipophilic permeation enhancer oleic acid. As such, the glyphs provide a reservoir of exogenous material for penetration and further lateral diffusion. The acquisition of a complete IR spectrum at each sampling point provides unique molecular level information with respect to changes in the structure of endogenous SC constituents and exogenous agents as they interact with the SC. Thus, the observation of DMSO-induced keratin denaturation facilitates the elucidation of a transcellular pathway for this permeation enhancer. Finally, since the IR imaging experiments are conducted in the transmission mode, the application of Beer's law provides quantification of exogenous agent concentrations. This, in turn, facilitates the inherently difficult estimation of diffusion coefficients.

3.6 References:

1. Jepps, O. G.; Dancik, Y.; Anissimov, Y. G.; Roberts, M. S., Modeling the human skin barrier - Towards a better understanding of dermal absorption. *Adv. Drug Deliv. Rev.* **2013,** 65, 152-168.

2. Selzer, D.; Hahn, T.; Naegel, A.; Heisig, M.; Kostka, K. H.; Lehr, C. M.; Neumann, D.; Schaefer, U. F.; Wittum, G., Finite dose skin mass balance including the lateral part: Comparison between experiment, pharmacokinetic modeling and diffusion models. *J. Contr. Rel.* **2013,** 165, 119-128.

3. Potts, R. O.; Guy, R. H., Predicting skin permeability. *Pharm. Res.* **1992,** 9, 663-669.

4. Johnson, M. E.; Blankschtein, D.; Langer, R., Evaluation of solute permeation through the stratum corneum: Lateral bilayer diffusion as the primary transport mechanism. *J. Pharm. Sci.* **1997,** 86, 1162-1172.

5. Menon, G. K.; Elias, P. M., Morphologic basis for a pore-pathway in mammalian stratum corneum. *Skin Pharmacol.* **1997,** 10, 235-246.

6. Johnson, M. E.; Berk, D. A.; Blankschtein, D.; Golan, D. E.; Jain, R. K.; Langer, R. S., Lateral diffusion of small compounds in human stratum corneum and model lipid bilayer systems. *Biophys. J.* **1996,** 71, 2656-2668.

7. Anissimov, Y. G.; Zhao, X.; Roberts, M. S.; Zvyagin, A. V., Fluorescence recovery after photo-bleaching as a method to determine local diffusion coefficient in the stratum corneum. *Int. J. Pharm.* **2012,** 435, 93-97.

8. Brewer, J.; Bloksgaard, M.; Kubiak, J.; Sorensen, J. A.; Bagatolli, L. A., Spatially Resolved Two-Color Diffusion Measurements in Human Skin Applied to Transdermal Liposome Penetration. *J. Invest. Dermatol.* **2013,** 133, 1260-1268.

9. Ashworth, J.; Watson, W. S.; Finlay, A. Y., The alteral spread of clobetasol 17-propionate in the stratum corneum in vivo. *British Journal Derm.* **1988,** 119, 351-358.

10. Chambin-Remoussenard, O.; Treffel, P.; Bechtel, Y.; Agache, P., Surface recovery and stripping methods to quantify percutaneneous absorption of caffeine in humans. *J. Pharm. Sci.* **1993,** 82, 1099-1101.

11. Jacobi, U.; Weigmann, H.-J.; Baumann, M.; Reiche, A.-I.; Sterry, W., Lateral spreading of topically applied UV filter substances investigated by tape stripping. *Skin Pharmacol. Physiol.* **2004,** 17, 17-22.

12. Schicksnus, G.; Muller-Goymann, C. C., Lateral diffusion of ibuprofen in human skin during permeation studies. *Skin Pharmacol. Physiol.* **2004,** 17, 84-90.

13. Gee, C. M.; Nicolazzo, J. A.; Watkinson, A. C.; Finnin, B. C., Assessment of the lateral diffusion and penetration of topically applied drugs in humans using a novel concentric tape stripping design. *Pharm. Res.* **2012,** 10.1007/s11095-012-0731-7.

14. van der Molen, R. G.; Spies, F.; van 't Noordende, J. M.; Boelsma, E.; Mommaas, A. M.; Koerten, H. K., Tape stripping of human stratum

corneum yields cell layers that originate from various depths because of furrows in the skin. *Arch. Dermatol. Res.* **1997,** 289, 514-518.

15.   Jacobi, U.; Schanzer, S.; Weigmann, H.-J.; Patzelt, A.; Vergou, T.; Sterry, W.; Lademann, J., Pathways of lateral spreading. *Skin Pharmacol. Physiol.* **2011,** 24, 231-237.

16.   Dussaud, A. D.; Adler, P. M.; Lips, A., Liquid transport in the networked microchannels of the skin surface. *Langmuir* **2003,** 19, 7341-7345.

17.   Jacobi, U.; Chen, M.; Frankowski, G.; Sinkgraven, R.; Hund, M.; Rzany, B.; Sterry, W.; Lademann, J., *In vivo* determination of skin surface topography using an optical 3D device. *Skin Res. Tech.* **2004,** 10, 207-214.

18.   Lavker, R. M.; Kwong, F.; Kligman, A. M., Changes in skin surface patterns with age. *Journal of Gerentology* **1980,** 35, 348-354.

19.   Zhang, G.; Moore, D. J.; Sloan, K. B.; Flach, C. R.; Mendelsohn, R., Imaging the prodrug-to-drug transformation of a 5-Fluorouracil derivative in skin by confocal Raman microscopy. *J. Invest. Dermatol.* **2007,** 127, 1205-1209.

20.   Zhang, G.; Flach, C. R.; Mendelsohn, R., Tracking the dephosphorylation of resveratrol triphosphate in skin by confocal Raman microscopy. *J. Control. Release* **2007,** 123, 141-147.

21.   Mendelsohn, R.; Flach, C. R.; Moore, D. J., Determination of molecular conformation and permeation in skin via IR spectroscopy, microscopy, and imaging. *Biochim.Biophys.Acta* **2006,** 1758, 923-933.

22.   Forster, M.; Bolzinger, M.-A.; Ach, D.; Montagnac, G.; Briancon, S., Ingredients tracking of cosmetic formulations in the skin: A confocal Raman microscopy investigation. *Pharm. Res.* **2011,** 28, 858-872.

23.   Cotte, M.; Dumas, P.; Besnard, M.; Tchoreloff, P.; Walter, P., Synchrotron FT-IR microscopic study of chemical enhancers in transdermal drug delivery: example of fatty acids. *J. Contr. Rel.* **2004,** 97, 269-281.

24.   Tfayli, A.; Piot, O.; Pitre, F.; Manfait, M., Follow-up of drug permeation through excised human skin with confocal Raman microspectroscopy. In *Eur Biophys J*, **2007**, 36, 1049-1058.

25.   Gotter, B.; Faubel, W.; Neubert, R. H. H., FTIR microscopy and confocal Raman microscopy for studying lateral drug diffusion from a semisolid formulation. *Eur. J. Pharm. Biopharm.* **2010,** 74, 14-20.

26.   Mao, G.; Flach, C. R.; Mendelsohn, R.; Walters, R. M., Imaging the distribution of sodium dodecyl sulfate in skin by confocal Raman and infrared microspectroscopy. *Pharm. Res.* **2012,** 29, 2189-2201.

27.   Crank, J., *The Mathematics of Diffusion.* 2nd ed.; Oxford University Press: London, 1975.

28.   Saad, P.; Flach, C. R.; Walters, R. M.; Mendelsohn, R., Infrared spectroscopic studies of sodium dodecyl sulphate permeation and interaction with stratum corneum lipids in skin. *Int. J. Cosmet. Sci.* **2012,** 34, 36-43.

29. Oertel, R. P., Protein conformational changes induced in human stratum corneum by organic sulfoxides: An infrared spectroscopic investigation. *Biopolymers* **1977,** 16, 2329-2345.
30. Zhang, G.; Moore, D. J.; Mendelsohn, R.; Flach, C. R., Vibrational microspectroscopy and imaging of molecular composition and structure during human corneocyte maturation. *J. Invest. Dermatol.* **2006,** 126, 1088-1094.
31. Almeida, P. F. F.; Vaz, W. L. C.; Thompson, T. E., Lateral diffusion in the liquid-phases of dimyristoylphosphatidylcholine cholesterol lipid bilayers-a free-volume analysis. *Biochemistry* **1992,** 31, 6739-6747.
32. Lieb, W. R.; Stein, W. D., Non-stokesian nature of transverse diffusion within human red-cell membranes. *J. Membrane Biol.* **1986,** 92, 111-119.
33. Warren, P. B., Late stage kinetics for various wicking and spreading problems. *Cond-mat/0311216v1* **2003**.
34. Mack Correa, M. C.; Mao, G.; Saad, P.; Flach, C. R.; Mendelsohn, R.; Walters, R. M., Molecular interactions of plant oil components with stratum corneum lipids correlate with clinical measures of skin barrier function. *Experimental Dermatology* **2014,** 23, 39-44.
35. Naik, A.; Pechtold, L. A. R. M.; Potts, R. O.; Guy, R. H., Mechanism of oleic acid-induced penetration enhancement in vivo in humans. *J. Contr. Rel.* **1995,** 37, 299-306.
36. Forslind, B., A domain mosaic model of the skin barrier. *Acta Derm. Venerol.* **1994,** 74, 1-6.

Chapter 4: Ceramide Permeation into Human Stratum Corneum

4.1 Introduction:

Skin, the largest organ in the body, provides excellent barrier function by maintaining homoeostasis against harmful environmental insults, loss of water, and other essential components[1, 2]. The stratum corneum (SC), the major skin barrier, often depicted as "bricks and mortar" model, consists mainly of flattened dead cells, corneocytes, embedded in a continuous multilamellar lipid matrix. Figure 4-1 depicts lipid organization in human SC[3]. SC lipids are composed of ceramide (50%, w/v), cholesterol (25%, w/v) and free fatty acids (10%, w/v), as well as small amounts of cholesterol esters and cholesterol sulfate[4]. Ceramides (CERs) are the major lipid components of lamellar sheets present in the intercellular spaces of the SC.
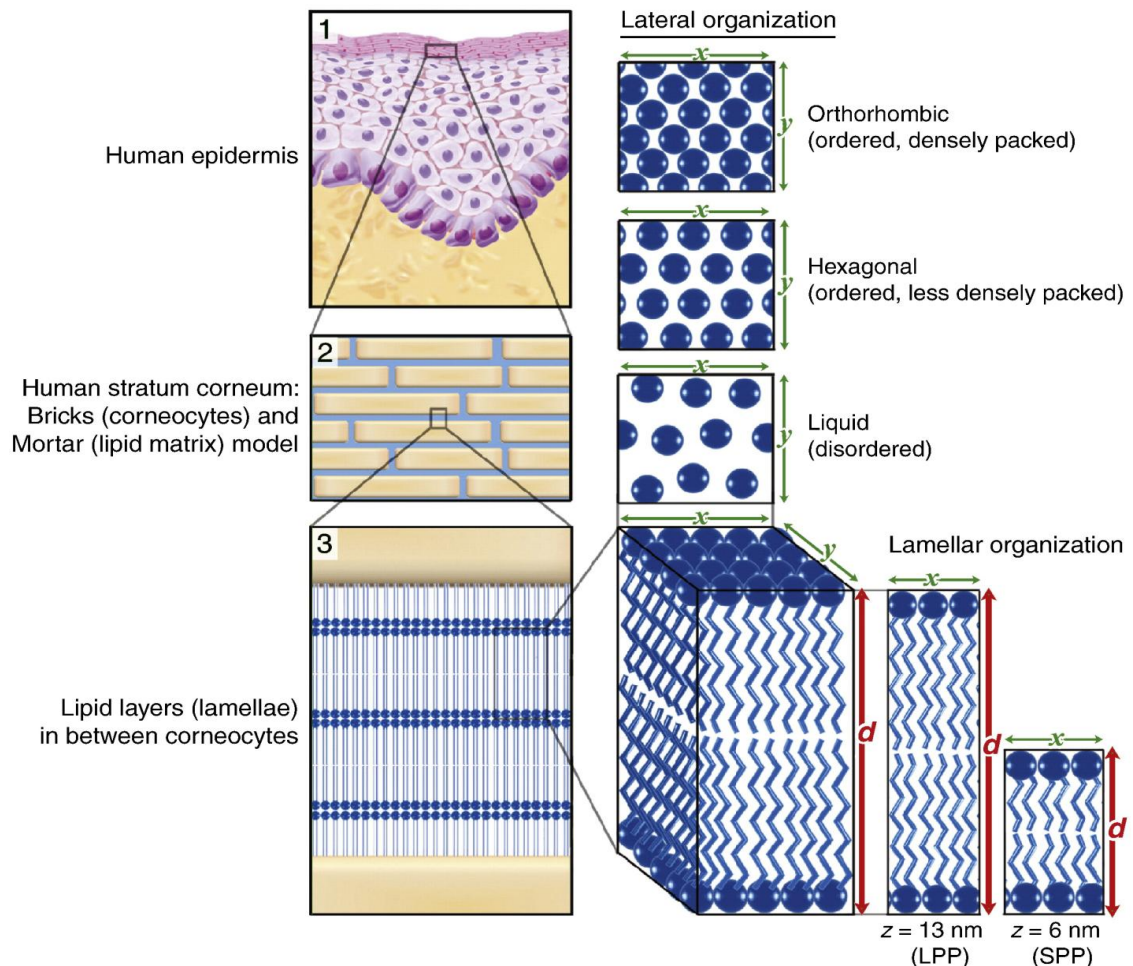
Fig. 4-1. Lipid packing in human SC. (1) the outermost layer of the epidermis, the SC. (2) The intercellular lipids are arranged in layers. (3) with either a long or short repeat distance (d), referred to as the long periodicity phase(LPP, ~ 13 nm) or short periodicity phase (SPP, ~ 6 nm), respectively. The lateral organization refers to the plane perpendicular to the direction of the lamellar organization. There are three possible packing motifs for the lipids; a very dense, ordered orthorhombic phase, a less dense, ordered hexagonal phase, and a disordered liquid phase. This image was originally published in the Journal of Lipid Research[5].

CERs are sphingolipids that contain a sphingoid moiety (which can be sphingosine (S), dihydrosphingosine (dS), phytosphingosine (P) or 6-hydroxy-sphingosine (H)), linked with a long chain free fatty acid moiety (which can be nonhydroxy (N), α-hydroxy (A) or ester-linked ω-hydroxy[6]) through an amide bond. To date, there have been 12 different classes of free CERs identified in human SC, which are named as "Ceramide XY" where "X" represents the type of

FFA moiety and Y represents the type of sphingoid base[7, 8]. Figure 4-2 illustrates the basic structure of CERs and CERs subclasses[3]. Table 4-1[3] also shows quantitative analysis of CERs in healthy human SC determined by thin layer chromatography (TLC) and liquid chromatography coupled to mass spectrometry (LC/MS). In general, CER [NP] is the most abundant subclass whereas the ultra-long acyl-CER subclasses ([EOdS], [EOS], [EOP], and [EOH]) contribute 8-13% of the CERs.

CER subclass	Analysis by TLC	Analysis by LC/MS	
	(n =2, Asian)	(n = 2, Asian)	(n = 15, Caucasian)
NdS*	10.4*	6.1	8.6
NS*		6.4	6.7
NP	25.4	22.1	25.8
NH	21	22.5	12.4
AS*	5.6*	3.4	3.8
AdS*		0.8	1.9
AP	14.7	15.7	13.4
AH	13.8	15.3	12.4
EOdS	ND	ND	1.3
EOS	4.3	4.3	5.4
EOP	1.3	0.9	2.7
EOH	3.5	2.6	5.4

*These subclasses are not separated on TLC and therefore share a common value. ND means not detected.

Table 4-1. CER composition in healthy SC determined by TLC and LC/MS. This table was originally published in Biochimica et Biophysica Acta[3].
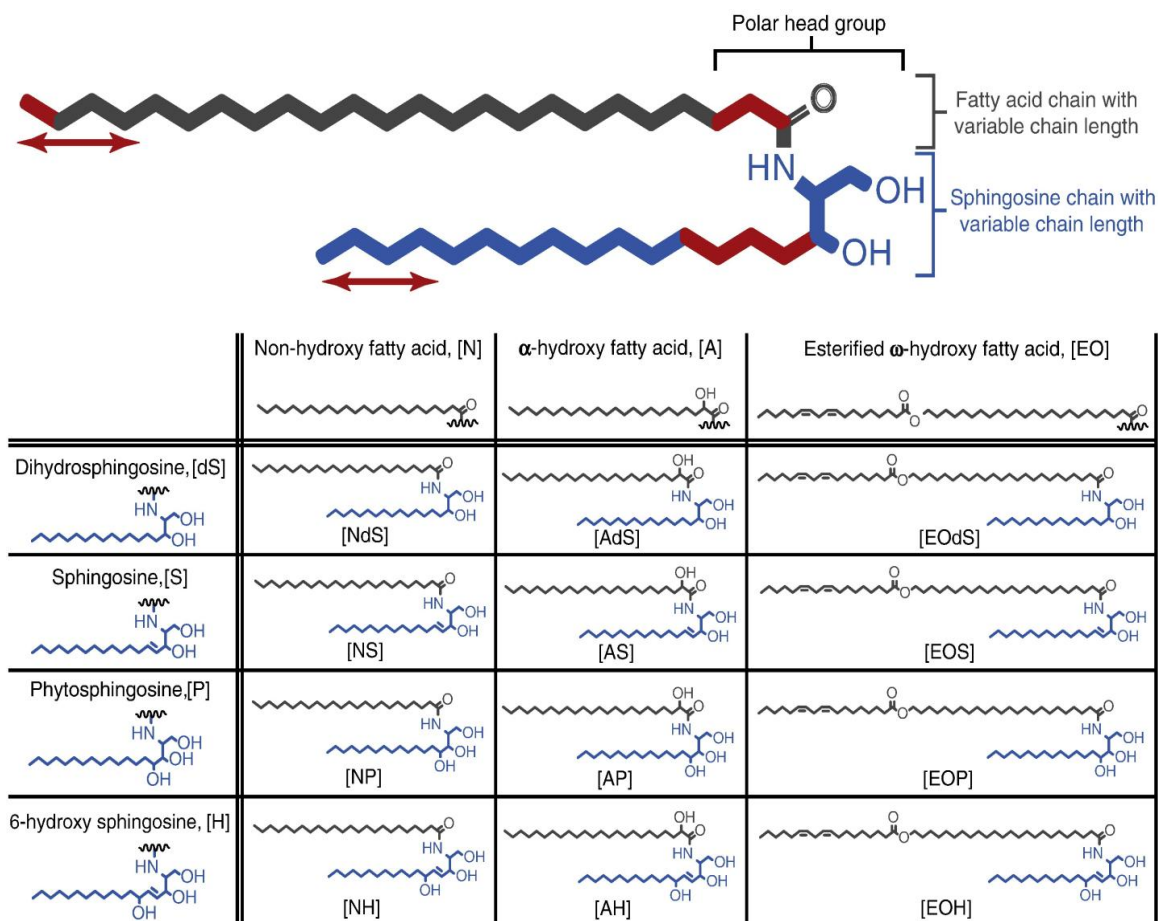
Fig. 4-2. Basic CER structure includes a sphingoid moiety and a long chain free fatty acid moiety.12 subclasses of CERs identified in Human SC and their corresponding structures are shown in the figure. This image was published in Biochimica et Biophysica Acta[3].

It is well known that CERs play an essential role in the water-retaining properties of the epidermis and are claimed to dramatically increase skin's hydration level, repair the cutaneous barrier, prevent moisture loss, and contribute to reducing dry flaky and aged skin[9]. Besides their structural role, CERs also serve as intracellular signaling molecules and regulate several biological processes, such as proliferation, differentiation, apoptosis, inflammation, and immune responses[10].

It is difficult to link skin disorders to changes in barrier lipid composition, especially in CERs, because of the many variables involved. However, most skin disorders, including atopic dermatitis[11] and psoriasis[12], often show an impaired barrier function and present a decrease in total CERs content with some differences in CER patterns. Table 4-2 summarizes current knowledge concerning lipid composition and organization in different skin disease states[3].

Disease	Lipid composition*	Lipid organization*
Lamellar ichthyosis	CER [NP] [EOS] ↓	Altered LPP, shorter lamellar periodicities, orthorhombicity ↓
Psoriasis	CER [EOP] [NP] [AP] ↓ CER [AS] and [NS] ↑	Altered LPP, shorter lamellar periodicities
Netherton	CER [EOS], [EOP], [EOH], [EOdS] [NP] ↓ short chain lipids ↑, unsaturated lipids ↑	Altered LPP, shorter lamellar periodicities, orthorhombicity ↓
Atopic dermatitis	CER [EOS], [EOP], [EOH], [EOdS] ↓ CER [AS], [AH], [AP], [AdS] ↑ short chain lipids ↑ unsaturated FFAs ↑	Altered LPP, shorter lamellar periodicities, orthorhombicity ↓
Chanarin -Dorfman	Acyl-CERs ↓ TAG ↑	Presence of non-lamellar lipid domains

* Among all the different studies, the general consensus is listed here.

Table 4-2. Overview of skin disease and alterations in lipid properties. This table was regenerated from Biochimica et Biophysica Acta[3].

Over the past decade, it has been suggested that formulations containing lipids identical to those in skin and, in particular, some CER supplementation, could improve pathological skin states. The utilization of physiological lipids has potential as new forms of topical therapy[13]. For progress in this research area to occur it is necessary to deliver the lipids into the SG-SC interface, because

organization of the SC lipids into bilayers takes place at this site[14-17]. However, it is usually difficult to administer the lipids deep into the interface using conventional formulations such as ointments and creams[18-20].

The penetration of deuterated CER [NP] as a model ceramide from various microemulsions (MEs) and a hydrophilic cream was investigated *ex vivo* using a Franz diffusion cell. The result of the study showed that CER [NP] could not permeate into deeper layers of the SC from a conventional hydrophilic cream, whereas permeability of CER [NP] into and across SC was significantly enhanced by MEs. In addition, the toxicity of the MEs was assessed. But in this study, the amount of CER [NP] permeated was quantified by HPLC coupled with MS. Not only is this detection method complicated, but also the skin sample preparation following permeability studies is tricky and time consuming, and includes tape stripping and lipid extraction[2].

Paepe's group reported a study incorporating CER 3B into common oil-in-water (o/w) emulsions and investigated the beneficial effect on barrier function by measuring the TEWL of SLS-induced scaly skin. They were able to develop suitable galenic ceramide-containing formulas, but unfortunately, their results showed no positive effect on TEWL values of SLS-damaged skin compared with that of proper controls[21]. This result was rationalized by others who suggested that single- or two-component lipid mixtures have no effect, and might even delay normal barrier recovery in disrupted skin[13, 21-23]. Paepe's group later compared the effect of two topically applied ceramide-containing emulsions with different lipid compositions on barrier repair of SLS and acetone-induced skin damage.

They showed that the emulsion with a complete mixture of skin lipids (emulsion 2) has significantly accelerated the barrier recovery better than a mixture of two types of CERs (emulsion 1) after SLS damage according to the TEWL values. After acetone damage, TEWL showed no effect with both emulsions, but emulsion 2 seemed to improve the skin hydration level compared to emulsion 1[23]. A natural lipid mixture, Y2, derived from animal porcine tissue proved to enhance barrier recovery in acetone-treated mouse skin, accelerate barrier recovery in acetone and tape-stripped human skin, increase SC hydration in both acutely disrupted and normal human skin, and accelerate permeability barrier recovery and enhance SC moisturization[23].

An *In vivo* test on the back of hairless mice following UVB irradiation was conducted to compare the recovery rate of the skin barrier after a mixture of natural lipids or liposomes with the same lipid composition was applied. The results showed that the liposomes had a higher turnover of the skin barrier compared with the mechanical mixture of lipids[24]. Parra's group also showed that internal wool lipids with stable liposome structure have the ability to accelerate the repair of water barrier functions more than the SC liposomes after SLS-chemical disruption and tape-stripped mechanical disruption[25], and can protect against detergent-induced dermatitis[26].

Measurements of TEWL and skin conductance were used to determine skin barrier function and hydration levels for most of the above studies. Both approaches are indirect techniques which provide no information concerning the

extent to which those skin lipids permeated into or across the SC, or into deeper skin layers.

Vávrová's group described the synthesis of fluorescent ceramide with different acyl chain lengths. The penetration of these NBD-labelled exogenous ceramide and pseudoCer 14S24 was visualized by fluorescence microscopy shown in figure 4-3[27].
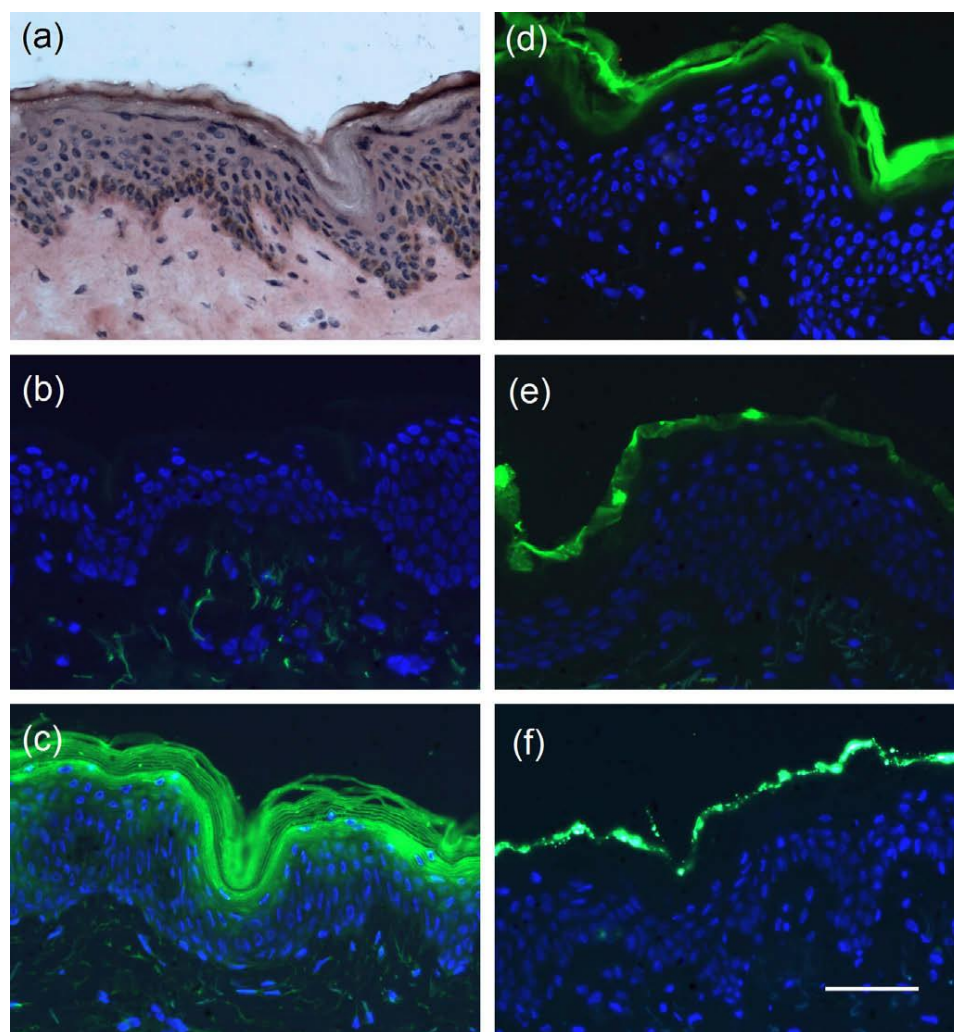
Fig. 4-3. Penetration of exogenous fluorescent CERs with different chain lengths and pseudoCer 14S24 into human skin. Histological sections are shown using brightfield microscopy with H&E staining (panel a), fluorescence microscopy with nuclei of cells (blue) stained with the Hoechst 33258 dye (b–f). (a) and (b) controls, (c) NBD-C_6-Cer, (d) NBD-C_{12}-Cer, (e) NBD-C_{24}-Cer, (f) NBD-14S24. Scale bar, 50 μm. This image was originally published in Bioorganic & Medicinal Chemistry Letters[27].

Their study showed that penetration of exogenous NBD-CERs across SC is highly dependent on chain length, which may be due to the difference in partitioning and mobility of the short- and long-chain CERs. Despite the substantial sensitivity of this technique, there are some limitations for their usefulness in understanding penetration mechanisms in skin. First, it is time-consuming, inefficient and expensive to synthesize NBD-labeled CERs, especially for the long-chain CERs. Second, the experiments evidently require the presence of a fluorescent moiety which could have significant effects on CERs penetration after adding a big conjugated group, and possibly changing the polarity of CERs.

Fourier transform infrared (FT-IR) spectroscopy is a vibrational spectroscopy-based method, which provides molecular structure information about endogenous skin components in addition to the exogenous agent whose penetration is being monitored. Over the past twenty years, the development of IR microspectroscopic imaging has proven the feasibility of acquiring spatially resolved spectra from microtomed skin sections and intact skin. Several studies from our lab and others[28-33] have demonstrated the utility of the approach. Penetration of exogenous agents is conveniently tracked from the spatial distribution of their vibrational band intensities. Although IR microscopic imaging has not been previously used to measure CERs penetration into skin, studies demonstrating the feasibility of the experiment have indeed appeared. Gotter et al.[34] investigated the heterogeneous lateral distribution of the anti-psoriasis drug dithranol in an artificial membrane. From our laboratories, Mao et al.[35] imaged

the distribution of deuterated sodium dodecyl sulphate (SDS-d) across different skin regions. A useful advantage of IR imaging was realized from the fact that Beer's Law is obeyed in the IR, thereby permitting (in the example cited above) determination of the SDS concentrations in the skin.

Based on the fact that there are hundreds of skincare products containing CER on the market claiming to dramatically increase the skin's hydration level, repair the cutaneous barrier, prevent moisture loss, and contribute to reducing dry and flaky skin, we are curious to know whether topically applied ceramide will penetrate skin and aid in this process. In the current study, we demonstrate the feasibility of mapping CER permeation in human skin with IR imaging. We imaged the penetration of deuterated CERs with a common permeation enhancer, oleic acid (OA). The use of half chain perdeuterated CER [NS]-d31 and CER [NP]-d31, shown in figure 4-4, permits us to spectroscopically distinguish the exogenous agents from the endogenous SC lipids without affecting penetration parameters. Images of CERs concentration are also generated after applying extinction coefficients determined from Beer's law. CER [NP]-d9 was also studied, but no CER could be detected due to reduced detection limits resulting from the presence of fewer deuterons (data not shown).
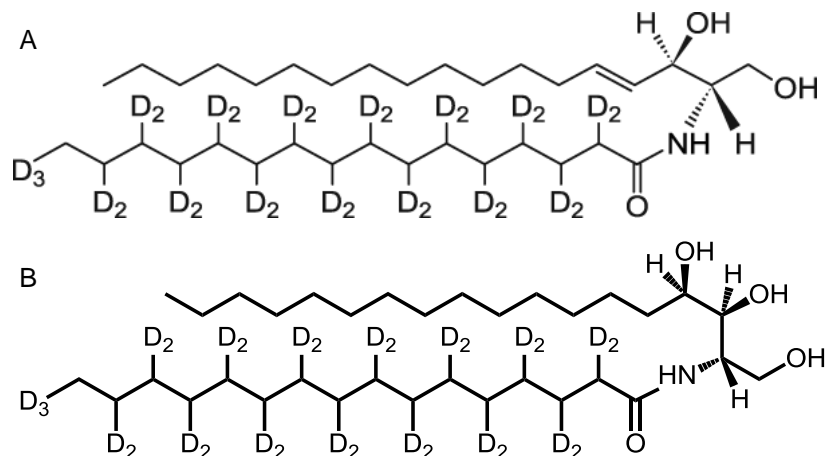
Fig. 4-4. The structures of the CERs studied. A. CER [NS]-d31 B. CER [NP]-d31

4.2 Materials and Methods:

4.2.1 Materials:

CER [NS]-d31, CER [NP]-d9, and CER [NP]-d31 were purchased from Avanti Polar Lipids (Alabaster, AL). OA was purchased from Sigma-Aldrich (St. Louis, MO). Human abdominal skin (otherwise to be discarded) from plastic surgery procedures, was obtained from dermatological offices following informed consent and approval of the institutional ethics committee. Samples were fast frozen with liquid nitrogen after removal of subcutaneous fat, cut into about 15 X 15 cm^2 pieces, and stored at -20°C for six months or less.

4.2.2 Methods:

Sample preparation

Ceramide was mixed with pure OA to make samples at ~10-12 mg/mL of ceramide. Skin samples of ~2 X 2 cm^2 surface area and ~2.5 mm thickness were

cut from a larger piece and defrosted on filter paper with the SC side up. The SC was cleaned with cotton swabs to remove surface fat and tape-stripped twice to remove most of the sebum from the surface. For the ceramide permeability study, skin samples were mounted and secured on a Franz diffusion cell (PermeGear, Inc., Hellertown, PA) with the SC facing the donor compartment. The acceptor compartment was filled with distilled water, and 50 μL of each suspension was applied on the skin surface (~0.64 cm^2). Samples, wrapped with parafilm to minimize water evaporation and to keep skin hydrated, were incubated at 34°C for 24 h or 48 h in separate experiments. Control experiments were conducted under the same conditions except using OA or OA-d alone. After incubation, excess suspension was removed with a cotton swab, the apparatus was disassembled, the skin surface was thoroughly wiped with Kimwipes and the center part of the skin samples was fast frozen with liquid N_2.

IR Microscopic Imaging

For IR imaging, samples prepared as described above were stabilized at -30°C within a Bright/Hacker 5030 Microtome (Bright Instrument Company, Huntington, UK/Hacker Instruments, Fairfield, NJ), and sections (~10 and 30 μm thick) were cut perpendicular to the SC. IR images of sections placed on CaF$_2$ IR windows were collected with a Perkin-Elmer Spotlight 300 system (PerkinElmer Life and Analytical Science, Inc., Waltham, MA) with an essentially linear array (16 X 1) of mercury-cadmium-telluride (MCT) detector elements. IR images were collected utilizing the transmission mode with a 6.25 X 6.25 μm^2 pixel size and 32 scans at a spectral resolution of 8 cm^{-1}. Image size was ~500 X 200 μm^2,

corresponding to 80 pixels in the x direction and 32 pixels in the y direction. Visible micrographs were obtained with the microscope integrated into the Spotlight 300 system. Two separate sets of skin specimens were prepared, imaged and analyzed. Typical data are presented here.

Determination of IR Extinction Coefficients of CER [NP]-d31

Chain perdeuteration of ceramide shifts the methylene stretching frequencies to a spectral region free from interference from endogenous skin vibrations. As IR spectra of skin sections were acquired in the transmission mode, Beer's law is applicable. To obtain extinction coefficients, CER [NP]-d31 was dissolved at known concentration in chloroform: methanol= 3:1 (v/v). Two fixed pathlength (16.4 μm and 200 μm) IR cells with CaF_2 windows were used to measure the absorbance of each standard solution. IR spectra were acquired with a Nicolet 6700 spectrometer (Thermo Electron Corporation, Madison, Wisconsin), 128 scans and using a spectral resolution of 2 cm^{-1}. A graph of the area of the asymmetric CD_2 stretching ($\nu_{asym}CD_2$) band (obtained using ISys 3.1 software, Malvern Instruments, UK) as a function of molar concentration is shown in Figure 4-5. Linear regression was used to find the best fit to the Beer's Law plots. The extinction coefficients (mol^{-1} dm^3 cm^{-1}) and correlation coefficient are as follows: 7467.7, 0.999. When calculating CER [NP]-d31 concentration, we assume that the thickness (pathlength) of skin section is 10 μm or 30 μm. The correlation coefficients demonstrate the high precision of using the asymmetric CD_2 stretching band areas for calculating CER [NP]-d31 concentrations in skin.
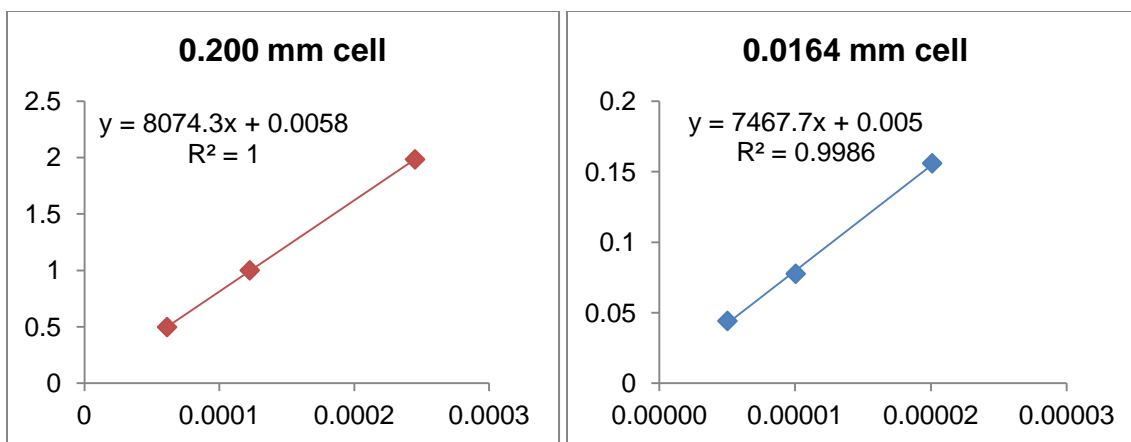
Fig. 4-5. The standard curves of CER [NP]-d31 in two-pathlength IR cells. The symbols represent experimental data, and the solid lines are linear regressions which best fit the data. The equations and R^2 values of the trendlines are also shown in the graphs.

IR Imaging Data Analysis

Vibrational microspectroscopic images were generated from IR spectral data using ISys 5.0 software (Malvern Instruments, UK). Image planes of spectral parameters (integrated peak areas, factor analysis) were produced after linear baselines were applied in spectral regions of interest. Image planes of ceramide concentrations were generated after using the extinction coefficient to estimate concentration. Figures were generated with SigmaPlot 2000 (SPSS Inc., Chicago, IL).

4.3 Results

4.3.1 Permeation of CER [NS]-d31

4.3.1.1 Ten micrometer-thick sections

A typical single-pixel IR spectrum of CER [NS]-d31 in skin is shown in Figure 4-6A with bands of interest marked. Figure 4-6B shows overlaid CD_2

stretching region (2234-2064 cm^{-1}) spectra in the area where the CER [NS]-d31

permeated. By integrating the area under the asymmetric CD_2 stretching band,

and converting to CER [NS]-d31 concentration according to Beer's law, we can
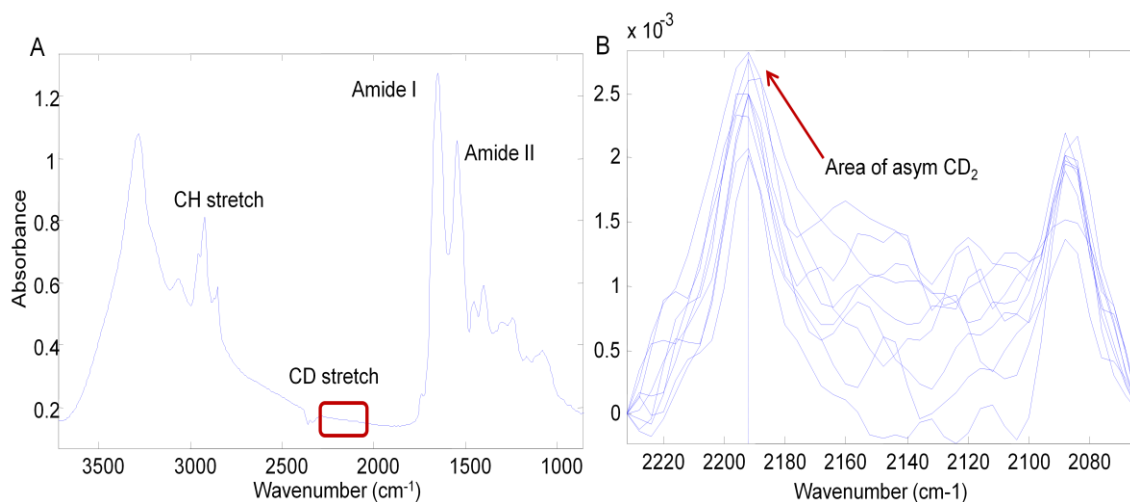
track the permeation of CER [NS]-d31 in skin.

Fig. 4-6A. A representative IR spectrum of CER [NS]-d31 in skin. The region marked with a square shows the CD_2 stretching bands free of interference from the endogenous skin bands. 6B. Overlaid IR spectra at CD_2 stretching region (2234-2064 cm^{-1}). Spectra were baseline corrected.

Visible micrographs of skin sections are shown in Figure 4-7A, with the SC

appearing on the left side of each skin section. The typical area over which IR

spectra are acquired is ~0.5 mm x 0.2 mm. IR images of the integrated

asymmetric CD_2 stretching band of CER [NS]-d31 are depicted in Figure 4-7B.

Figure 4-7C shows the interference from H_2O association band in the CD_2

stretching region; however, most of the H_2O association band is from the dermis.

To distinguish CD_2 stretching bands from the H_2O association band, factor

analysis of the CD_2 stretching region (2234-2064 cm^{-1}) was conducted after the

same spectral region was baseline corrected. Two factors obtained are shown in

Figure 4-7D. Factor score loading images for the H_2O association band and the

CD_2 stretching bands are shown in Figures 4-7E and F, respectively. High scores

in factor loading images of CD_2 stretching region in Figure 4-7F correlate well with the high score regions in the integrated area images in Figure 4-7B. The average concentration of ceramide (in CER-containing regions only) is ~6.3 mM, as calculated and explained in Figure 4-8. There are only 39 out of 30720 pixels averaged. The concentration was generated by converting integrated asymmetric CD_2 stretching band areas using the extinction coefficient of CER [NP]-d31 (due to the similarity of the structures) according to Beer's law.

Duplicate experiments were also conducted under the same conditions for 24 H to better understand the penetration properties of CER [NS]-d31. Factor analysis was also conducted for the CD_2 stretching region. Figure 4-9A-E show the visible images, IR images of CER [NS]-d31 concentration, two factor loadings, IR images of factor loadings of the H_2O association band, and IR images of factor loadings of CD_2 stretching bands, respectively. The average concentration is ~27.5 mM as calculated similarly as in Fig. 4-8.
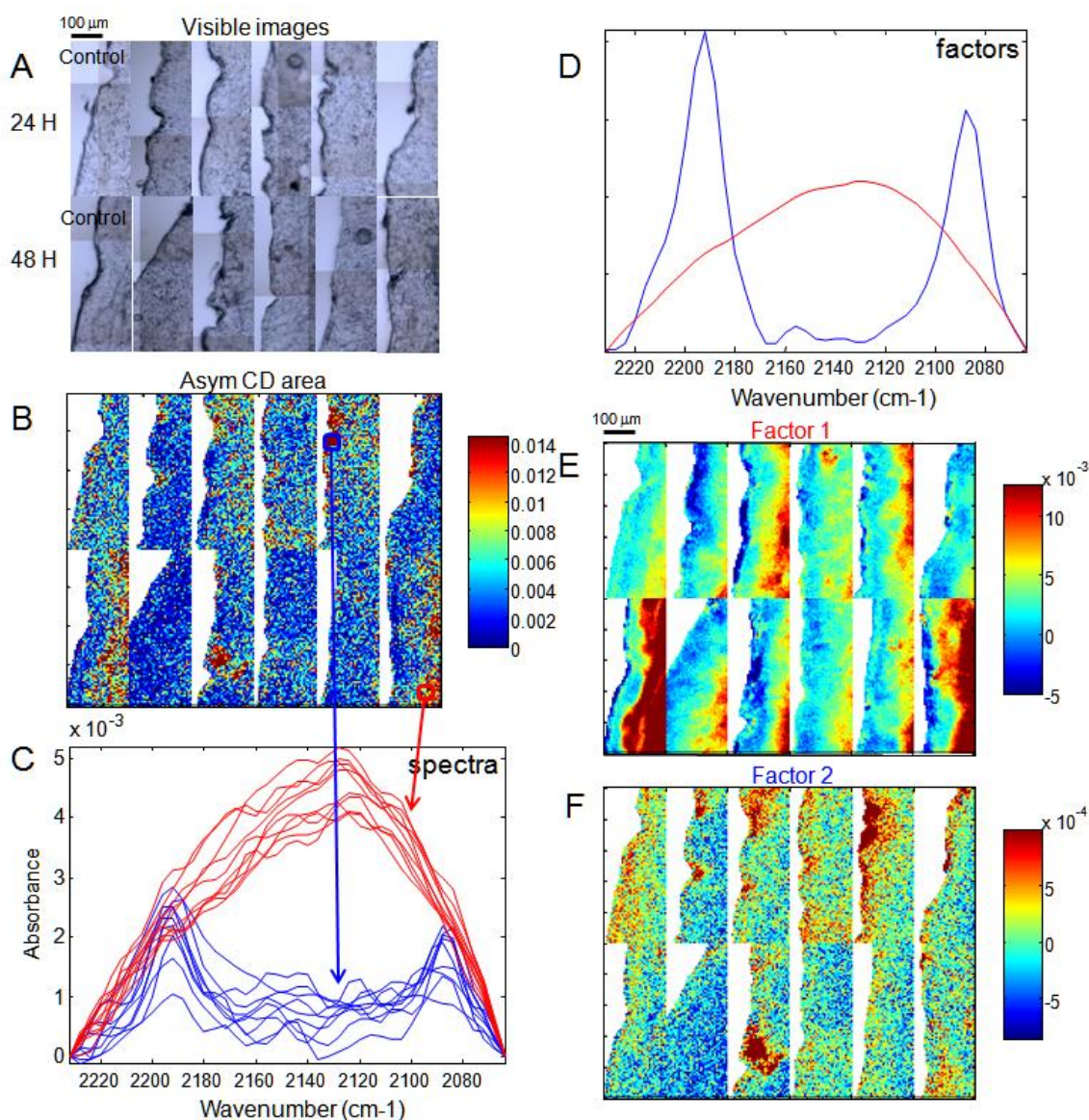
Fig. 4-7A. Visible images of skin sections on CaF$_2$ windows after different treatment conditions. 7B. IR images of integrated area of asymmetric CD$_2$ stretching band (± 2 STD). 7C. Spectra of the highlighted regions from the IR images of CER [NS]-d31 CD$_2$ stretching area. Blue: CD$_2$ stretching bands; red: H$_2$O association band. 7D. Factor loadings of the CD$_2$ stretching region. Blue: CD$_2$ stretching bands factor; red: H$_2$O association band factor. 7E. Factor loading score images from the H$_2$O association band (± 2 STD). 7F. Factor loading score images from the CD$_2$ stretching bands (± 2 STD). Scale bar is 100 μm.
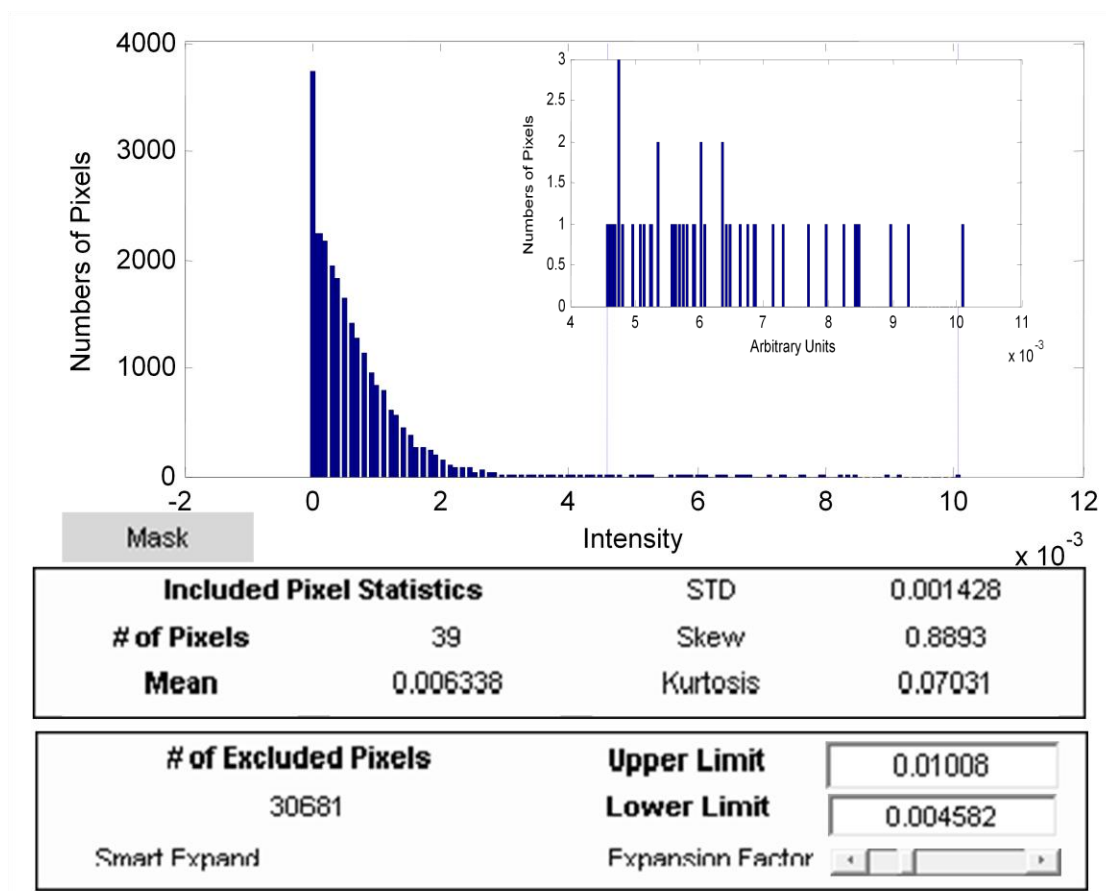
Fig. 4-8. Histogram of sample statistics from IR images of CER [NS]-d31 concentration in Fig. 4. The "Lower Limit" was set at 0.004582 because the IR detection limit is ~0.004-0.005 M, and the "Upper Limit" was set to the highest intensity in the histogram. In this case, the program averaged 39 "# of Pixels" in the chosen range, which gave the "Mean" of 0.006338. The inset shows the pixel distribution of the averaged region.

4.3.1.2 Thirty micrometer-thick sections

Due to the low detection limit of the CER [NS]-d31, thicker sections of skin were also imaged under the same sample preparation conditions. Since there is no difference between 24 or 48 H incubation time, the thicker sections were only incubated for 24 H. Figure 4-10A-B shows the visible micrographs, and IR images of CER [NS]-d31 concentration, respectively. The average concentration is ~11.9 mM as calculated similarly as in Fig. 4-8. Factor analysis was also

conducted for the CD_2 stretching region and the results are shown in Figure 4-10C-E.
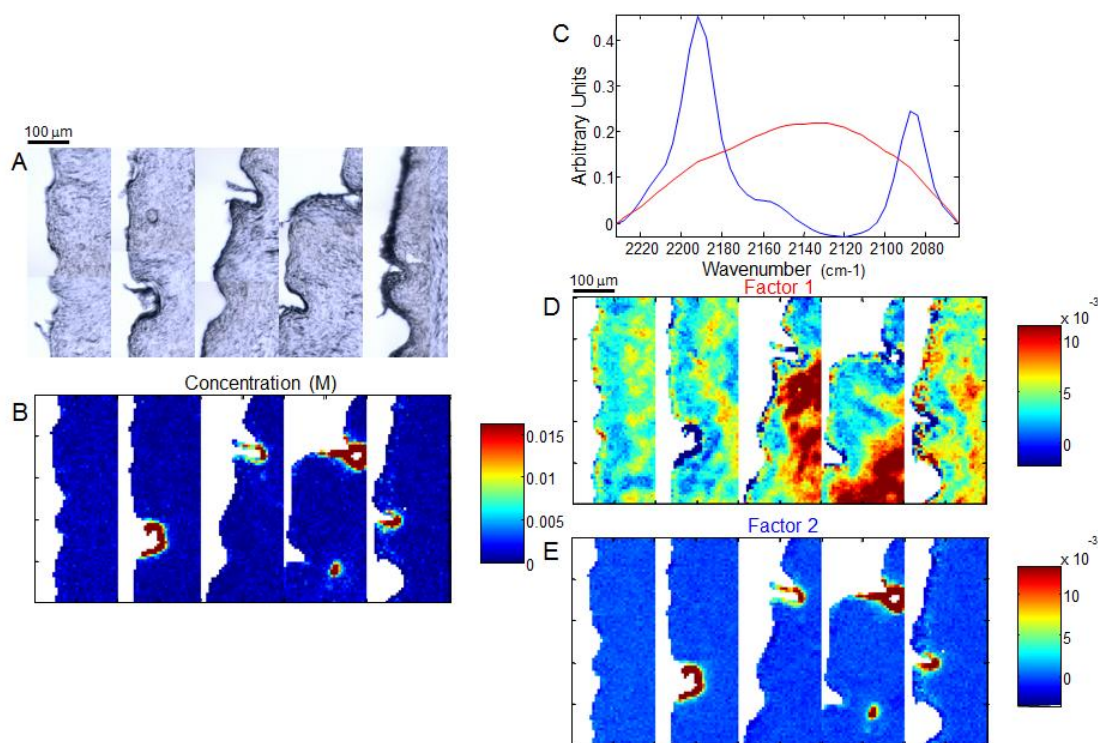

Fig. 4-9A. Visible images of skin sections on CaF_2 windows. 9B. IR images of CER [NS]-d31 concentration (± 2 STD). 9C. Factor loadings of CD_2 stretching region. Blue: CD_2 stretching bands; red: H_2O association band. 9D. Factor loading score images from the H_2O association band (± 2 STD). 9E. Factor loading score images from CD_2 stretching bands (± 2 STD). Scale bar is 100 μm.

4.3.2 Permeation of CER [NP]-d31

4.3.2.1 Ten micrometer-thick sections

Visible images of skin sections on CaF_2 IR windows at different incubation times are shown in Figure 4-11A. Figure 4-11B shows the IR images of the concentration of CER [NP]-d31 permeating into the skin. The average concentration is ~20.1 mM as calculated similarly as in Fig. 4-8. Factor analysis was also conducted over the CD_2 stretching region for CER [NP]-d31 to check if there is any interference from the H_2O association band. Figure 4-11C shows the

overlaid factor loadings of the CD_2 stretching region. The factor score loading images of H_2O association band and CD_2 stretching bands are shown in Figure 4-11D and 11E, respectively, which shows almost no interference from the H_2O association band. IR images of the concentration of CER [NP]-d31 in Figure 4-11B depicts exactly the same high score regions from factor 2 in Figure 4-11E. Duplicate experiments of penetration of CER [NP]-d31 were also conducted, which shows similar results as above. The average concentration is ~17.4 mM as calculated similarly as in Fig. 4-8.

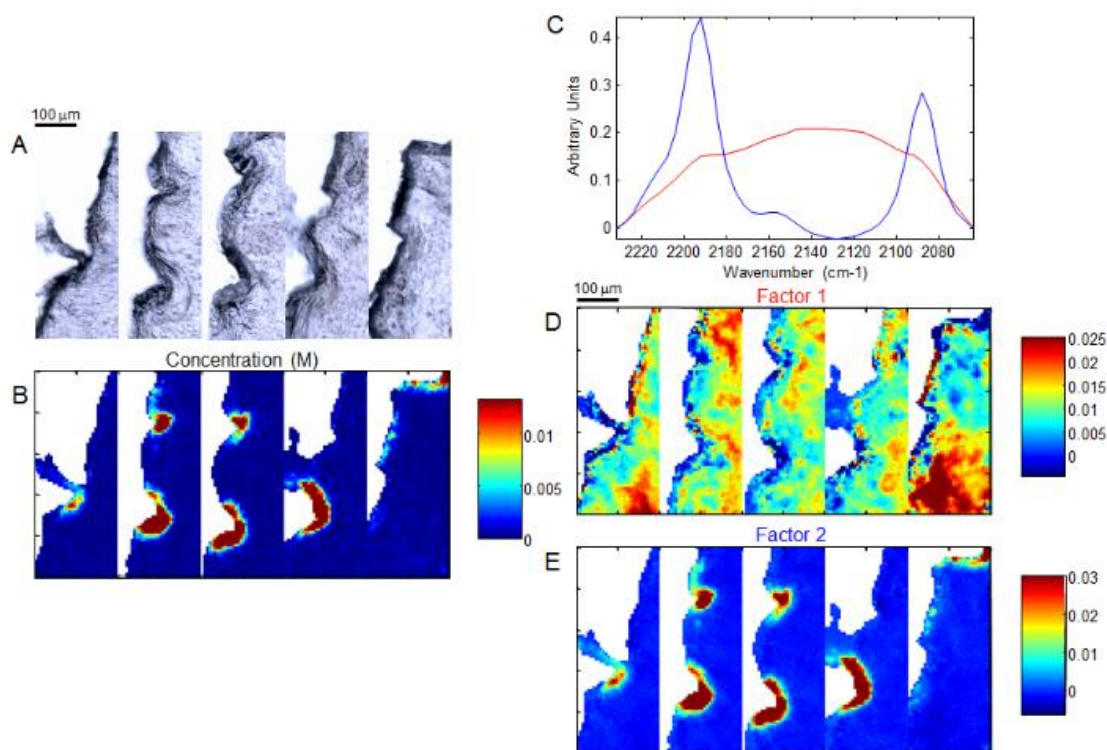Fig. 4-10A. Visible images of skin sections on CaF_2 windows. 10B. IR images of CER [NS]-d31 concentration (± 2 STD). 10C. Factor loadings for the CD_2 stretching region. Blue: CD_2 stretching band; red: H_2O association band. 10D. Factor loading score images from the H_2O association band (± 2 STD). 10E. Factor loading score images from CD_2 stretch bands (± 2 STD). Scale bar is 100 μm.

Fig. 4-11A. Visible images of skin sections on CaF$_2$ windows after different incubation time. 11B. IR images of CER [NP]-d31 concentration (± 2 STD). 11C. Factor loadings at CD$_2$ stretching region. Blue: CD$_2$ stretching band; red: H$_2$O association band. 11D. Factor loading score images from H$_2$O association band (± 2 STD). 11E. Factor loading score images from CD$_2$ stretching band (± 2 STD). Scale bar is 100 μm.
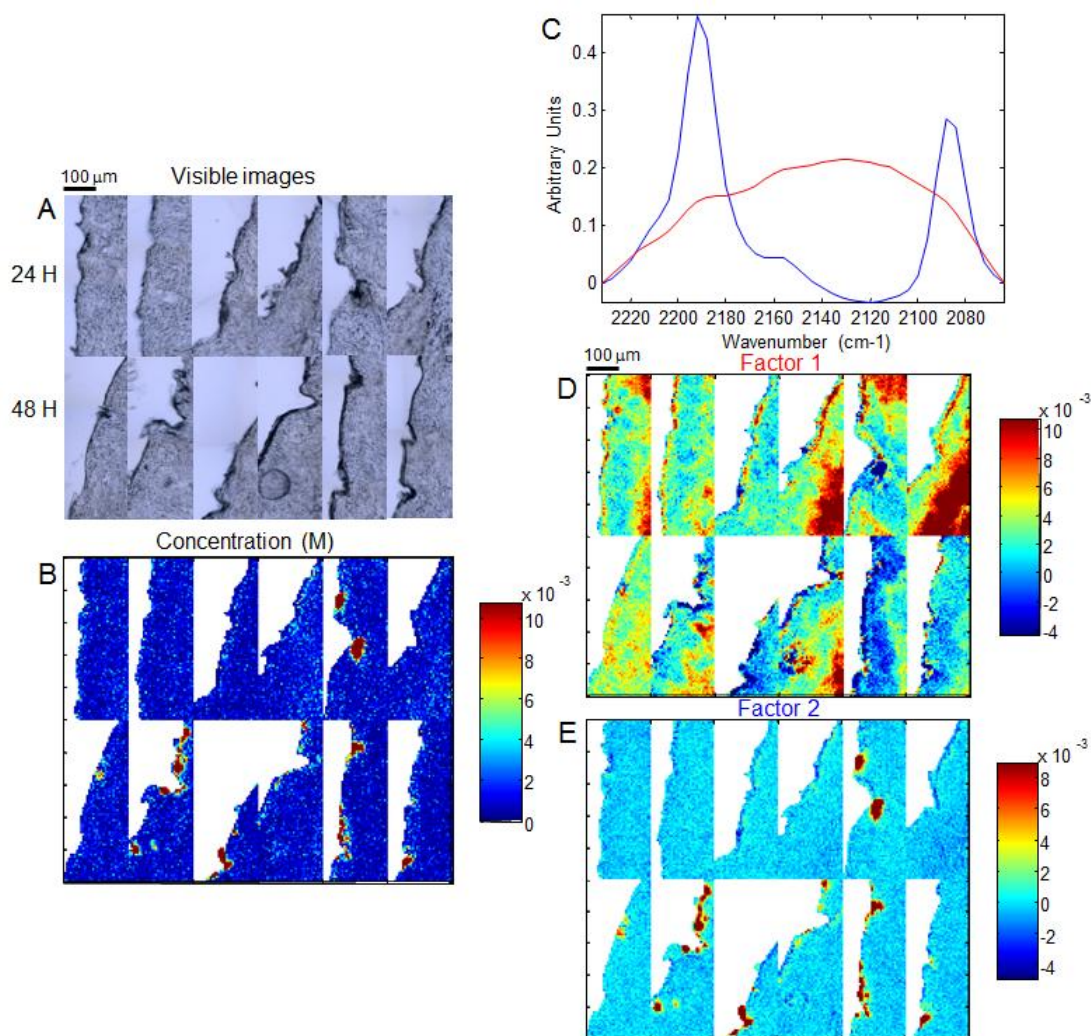
4.3.2.2 Thirty micrometer-thick sections

Similar to the CER [NS]-d31, thicker skin sections were imaged in order to increase detection sensitivity. The results are shown in Figure 4-12A-B. The average concentration is ~9.7 mM as calculated similarly as in Fig. 4-8.
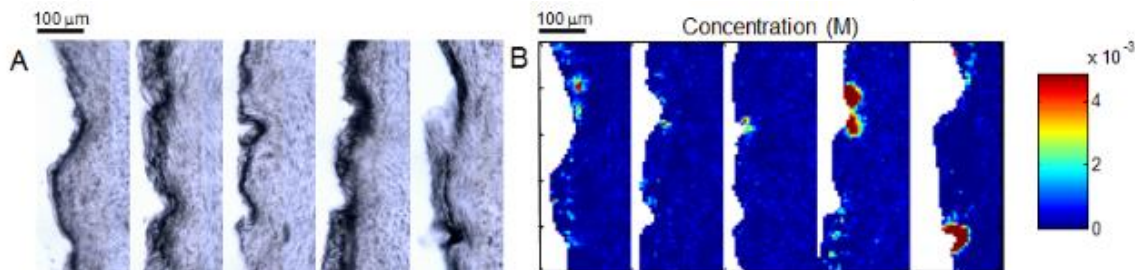

Fig. 4-12A. Visible images of thicker skin sections on IR windows. 12B. IR images of CER [NP]-d31 concentration (± 2 STD). Scale bar is 100 μm.

4.4 Discussion:

Early studies of topically applied CERs focused mainly on skin barrier function recovery determined by TEWL technique or skin conductance measurement[21, 23-26]; there was no information concerning the concentration of lipids penetrating into the skin to repair the barrier. Other groups investigated the penetration properties of CER [NP] with Franz diffusion cell methods together with LC/MS as analytical method, which is a sensitive tool, but with complicated procedures. In addition, no spatial distribution of the CERs can be visualized[2]. Other groups synthesized fluorescent CERs to track the penetration into skin. Despite the high sensitivity of the fluorescence microscopy, the presence of a fluorescent moiety could have significant effects on CER diffusion, especially in the heterogeneous environment of skin[27].

The IR imaging method we demonstrate here for tracking CERs penetration in human skin offers some advantages. One major advantage of IR spectroscopy

is that there is no need to synthetically attach the exogenous agent with a chromophore under investigation. Additionally, IR spectra provide molecular structure information from endogenous skin constituents and the exogenous material whose penetration is being tracked. In the current study, we take advantage of deuterated analogues to isolate the C-D stretching modes of the molecule of interest. Finally, when IR imaging is conducted in the transmission mode and the sample has a uniform thickness, Beer's Law provides quantitative concentration values for the exogenous agent.

All the IR images were masked based on the peak height of Amide II band after baseline correction in Amide I/II region in order to keep reasonable pixels only from skin. The integrated CD area profiles of CER [NS]-d31 depicted in Fig. 4-7B reveal that CERs are concentrated in pockets on the SC surface, especially in skin folds or glyphs compared to the visible images of the skin sections. The average concentration of CER [NS]-d31 is about 6.3 mM, close to the IR detection limit, which explains that the IR images of CER [NS]-d31 concentration exhibit a lot of noise, and even the H_2O association band that exists interferes in the CD_2 stretching region. Results of duplicate experiments shown in Fig. 4-9B indicate three times higher concentration. The only difference between these two separate experiments is that the skin sections imaged of the latter one have more deep glyphs or folds than the former one. Even at this high concentration, CER [NS]-d31 is still concentrated localized in pockets close to the SC surface.

In order to increase the detection sensivity to better understand the isolation of those well-identified pockets, thicker skin sections were also

investigated under the same condition. According to Beer's law, increasing the thickness of the skin sections will increase the pathlength in the IR beam pathway, which will enhance the CD stretch intensity. At the same time, it also brings other spectral regions, such as Amide I/II and CH stretch region off scale. There is indeed an increase of CD stretch intensity (spectrum not shown), which brings the detection limit from 4.5mM to 1.5mM. But as shown in Fig. 4-10B, onl0y pockets of high concentration of CER [NS]-d31 are shown. Some extent of distribution around those pockets are seen, probably due to the smear of the SC (the darker edges on the left side of each section is supposed to be SC) of the thicker sections on the IR window, which is evident from the visible images shown in Fig. 4-10A compared to the thinner sections shown in Fig. 4-9A. Attempts have made to image even thicker sections (data not shown), but it turned out that there was too much bulk water, which makes it hard for the sections to attach well on the IR windows, and compromises the spectral quality as well. In general, our results show that CERs do not substantially penetrate across SC or into the viable epidermis, which matches the fluorescent study suggesting that CERs only penetrate into SC, and that neither long nor short-chain NBD CERs can penetrate into nucleated epidermal layers[27].

Both ceramides seem to localize in pockets close to the skin surface. In order to investigate whether the ceramides remain on the skin surface or permeate into the SC, further analysis was conducted. Line plots of ceramide concentration and Amide II peak height were compared between glyph and non-glyph regions in Figure 4-13. The surface of the skin is defined at the half-

maximum Amide II peak height (~0.2 AU in the line plots). In the glyph set of plots, labeled 1 in Fig. 4-13, there is high CER concentration at ~0-10 μm from the image edge, in the region where the Amide II peak height is less than 0.2 suggesting that there is a significant amount of CER [NS]-d31 staying on the skin surface instead of inside the SC. There is some overlap, however, at ~25 μm from the image edge where the Amide II intensity indicates we are in the SC and where CER [NS]-d31 concentration is ~0.008-0.015M. A similar phenomenon was also observed in line plots 2 in Fig. 4-13 in a non-glyph region with a relatively lower concentration of ceramide. The line plots 3 were chosen at a place where no CER was observed in Fig. 4-13C, which serves as a baseline for analysis of line plots 1 and 2. In conclusion, CER [NS]-d31 is heterogeneously distributed on the skin surface with small pockets of low concentration penetrating ~10 microns into SC.
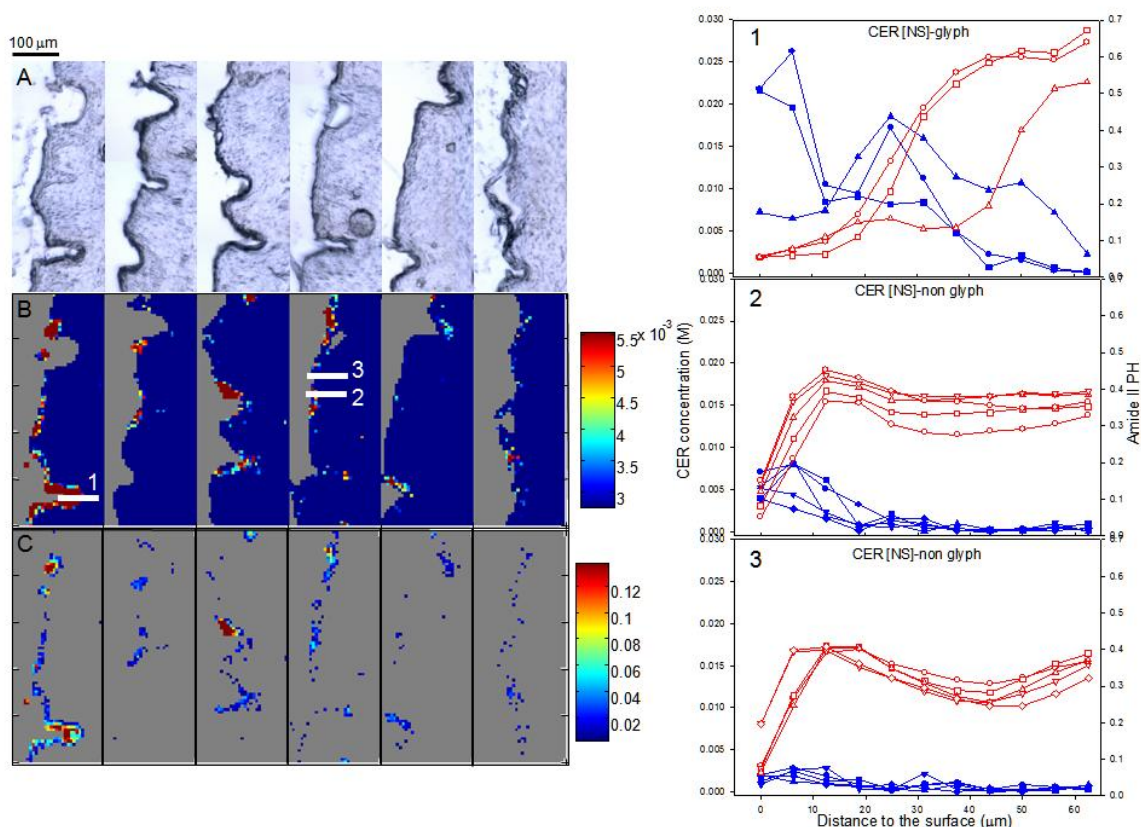
Fig. 4-13. Line plots at three different regions to compare the CER [NS]-d31 concentration and Amide II peak height. 13A. Visible images of skin sections. 13B. Concentration images of CER [NS]-d31 in M. The range is ~3-5.5e-3 M in order to highlight the pockets. White solid lines labelled with number 1-3 correlate with the line plots on the right, respectively. Each solid line covered 3-5 adjacent pixels. Closed symbols: CER concentration; Open symbols: Amide II peak height. 13C. Concentration images of CER [NS]-d31 masked below detection limit ~3e-3 M (± 1 STD). Scale bar is 100 μm.

Similar studies done with CER [NP]-d31 shows similar IR concentration profiles in Fig. 4-11B and 4-12B, but CER [NP]-d31 has a higher concentration range on average and it is still concentrated localized in pockets on the SC surface, in deep glyph areas or hair follicles. The line plots shown in Figure 4-14 suggest that CER [NP]-d31 is heterogeneously distributed on the skin surface with small pockets of low concentration penetrating ~10 microns into SC.
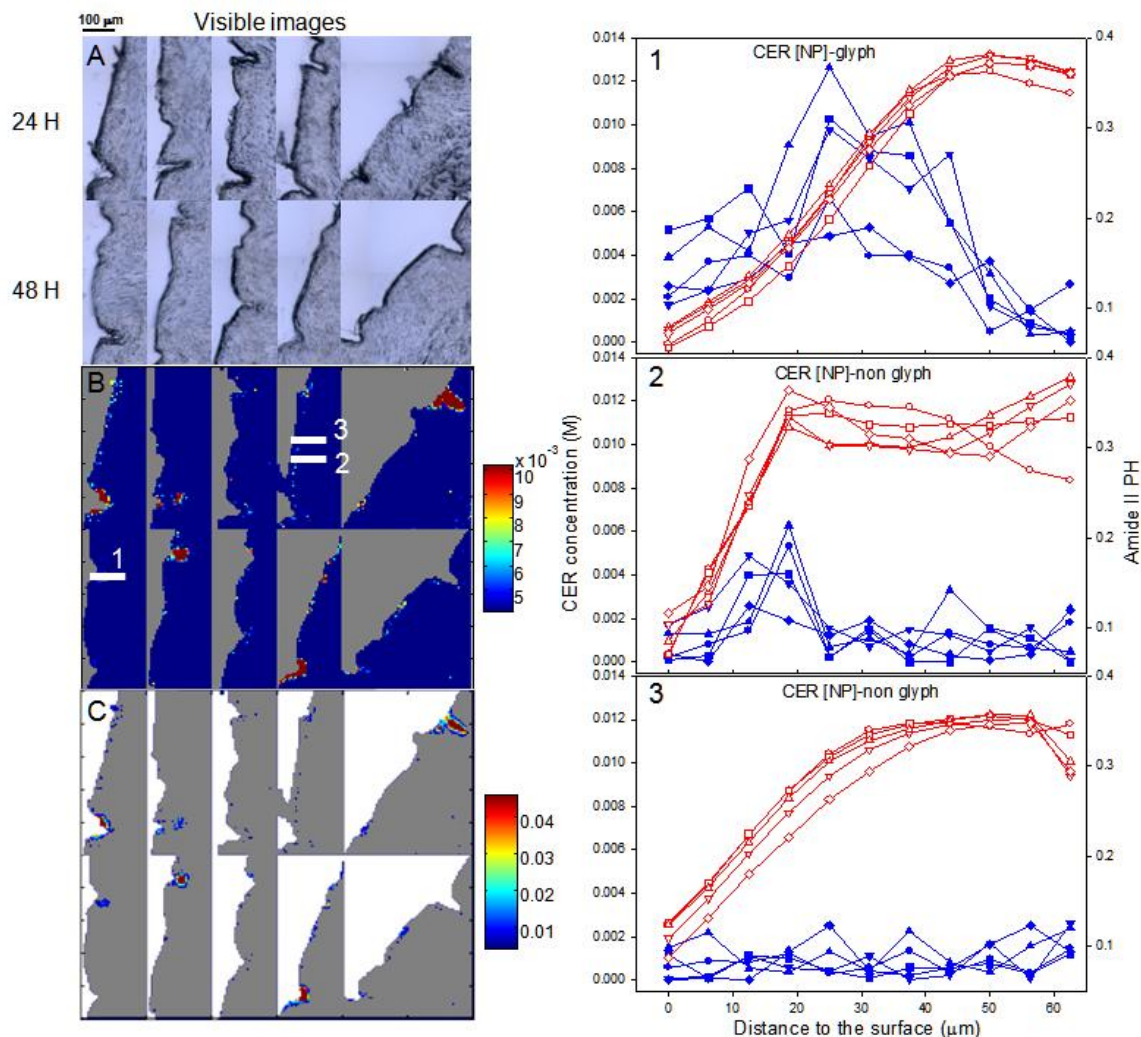
Fig. 4-14. Line plots at three different regions to compare the CER [NP]-d31 concentration and Amide II peak height. 14A. Visible images of skin sections. 14B. Concentration images of CER [NP]-d31 in M. The range is ~3.5-10e-3 M in order to highlight the pockets. White solid lines labelled with number 1-3 correlate with the line plots on the right, respectively. Each solid line covered 5 adjacent pixels. Closed symbols: CER concentration; Open symbols: Amide II peak height. 14C. Concentration images of CER [NP]-d31 masked below detection limit ~3.5e-3 M (± 1 STD). Scale bar is 100 μm.

The use of OA as penetration enhancer is supposed to improve the penetration of CERs. Since we observed limited CERs penetrating into the SC, it is of interest to examine OA penetration. One control experiment was conducted with protonated CER [NS] in deuterated OA-d_{34}. Other control samples were treated only with OA-d_{34}. Figure 4-15A shows the visible images of control skin sections. Figure 4-15B depicts the IR images of OA concentration and

distribution by integrating the asymmetric CD_2 stretch band. A more homogenous distribution of OA-d is observed penetrating into the SC and VE, mainly concentrating in the SC (± 1 STD is used to highlight the distribution of OA). The full concentration range is shown in Figure 4-15C. The results are in good agreement with the similar study conducted by a former group member[36]. In conclusion, OA, as a penetration enhancer, penetrates into the SC and VE with a fairly homogenous distribution, whereas, it did not significantly enhance the penetration of CERs into the skin.
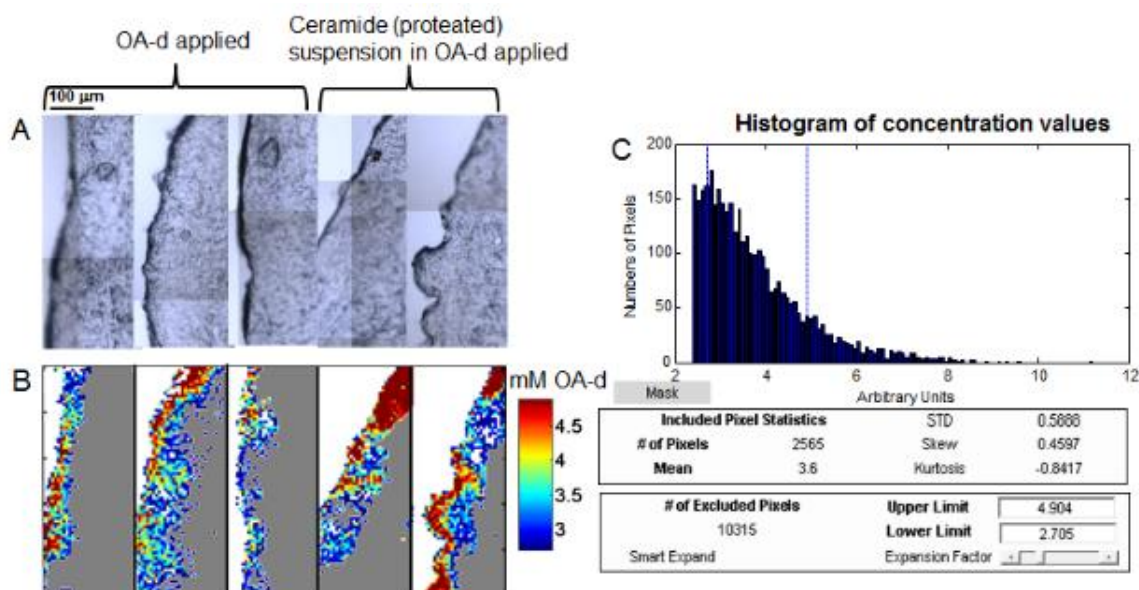

Fig. 4-15A. Visible images of skin sections on IR windows. 15B. IR images of OA concentration. (± 1 STD). 15C. Sample statistics of OA concentration in 15B showing the concentration distribution. Scale bar is 100 μm.

4.5 Conclusions:

The current application represents the first use of IR imaging technique to quantitatively investigate the penetration of CER [NS]-d31 and CER [NP]-d31 into human skin. With the help of OA as penetration enhancer, we are able to detect the average concentration of CER [NS]-d31 and CER [NP]-d31 as ~16.9 mM and ~18.8 mM respectively. Both ceramides are highly concentrated in pockets on the SC surface or top layers for both the thin and thick skin sections studied. Since those early studies of topically applied CERs were conducted on skins with compromised barrier functions such as acetone-treated or tape stripped, future studies can be done on a human skin equivalent, which has demonstrated different barrier function compared to normal human skin[37].

4.6 Reference:

1. Sahle, F. F.; Metz, H.; Wohlrab, J.; Neubert, R. H. H., Polyglycerol fatty acid ester surfactant-based microemulsions for targeted delivery of ceramide AP into the stratum corneum: Formulation, characterisation, in vitro release and penetration investigation. *European Journal of Pharmaceutics and Biopharmaceutics* **2012,** 82, 139-150.
2. Sahle, F. F.; Wohlrab, J.; Neubert, R. H., Controlled penetration of ceramides into and across the stratum corneum using various types of microemulsions and formulation associated toxicity studies. *Eur J Pharm Biopharm* **2013,** 86, 244-250.
3. Van Smeden, J.; Janssens, M.; Gooris, G. S.; Bouwstra, J. A., The important role of stratum corneum lipids for the cutaneous barrier function. *Biochim Biophys Acta* **2013,** 1841, 295-313.
4. Vavrova, K.; Zbytovska, J.; Palat, K.; Holas, T.; Klimentova, J.; Hrabalek, A.; Dolezal, P., Ceramide analogue 14S24 ((S)-2-tetracosanoylamino-3-hydroxypropionic acid tetradecyl ester) is effective in skin barrier repair in vitro. *Eur J Pharm Sci* **2004,** 21, 581-587.
5. Janssens, M.; van Smeden, J.; Gooris, G. S.; Bras, W.; Portale, G.; Caspers, P. J.; Vreeken, R. J.; Hankemeier, T.; Kezic, S.; Wolterbeek, R.; Lavrijsen, A. P.; Bouwstra, J. A., Increase in short-chain ceramides correlates with an altered lipid organization and decreased barrier function in atopic eczema patients. *Journal of Lipid Research* **2012,** 53, 2755-2766.
6. Park, K. Y.; Kim, D. H.; Jeong, M. S.; Li, K.; Seo, S. J., Changes of antimicrobial peptides and transepidermal water loss after topical application of tacrolimus and ceramide-dominant emollient in patients with atopic dermatitis. *Journal of Korean Medical Science* **2010,** 25, 766-771.
7. Mizutani, Y.; Mitsutake, S.; Tsuji, K.; Kihara, A.; Igarashi, Y., Ceramide biosynthesis in keratinocyte and its role in skin function. *Biochimie* **2009,** 91, 784-790.
8. Van Smeden, J.; Hoppel, L.; van der Heijden, R.; Hankemeier, T.; Vreeken, R. J.; Bouwstra, J. A., LC/MS analysis of stratum corneum lipids: ceramide profiling and discovery. *J Lipid Res* **2011,** 52, 1211-1221.
9. Zhang, L.; Hellgren, L. I.; Xu, X. B., Enzymatic production of ceramide from sphingomyelin. *Journal of Biotechnology* **2006,** 123, 93-105.
10. Kang, J. S.; Yoon, W. K.; Youm, J. K.; Jeong, S. K.; Park, B. D.; Han, M. H.; Lee, H.; Moon, E. Y.; Han, S. B.; Lee, C. W.; Lee, K.; Park, S. K.; Yang, K. H.; Kim, H. M., Inhibition of atopic dermatitis-like skin lesions by topical application of a novel ceramide derivative, K6PC-9p, in NC/Nga mice. *Experimental Dermatology* **2008,** 17, 958-964.
11. Imokawa, G.; Abe, A.; Jin, K.; Higaki, Y.; Kawashima, M.; Hidano, A., Decreased level of ceramides in stratum-corneum of atopic-dermatitis - an etiologic factor in atopic dry skin. *Journal of Investigative Dermatology* **1991,** 96, 523-526.

12. Motta, S.; Monti, M.; Sesana, S.; Mellesi, L.; Ghidoni, R.; Caputo, R., Abnormality of water barrier function in psoriasis - role of ceramide fractions. *Archives of Dermatology* **1994,** 130, 452-456.

13. Coderch, L.; Lopez, O.; de la Maza, A.; Parra, J. L., Ceramides and skin function. *Am J Clin Dermatol* **2003,** 4, 107-129.

14. Bouwstra, J. A.; Ponec, M., The skin barrier in healthy and diseased state. *Biochimica Et Biophysica Acta-Biomembranes* **2006,** 1758, 2080-2095.

15. Loden, M., The skin barrier and use of moisturizers in atopic dermatitis. *Clinics in Dermatology* **2003,** 21, 145-157.

16. Weerheim, A.; Ponec, M., Determination of stratum corneum lipid profile by tape stripping in combination with high-performance thin-layer chromatography. *Archives of Dermatological Research* **2001,** 293, 191-199.

17. Bonte, F.; Pinguet, P.; Saunois, A.; Meybeck, A.; Beugin, S.; Ollivon, M.; Lesieur, S., Thermotropic phase behavior of in vivo extracted human stratum corneum lipids. *Lipids* **1997,** 32, 653-660.

18. Liu, C. H.; Chang, F. Y.; Hung, D. K., Terpene microemulsions for transdermal curcumin delivery: effects of terpenes and cosurfactants. *Colloids Surf B Biointerfaces* **2011,** 82, 63-70.

19. Yuan, J. S.; Yip, A.; Nguyen, N.; Chu, J.; Wen, X. Y.; Acosta, E. J., Effect of surfactant concentration on transdermal lidocaine delivery with linker microemulsions. *Int J Pharm* **2010,** 392, 274-284.

20. Araujo, L. M.; Thomazine, J. A.; Lopez, R. F., Development of microemulsions to topically deliver 5-aminolevulinic acid in photodynamic therapy. *Eur J Pharm Biopharm* **2010,** 75, 48-55.

21. De Paepe, K.; Derde, M. P.; Roseeuw, D.; Rogiers, V., Incorporation of ceramide 3B in dermatocosmetic emulsions: effect on the transepidermal water loss of sodium lauryl sulphate-damaged skin. *Journal of the European Academy of Dermatology and Venereology* **2000,** 14, 272-279.

22. MaoQiang, M.; Feingold, K. R.; Wang, F. S.; Thornfeldt, C. R.; Elias, P. M., A natural lipid mixture improves barrier function and hydration in human and murine skin. *Journal of the Society of Cosmetic Chemists* **1996,** 47, 157-166.

23. De Paepe, K.; Roseeuw, D.; Rogiers, V., Repair of acetone- and sodium lauryl sulphate-damaged human skin barrier function using topically applied emulsions containing barrier lipids. *J Eur Acad Dermatol Venereol* **2002,** 16, 587-594.

24. Hatziantoniou, S.; Rallis, M.; Demetzos, C.; Papaioannou, G. T., Pharmacological activity of natural lipids on a skin barrier disruption model. *Pharmacological Research* **2000,** 42, 55-59.

25. De Pera, M.; Coderch, L.; Fonollosa, J.; de la Maza, A.; Parra, J. L., Effect of internal wool lipid liposomes on skin repair. *Skin Pharmacology and Applied Skin Physiology* **2000,** 13, 188-195.

26. Coderch, L.; De Pera, M.; Fonollosa, J.; De la Maza, A.; Parra, J., Efficacy of stratum corneum lipid supplementation on human skin. *Contact Dermatitis* **2002,** 47, 139-146.

27. Novotny, J.; Pospechova, K.; Hrabalek, A.; Cap, R.; Vavrova, K., Synthesis of fluorescent C-24-ceramide: Evidence for acyl chain length dependent differences in penetration of exogenous NBD-ceramides into human skin. *Bioorganic & Medicinal Chemistry Letters* **2009,** 19, 6975-6977.

28. Zhang, G. J.; Moore, D. J.; Sloan, K. B.; Flach, C. R.; Mendelsohn, R., Imaging the prodrug-to-drug transformation of a 5-fluorouracil derivative in skin by confocal Raman microscopy. *Journal of Investigative Dermatology* **2007,** 127, 1205-1209.

29. Zhang, G.; Flach, C. R.; Mendelsohn, R., Tracking the dephosphorylation of resveratrol triphosphate in skin by confocal Raman microscopy. *J. Control. Release* **2007,** 123, 141-147.

30. Mendelsohn, R.; Flach, C. R.; Moore, D. J., Determination of molecular conformation and permeation in skin via IR spectroscopy, microscopy, and imaging. *Biochim.Biophys.Acta* **2006,** 1758, 923-933.

31. Forster, M.; Bolzinger, M. A.; Ach, D.; Montagnac, G.; Briancon, S., Ingredients tracking of cosmetic formulations in the skin: a confocal Raman microscopy investigation. *Pharmaceutical Research* **2011,** 28, 858-872.

32. Cotte, M.; Dumas, P.; Besnard, M.; Tchoreloff, P.; Walter, P., Synchrotron FT-IR microscopic study of chemical enhancers in transdermal drug delivery: example of fatty acids. *Journal of Controlled Release* **2004,** 97, 269-281.

33. Tfayli, A.; Piot, O.; Pitre, F.; Manfait, M., Follow-up of drug permeation through excised human skin with confocal Raman microspectroscopy. *European Biophysics Journal with Biophysics Letters* **2007,** 36, 1049-1058.

34. Gotter, B.; Faubel, W.; Neubert, R. H. H., FTIR microscopy and confocal Raman microscopy for studying lateral drug diffusion from a semisolid formulation. *Eur. J. Pharm. Biopharm.* **2010,** 74, 14-20.

35. Mao, G.; Flach, C. R.; Mendelsohn, R.; Walters, R. M., Imaging the distribution of sodium dodecyl sulfate in skin by confocal Raman and infrared microspectroscopy. *Pharm. Res.* **2012,** 29, 2189-2201.

36. Correa, M. C. M.; Mao, G. R.; Saad, P.; Flach, C. R.; Mendelsohn, R.; Walters, R. M., Molecular interactions of plant oil components with stratum corneum lipids correlate with clinical measures of skin barrier function. *Experimental Dermatology* **2014,** 23, 39-44.

37. Yu, G.; Zhang, G. J.; Flach, C. R.; Mendelsohn, R., Vibrational spectroscopy and microscopic imaging: novel approaches for comparing barrier physical properties in native and human skin equivalents. *Journal of Biomedical Optics* **2013,** 18.

List of Publications

1. "*Raman Microspectroscopic and Dynamic Vapor Sorption Characterization of Hydration in Collagen and Dermal Tissue*"
Q. Zhang, K. L. A. Chan, G. Zhang, T. Gillece, L. Senak, D. J. Moore, R. Mendelsohn, C. R. Flach, *Biopolymers,* **2011**, 95, 607-615.
2. "*Infrared Spectroscopic Imaging Tracks Lateral Distribution in Human Stratum Corneum*"
Q. Zhang, P. Saad, G. Mao, R. M. Walters, M. C. Mack Correa, R. Mendelsohn, C. R. Flach, *Pharm. Res.* **2014**, DOI 10.1007/s11095-014-1373-8.

Curriculum Vitae

Birth: Feb. 03, 1986, in Pengzhou, Sichuan, China

Education:

01/2009-06/2014   Ph.D., Chemistry, Rutgers University-Newark, U. S.
                 Advisor: Dr. Richard Mendelsohn

09/2004-06/2008   B. Sc., Basic Pharmacy, China Pharmaceutical
                 University, China
                 Advisor: Dr. Qizheng Yao

Honors and Awards:

2004-2007: Scholarship of China Pharmaceutical University